# AERODYNAMICS OF HIGH PERFORMANCE BICYCLE WHEELS

---

A thesis submitted in partial fulfilment of the requirements for the

Degree of Master of Engineering

in Mechanical Engineering

in the University of Canterbury

by J. K. Moore

University of Canterbury

2008

---

# Table of Contents

# Acknowledgements

As my time as a Master's student draws to a close, there are a number of people who have assisted me with my research to which I am indebted. I must first acknowledge my supervisor, Dr Mark Jermy. I am grateful for his unwavering enthusiasm for this project and timely words of encouragement and I look forward to hearing about the research he undertakes in this field in the future.

Thank you to the project sponsor, Dynamic Composites, and their Technical Director, Milton Bloomfield for wishing to collaborate with the University on this project. I can't wait to see the improved wheels in action!

Several COP students from France have assisted me on this project and all made a valuable contribution. Thanks to Dante Paulo de Bittencourt for his early work on the finite element model of the disk wheel and Samuel Dupont for his assistance with designing the side force calibration device. Elise Mangeolle and Mathieu Galmes ran numerous CFD simulations providing the platform for the wheel improvement modelling. Thanks also to visiting researcher Nathalie Labonnet who assisted with developing the method for modelling the 3-spoke wheel using finite elements.

With such a large experimental component to this project I am indebted to several of the Mechanical Engineering Department technical staff. Thanks to Graeme Harris for his assistance and encouragement while setting up the test rig and running experiments.

Thanks also to Paul Wells in the workshop for his attention to detail and insightful suggestions when manufacturing the rig.

To my officemates – Laura and Lisa. Thanks for providing such an enjoyable and supportive office atmosphere. I will miss the constant opportunity for girly chats when I return to the male dominated consulting engineering world!

To my family – Mum, Dad, Sam and Matt. Thanks for all the support you have given me over the years while I have been a tertiary student. Thank you, Mum, for all the pep talks when I was feeling under pressure with workload.

Finally, I must thank my partner, Jonny. Thank you for the love and support you have given me for the last six years and especially while I have been studying for this degree.

# Abstract

This thesis presents the work undertaken to assess potential improvements in high performance bicycles. There are several wheel options available for elite riders to use in competition and this research has investigated the aerodynamic properties of different wheel types. The research has also developed CFD and FEA models of carbon fibre bicycle wheels to assist in the wheel improvement process.

An accurate and repeatable experimental test rig was developed to measure the aerodynamic properties of bicycle wheels in the wind tunnel, namely translational drag, rotational drag and side force. Both disk wheels and spoked wheels were tested.

It was found that disk wheels of different hub widths have different aerodynamic properties with the 53mm wide Zen disk wheel requiring the lowest total power of the wheels tested. There was little difference between the translational power requirements of the wheels but there was greater variation in the rotational power requirements.

Compression spoked wheels of 3 and 5 spokes were found to require less power than wire spoked wheels. There was little difference between the total power requirements of the compression spoked wheels tested, with the differences at 50km/hr being less than the experimental uncertainty.

The Zipp 808 wheel demonstrated considerably lower axial force than all other wheels at 10° yaw angle, confirming Zipp's design intention to have optimum wheel performance between 10-20°. The Zen 3-spoke wheel showed the lowest axial drag and side force at yaw of the compression spoked wheels tested and had similar side force results to the Zipp 808.

CFD models of the disk and 3-spoke wheel achieved good agreement with the experimental results in terms of translational drag. Rotational drag did not agree so closely, most likely due to the turbulence model used being designed for higher Reynolds number flows.

A FE model of the disk wheel was validated with experimental testing. In order to simplify modelling, the FE model of the 3-spoke wheel did not include the hub, which led to a large discrepancy with the experimental results for the particular loading scenario.

The experimental rig and CFD models were used to develop aerodynamic improvements to the wheel and the FE models were used to identify the implication of geometric changes to the wheel structural integrity. These improvements are not reported in detail in this thesis due to the results being commercially sensitive.

Chapter 1

# Introduction

## 1.1 History of Bicycle and Wheel Development

The development of the bicycle can be traced back as far as 1817 when Baron Karl von Drais of Mannheim, Germany invented his two wheeled 'running machine'. Von Drais' machine included side panniers and wheels of 690 mm diameter (27 inches) and was imitated and further developed by others including Denis Johnson, a coachmaker who decided that a mainly iron frame was more convenient than a wooden frame. After some initial scepticism, it was demonstrated that Von Drais' machine (called "le velocipede" in Paris where it was patented) could exceed the speed of runners and horse-pulled post carriages even over journeys of up to three hours (Wilson, 2004). These early machines incorporated wooden compression spoked wheels designed similarly to those used on horse-drawn carriages and trains.

Following Von Drais, several other major steps in the development of the bicycle occurred. Firstly, pedals were added to create propulsion during the 1860s. This led to the first 'bicycle boom' starting in Paris and spreading to Belgium, the Netherlands, Germany, Britain and the United States (Wilson, 2004). During this time, rubber was first fastened to the rims of the wheels and ball bearings were first used in bicycles to provide easier running. The tension wheel was developed in Paris in 1869-1870 and in 1874

Starley patented the tangent-tension method of spoking which has since remained the standard spoking method (Wilson, 2004). With the development of tension-spoked wheels, the front wheel of bicycles was made larger to give a longer distance per pedal revolution resulting in greater speed. This resulted in the Penny Farthing bicycle which was popular in the 1870s.

The final development of the bicycle to the form we recognise today is the invention of the safety bicycle. The safety bicycle utilised two wheels of a similar, moderate diameter (in contrast to the Penny Farthing) with the rider seated between the two wheels and also included rubber tyres, variable gears and tubular frames, all common components of a modern bicycle. The pneumatic tyre was patented in 1888 by John Dunlop and was used successfully in racing for the first time in 1889. This racing success, and the increased comfort, safety and cycling performance of the pneumatic tyre assured it of a permanent place on the bicycle and solid rubber tyres were soon phased out (Wilson, 2004).

### 1.2 Current Wheel Designs and Applications

Today, bicycle wheels can be separated into three distinct groups: tension spoked wheels, compression spoked wheels and disk wheels. The choice of wheel to use is based on the riding conditions, the type of race and whether the wheel is to be used on the front or back of the bicycle.

The initial development of the bicycle wheel was from a compression spoked wheel, as was common on carriages, to the tension-spoked wheel found on most bicycles today.

There are several features of a tension spoked wheel which can be modified to alter the aerodynamic performance of the wheel. Firstly, the spoke count can vary significantly between wheels, with the standard tension spoked wheel having 36 spokes and the WH-R561 model by Shimano having just 16 spokes (Shimano, 2006). The shape of the spoke can also differ, with some wheels have round wire spokes and some wheels have spokes resembling blades of 4-5mm depth. The depth of the rim is different on many wheels. Some of the best tension spoked wheels currently available are manufactured by Zipp and have carbon fibre rims ranging from 33mm to 108mm (Zipp, 2008). Tension spoked wheels with metal rims are generally the most affordable wheel option for cyclists and are usually the default wheel set offered on a new bike.

The compression spoked wheel has reappeared with the development of wheels manufactured from carbon fibre. The first of these wheels was developed by DuPont/Specialised in 1989 (Hopkins et al, 1990). The use of carbon fibre allows the wheels to have as few as three spokes in compression with superior strength, stiffness and far lighter weight than their wooden predecessors in the 1800s. Wheels with three, four and five spokes are common on the bicycles of top level cyclists.

The final common type of wheel is the disk wheel which initially simply utilised covers of the same diameter as the wheel fitted over the tension spokes to reduce the drag as the spokes rotated. With the introduction of carbon fibre to wheel manufacture, the need for internal spokes has disappeared and the disk itself now takes the loading on the wheel. Disk wheels can have flat, convex or lenticular sides and different hub widths. Disk

wheels are most commonly used indoors at velodromes where side winds, which can affect the wheels greatly due to their large side area, are not present. In outdoor events, the disk wheel is most commonly used as a back wheel. As a front wheel, the cross wind on the disk wheel significantly affects steering because the wheel centre of pressure is ahead of the steering axis.

### 1.3 Research Objectives

Several key objectives were identified at the beginning of the research period:

- Designing an experimental rig to effectively measure linear and rotational drag
- Predicting the aerodynamic efficiency of bicycle wheels
- Gain knowledge of the performance of different wheels at varying wind angles
- Predicting the stiffness of wheels from finite element simulations

Underpinning these objectives was the desire of Dynamic Composites to understand how their wheels performed compared to their main competitors and whether their wheel designs could be further improved for enhanced aerodynamic performance. This thesis documents how the above research objectives were achieved and briefly describes the resulting recommendations for wheel improvements which were supplied to Dynamic Composites for use in their wheel development programme.

### 1.4 Thesis Organisation

Chapters 2-5 of this thesis have been divided correlating to the several distinct areas of work encountered in this research: aerodynamics, experimental testing, computational

fluid dynamics and finite element analysis. Chapters 6-7 outline the analysis of the existing wheels including experimental testing, CFD analysis and FE analysis. Chapters 8 and 9 contain the research conclusions and suggestions for future work. The thesis utilises APA referencing and a full reference list is located after Chapter 9.

Chapter 2

# Fundamentals of Bicycle Wheel Performance

## 2.1 Introduction

For optimum performance, a bicycle wheel should have low aerodynamic drag, high stiffness, low weight and low moment of inertia. Aerodynamic drag is important to all riders and it is directly related to the amount of effort that must be expended by the rider to make the bicycle move. Weight is also important to all riders but is especially important for road racers who may gain significant elevation during hill stages of an event. The moment of inertia is important in sprint events where the rider's ability to accelerate the bicycle up to speed quickly is required (Moore et al, 2008).

## 2.2 Aerodynamic Factors

There are two components of aerodynamic drag which combine to give the total drag of a bicycle wheel: translational aerodynamic drag and rotational aerodynamic drag.

### *2.2.1 Translational Aerodynamic Drag*

Translational aerodynamic drag is the drag force on the wheel due to the wheel moving in a straight line through the air (sometimes referred to as linear drag). Translational aerodynamic drag ($F_D$) is given by:

$$F_D = \frac{1}{2} C_{d,trans} A_{wheel,\,frontal}\, r v^2 \qquad (1)$$

where $C_{d,trans}$ is the translational drag coefficient, $A_{wheel,frontal}$ is the frontal area of the wheel ($m^2$), $\rho$ is the air density ($kg/m^3$) and v is the linear velocity (m/s).

### *2.2.2 Rotational Aerodynamic Drag*

Rotational aerodynamic drag is the drag force due to rotating the wheel about its axle through the air. Rotational aerodynamic drag ($F_R$) is given by:

$$F_R = \frac{1}{2} C_{d,rot} A_{wheel,side} r w^2 r^2 \quad (2)$$

where $C_{d,rot}$ is the rotational drag coefficient, $A_{wheel,side}$ is the side area of the wheel ($m^2$), $\rho$ is the air density ($kg/m^3$), $\omega$ is the angular velocity (radians/s) and $r$ is the wheel radius (m).

## 2.3 Weight Factors

The effect of wheel weight contributes to the energy needed to lift the wheels to high elevation during mountain races, the rolling resistance of the tyre and bearings and the moment of inertia of the wheels. For a bicycle riding on flat ground, the rolling resistance of the tyre is given by:

$$F_{rr,tyre} = C_{rr,tyre} N_{tyre} \quad (3)$$

where $C_{rr,tyre}$ is the coefficient of rolling resistance of the tyre and $N_{tyre}$ is the force being applied normal to the tyre. Similarly, the rolling resistance in the wheel bearings is given by:

$$F_{rr,bear} = C_{rr,bear} N_{bear} \quad (4)$$

where $C_{rr,bear}$ is the coefficient of rolling resistance of the bearings and $N_{bear}$ is the force being applied radially through the bearings.

### 2.4 Importance of Wheel Drag

Due to the aforementioned forces experienced by the wheel, power is absorbed by a wheel through six mechanisms:

1. Translational acceleration of the wheel centre of mass in the direction of travel:

$$P_{transacc} = m_{wheel} v \frac{dv}{dt} \tag{5}$$

2. Angular acceleration of the wheel:

$$P_{rotacc} = I_{wheel} w \frac{dw}{dt} \tag{6}$$

($P_{transacc}$ and $P_{rotacc}$ are zero for a bicycle moving at constant speed.)

3. Translational aerodynamic drag:

$$P_{ltransdrag} = C_{d,trans} A_{wheel,frontal} \frac{1}{2} r v^3 \tag{7}$$

4. Rotational aerodynamic drag:

$$P_{rotdrag} = C_{d,rot} A_{wheel,side} \frac{1}{2} r w^3 r^3 \tag{8}$$

5. Rolling resistance between the tyre and the road:

$$P_{rr,tyre} = C_{rr,tyre} N_{tyre} v \tag{9}$$

6. Rolling resistance in the bearings:

$$P_{rr,bear} = C_{rr,bear} N_{bear} w r_{bear} \tag{10}$$

The total power absorbed by a wheel is the sum of the components in Eqs. 5-10. These components cannot all be easily expressed as forces without defining at the same time a radius or distance; however they can all be expressed as power and summed to determine the total power absorbed.

This section will compare the power absorbed by the wheels with power absorbed elsewhere while riding at constant speed alone or at the front of the peleton.

The power absorbed by the aerodynamic drag of the whole system (bicycle and rider) is given by:

$$P_{cycle+rider} = C_{d,bicycle+rider} A \frac{1}{2} r v^3 \qquad (11)$$

where A is the frontal area of the rider and bicycle and $C_{d,bicycle+rider}$ is the drag coefficient of the bicycle and rider taken as $0.4m^2$ and 0.85 respectively from measurements of male athletes of average size in the University of Canterbury wind tunnel using carbon-fibre time-trial bicycles, aero-bars and aero-helmets. The results are presented in Table 2.1.

**Table 2.1** – Estimates of power absorbed by aerodynamic drag of rider, frame, wheels and rolling resistance.

| | Power absorbed by: | | | |
|---|---|---|---|---|
| Speed (kmhr) | Drag of cycle + rider (W) | Total aerodynamic drag of wheels (W) | Rolling resistance of wheel (W) | Rolling resistance of bearings (W) |
| 30 | 123.0 | 10.4 | 19.7 | 0.24 |
| 40 | 291.5 | 21.6 | 26.2 | 0.33 |
| 50 | 569.3 | 38.0 | 32.7 | 0.41 |

The power absorbtion values above relate to a 75kg person riding an 8kg bicycle. The coefficient of rolling resistance for the tyre was taken to be 0.0029. The coefficient of rolling resistance for the bearings was taken as 0.001 (Wilson, 2004).

**2.5 Kinetic Energy of Bicycle and Rider System**

It is also interesting to note the contribution that the rotating wheels make to the overall kinetic energy of the system. This is important as it indicates the overall inertial effect of the wheels compared to the bicycle frame and rider. The total kinetic energy of the bicycle and rider system is:

$$KE_{total} = KE_{wheels} + KE_{frame} + KE_{rider} + KE_{movinglegs} \quad (12)$$

The kinetic energy of the wheels has both translational and rotational components and the kinetic energy of the frame and rider is translational.

$$KE_{wheels} = \frac{m_{wheel}v^2}{2} + \frac{I_{wheel}w_{wheel}^2}{2r_{wheel}^2} \quad (13)$$

Where $m_{wheel}$ is the wheel mass (kg), v is the translational velocity (m/s), $I_{wheel}$ is the mass moment of inertia of the wheel, $\omega_{wheel}$ is the angular velocity of the wheel and $r_{wheel}$ is the wheel's radius.

$$KE_{frame} = \frac{m_{frame}v^2}{2} \quad (14)$$

Where $m_{frame}$ is the mass of the bicycle frame (kg) and v is the translational velocity (m/s).

$$KE_{rider} = \frac{m_{rider}v^2}{2} \quad (15)$$

Where $m_{rider}$ is the mass of the rider (kg) and v is the translational velocity (m/s).

The kinetic energy of the moving legs is the sum of the kinetic energy of the foot and calf which are moving in elliptical paths and the thigh which is acting as a pendulum.

$$KE_{movinglegs} = \frac{I_{foot} w^2_{cadence}}{2r^2_{foot}} + \frac{I_{calf} w^2_{cadence}}{2r^2_{calf}} + \frac{I_{thigh} w^2_{cadence}}{2r^2_{thigh}} \quad (16)$$

where:

$$I_{foot} = m_{foot} r^2_{foot} \quad (17)$$

$$I_{calf} = m_{calf} r^2_{calf} \quad (18)$$

$$I_{thigh} = m_{thigh} L^2_{thigh} \quad (19)$$

In the above equations, $m_{foot}$, $m_{calf}$ and $m_{thigh}$ are the respective masses of the leg sections. Based on anthropometric data for a 75kg rider, the masses are 1.09kg, 3.49kg and 7.5kg respectively (Grimshaw, 2007). Video data of a 60kg rider and a 90kg rider was analysed to find the radius of gyration for the foot ($r_{foot}$) and calf ($r_{calf}$) and pendulum length for the thigh ($L_{thigh}$). The cadence velocity ($\omega_{cadence}$) was taken as 100rpm which is a standard cadence rate for competitive cyclists. For the calculations, the frame mass plus accessories such as drink bottles was taken to be 8kg and the mass of each wheel was based on a Zen wire-spoke wheel and was taken to be 0.51kg. The moment of inertia for a wire-spoke wheel was simply based on a circular hoop of 0.51kg rotating about a 0.333m radius (to simulate a typical wire-spoke wheel).

**Table 2.2** – Kinetic energy estimates of bicycle and rider system

| Speed (kmhr) | $KE_{wheels}$ (J) | $KE_{frame}$ (J) | $KE_{rider}$ (J) | $KE_{moving\ legs}$ (J) | $KE_{total}$ (J) |
|---|---|---|---|---|---|
| 30 | 53 | 278 | 2604 | 122 | 3057 |
| 40 | 94 | 494 | 4630 | 122 | 5340 |
| 50 | 148 | 772 | 7234 | 122 | 8275 |

The kinetic energy of the wheels is between 5.4-6.0% of the total kinetic energy. This indicates that when a rider is attempting to accelerate the bicycle, only a small amount of their effort is required to accelerate the wheels, most of their effort is used in accelerating themselves and the bike frame. This implies that while it is optimal to have the wheels as with as low a mass as possible, the gains to be made in terms of acceleration ability as small. Similar gains can be made by reducing the frame and accessory mass by the same amount and more significant gains can be made by increasing the rider's power-to-weight ratio.

As the kinetic energy of the rotating legs is based on pedalling cadence, assuming a cadence of 100rpm is maintained at all velocities via different gearing, the kinetic energy of the legs remains constant at all velocities.

### 2.6 Previous Research on Wheel Aerodynamics

The significant work over the past century on the aerodynamics of the whole rider/bicycle combination is reviewed by Wilson (2004), Kyle and Weaver (2004) and Kyle and Burke (1984). The aerodynamics of the wheel alone has received less attention until recently.

Zdravkovich (1992) reviewed early $20^{th}$ century work on reducing the drag of fixed undercarriage aeroplane wheels, and work on inhibiting the formation of trailing edge vortices with splitter plates, which can reduce drag. Zdravkovich tested wire spoked

wheels and frames with splitter plates inside the rim, similar to a deep rim. Measuring translational drag and side force, plates with a chord length equal to twice the depth of the tyre and rim were found to reduce the drag by ~5%. This weak reduction in drag was attributed to the low contribution of vortex shedding to the total linear drag of the wheel. The splitter plate was a thin plate rather than a profiled deep rim as seen on more recent wheels.

Hopkins et al. (1990) measured rotational and translational drag in wind tunnel tests on a Specialized 3-spoke aero wheel, and also on flat rim and deep rim spoked wheels, lenticular discs and flat discs. Translational drag was measured with a strain ring and rotational drag by motor power consumption. They state that rotational drag comprised 10-20% of the total wheel drag.

Kyle and Burke (1984) report wind tunnel and coast down tests of faired and unfaired wheels. Translational drag only was measured in the wind tunnel tests, and the rotational drag was inferred from the difference in drag measured in the coast down and wind tunnel tests. They estimated rotational drag to be 20% of the total drag for an unfaired wheel, 50% for a faired wheel, at 24km/hr.

Sayers and Stanley (1994) measured the translational drag of three wheels in a wind tunnel at wind speeds up to 72km/hr and rotational speeds up to the equivalent of 60km/hr ground speed. The wheels tested were a 16mm wide disc wheel; a 36-spoke wire wheel with partial and full cladding; and a deep rim aero wheel. The deep rim wheel

showed the greatest drag of those tested. At ≥54km/hr the fully clad and disc wheels had similar drag coefficients. The authors found a marked difference between the translational drag measured on a rotating wheel and the translational drag on Zdravkovich's stationary wheels (1992). They also explored the effect of head and tail winds.

Tew and Sayers (1999) extended this work to include yaw, comparing a standard wire spoked wheel with few aerodynamic features to a Campagnolo Shamal wire spoked wheel, Mavic Cosmic, Spinergy, Specialized Trispoke compression spoked wheels and a disc wheel. At zero yaw the aero wheels showed 60% less translational drag than the standard wire spoked wheel, and the disc 70% less. Sunter and Sayers (2001) measured the drag of a range of mountain bike tyres.

Greenwell et al. (1995) measured linear drag, side force and yawing moment of a number of wheels in a wind tunnel. The wheels tested included HED and ZIPP 950 disc wheels, Specialized Ultralight and FiR Trispoke three-spoke wheels, and Campagnolo Shamal and HED CX wire spoked wheels. They found all the aero wheels (i.e. disc, compression spoke and deep rim wire spoke) had ~25% less translational drag than conventional shallow rim spoked wheels, and that the drag, side force and yaw moment coefficients were largely independent of wheel rotational speed.

Less detailed than the studies mentioned above, Daugherty (1983) reports drag forces for a single wheel at a single speed.

Besides these studies in peer-reviewed journals there are a number of reports on manufacturer's websites and in bicycle magazines. The wheel manufacturer Zipp measured the linear and rotational aerodynamic resistance of a number of their wheels (Zipp, 2006). Assuming the rotational and translational measurements are at the same speed, their measurements on wire spoke wheels show that the rotational power is around 60-70% of the total power dissipation.

Roues Artisanales (2008) measured the drag of a large number of wheels at 50km/hr in the wind tunnel of the Technical University of Lyon in 2006 and again in 2008. Tour magazine (Kühnen, 2005) also tested a range of wheels. Bike Tech Review (Willett, 2006) compared the Zipp 808 and the Specialised Trispoke wheels in the San Diego Low Speed Wind Tunnel and found the wheels to have similar power requirements over a range of yaw angles.

Chapter 3

# Wind Tunnel Testing

## 3.1 Introduction

A major objective of this project was to develop an accurate and repeatable method of measuring the aerodynamic properties of bicycle wheels. An experimental rig was designed and installed in the wind tunnel at the University of Canterbury. This chapter will explain the features of the rig and the testing methodology.

## 3.2 Wind Tunnel Facility

The Mechanical Engineering Department of the University of Canterbury has two wind tunnels in its aerodynamics laboratory. This project utilised the high speed, closed circuit wind tunnel. The wind tunnel has a working section of 900mm x 1200mm. The settling chamber, screens and contraction generate a uniform flow in the test section except for a boundary layer ≈50mm thick at the beginning of the test section. The turbulence level was measured with a hot wire anemometer to be 0.5% at a speed of 50km/hr (Moore et al, 2008).

**Figure 3.1** University of Canterbury closed circuit wind tunnel

### 3.3 Test Rig

The test rig is mounted on top of the wind tunnel and consists of two horizontal steel frames connected to each other and to a base plate via aluminium flexures, forks to hold the wheel in place in the tunnel and a motor and driver arm system to enable rotation of the wheel. The forks are covered with carbon fibre fairings to replicate the aerodynamic forks found on racing bicycles. Three loads cells are fixed to the rig to measure axial force, side force and motor torque.

Fackrell and Harvey (as cited in McManus & Zhang, 2006) found that the wake of a rotating wheel was taller and narrower than that of a stationary wheel. The taller wake

was deemed to be due to earlier separation. Therefore, in order to gain the most accurate aerodynamic data, the wheel must be rotating.

The wheel sits less than 2mm above a fixed plane used to simulate the road surface. In reality, there is no boundary layer on the road as a wheel rolls along it, so using the floor of the wind tunnel, where a boundary layer is present, as a ground plane is not appropriate. The false ground plane begins 600mm upwind of the wheel and a boundary layer does not form. The fact that the ground plane is not moving is not representative of reality. Stapleford (as cited in Zhang et al, 2006) found that the true operating conditions of a wheel require that the wheel is rotating and is in contact with the ground. However, he also stated that a moving ground surface does not significantly improve the simulation and can have a detrimental effect on the flow representation if it is employed with a gap between the wheel and the ground. Therefore, it was decided to concentrate on developing a test rig that rotated the wheel and accurately measured its aerodynamic properties and leave the moving ground plane for a future research project.

**Figure 3.2** PC, data acquisition unit, manometer and wind tunnel speed controller

**Figure 3.3** PC, test rig, rig motor controller and wheel

**Figure 3.4** Test rig with wheel mounted in wind tunnel

**Figure 3.5** Test rig and motor controller atop wind tunnel

### *3.2.1 Axial Force Measurement*

The top steel frame of the rig is connected to the lower frame by aluminium flexures. The flexures enable the top steel frame to move in an axial (backward) direction relative to the lower frame when a force is applied on the forks. A force point is fixed at the rear of the top frame and puts pressure onto a load cell which is mounted on the lower frame.

This load cell measures the force being applied on the wheel when air is flowing in the wind tunnel.

The linearity of the load cell measurement was checked using several masses between 50g and 1000g (the load cell capacity). The correlation between the measured strain and the hanging mass was linear. Therefore, using two masses to reduce calibration time was acceptable.

### *3.2.2 Side Force Measurement*

The lower steel frame of the rig is connected to the top frame and the base plate also using aluminium flexures. The flexures are orientated to allow the lower frame to move in a sideways direction when a side force is applied on the forks. A force point is fixed on the right hand side of the frame and puts pressure onto a load cell which is mounted to the base plate. This load cell measures the side force being applied to the wheel when it is placed in the wind tunnel at some yaw angle to the airflow.

### *3.2.3 Motor Torque Measurement*

An aluminium “arm” screwed to the end of the motor terminates with a point that rests on a load cell. When the motor is operating, the arm stopping on the load cell opposes the tendency for the motor to spin in the opposite direction to the shaft. The motor torque is calculated using the force transferred to and measured by the load cell and the arm length.

### *3.2.4 Effect of Bearing Resistance and Rolling Resistance on Results*

The contribution of bearing resistance and rolling resistance to the total rotational power was assessed. The power requirement for the bearings in the wheel and the test rig at 50km/hr was calculated using equation 10 to be 0.1W. This value is smaller than the uncertainty of the rotational power measurement (~1.0W at 50km/hr) so the bearing power loss can be neglected. To minimise the potential for axial bearing loads due to over-tightening the nuts holding the wheel in the forks (and consequently shortening the axle), the nuts were tightened to 40lbs/in on every wheel. This level of torque is less than the torque recommended by Zipp (2007) to eliminate axial bearing loads (50lbs/in) so it is considered that axial bearing loads are not present in the rig and are not a source of power dissipation.

The rolling resistance between the drive belt and the tyre at 50km/hr was calculated using equation 9 be 0.13W, which is less than the uncertainty of the rotational power measurement so it too can be ignored in terms of affecting the rotational power reading.

## 3.3 Calibration Procedure

The required load cells for each test were individually calibrated before each run. The calibration was then checked at the end of each run to ensure that any shift in the load cell reading from the start of the test to the end was below a reasonable level (within +/- 2g).

### *3.3.1 Axial Force Load Cell*

The axial force load cell is calibrated by hanging 100g and 400g masses on a string which is connected horizontally to the top frame and runs over a pulley. This simulates a 100g and 400g mass being applied in the axial direction. The strain measured by the load cell is read and recorded using LabView$^{TM}$. These readings are then used as the values between which to interpolate when the load cell experiences a strain due to the axial force on the wheel.

### *3.3.2 Side Force Load Cell*

The side force load cell utilises a lever system for calibration as the position of the load cell meant that weights could not be hung over a pulley to calibrate in the same manner as the axial force load cell. The lever arm has a vertical member which presses on the back end of the side force point which is mounted on the lower frame. 500g, 1kg and 2kg masses are placed on the horizontal member of the lever arm which causes the vertical member to put pressure on the force point. By summing moments to zero about the lever fulcrum, and using the respective member length, the force being applied to the side force load cell is known. The 500g, 1kg and 2kg masses equate to 1.522kg, 3.042kg and 6.090kg and these known masses are related to the strains measured by the load cell and can be used to calculate the force when a side load acts on the wheel in the wind tunnel.

### *3.3.3 Motor Torque Load Cell*

The motor torque load cell is calibrated by holding the torque arm off the load cell and measuring the strain when there is zero load, 50g and 100g masses acting on the load cell. The actual experimental force reading is then calculated from the experimental strain by interpolating within the known strains and loads.

### *3.3.4 Data Acquisition System*

A National Instruments$^{TM}$ cDAQ-9172 unit was used for acquisition of data from the three load cells. The DAQ unit reads the strains from each load cell and then sends them to the LabView$^{TM}$ software. Figure 3.6 Shows the LabView$^{TM}$ block diagram that was created to record the strains and output the results to text files. The text files were imported to Microsoft Excel$^{TM}$ where the strains were converted to grams of drag based on the calibration data.

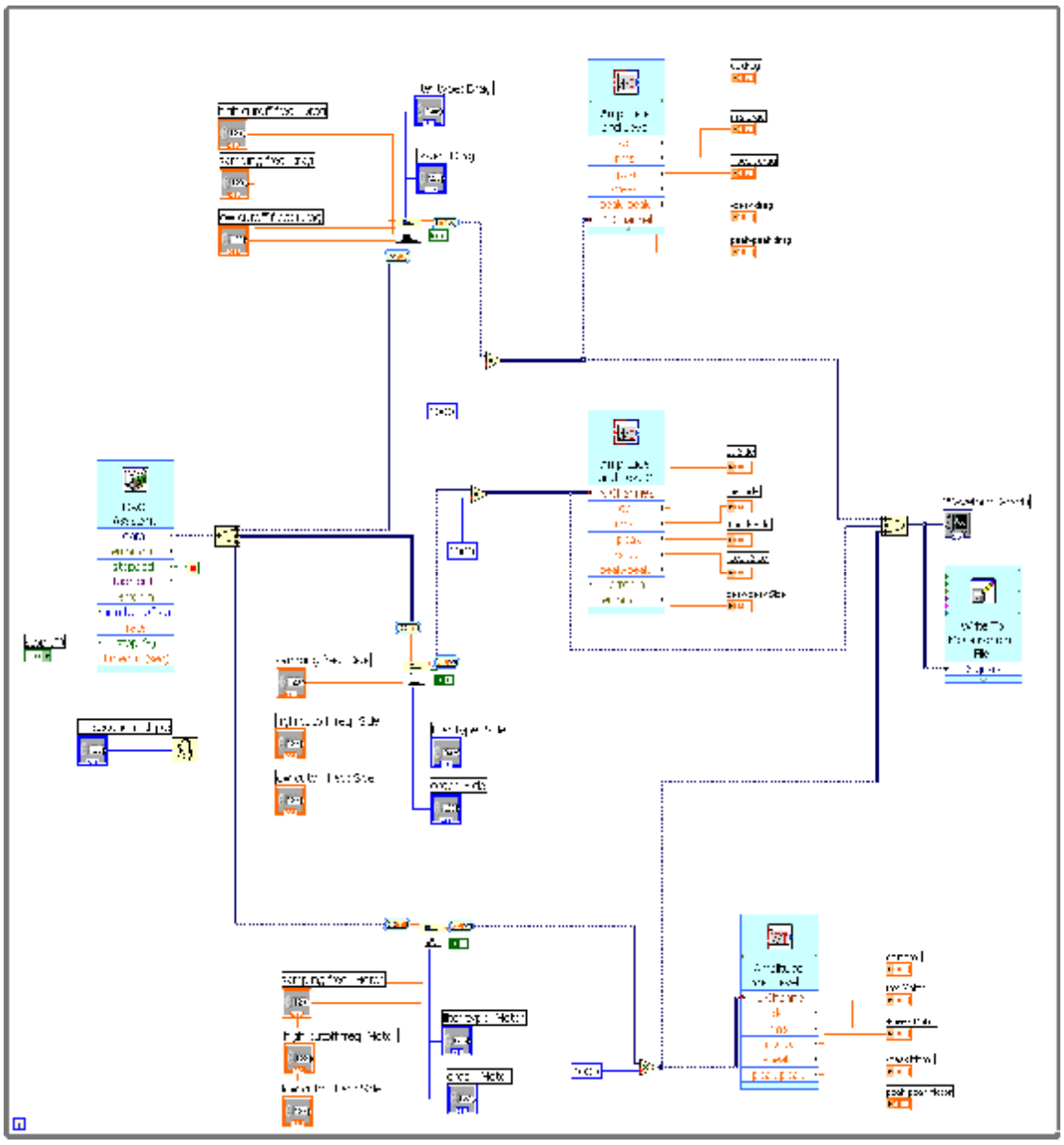

**Fig 3.6** – Labview™ block diagram for data acquisition system

Figure 3.7 shows the LabView™ front screen in which the user inputs the data acquisition settings (frequency, filters etc) and the measured strains of each load cell are displayed in real-time.

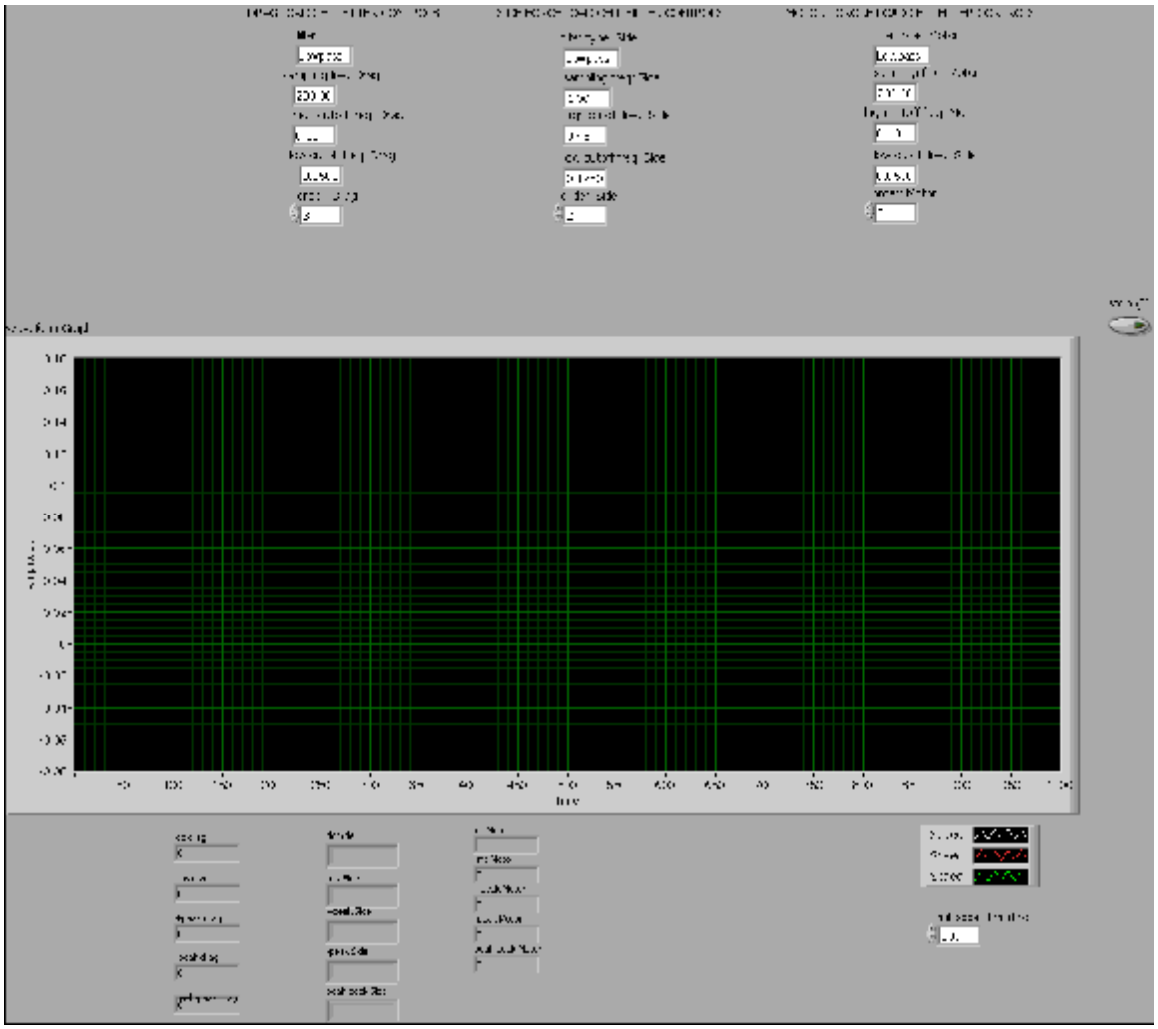

**Fig 3.7** – LabView™ front screen for data acquisition system

### *3.3.5 Motor Speed Control*

The motor speed was controlled using the program DES UserInterface Version 1.15 which was developed by the motor's manufacturer, Maxon. It was independent of the data acquisition system.

## 3.4 Test Procedure

All tests were conducted at the appropriate wind tunnel velocity based on the wheel rotational speed, atmospheric pressure and wind tunnel airflow temperature. The pressure and temperature readings were checked every 30 minutes to ensure that atmospheric and wind tunnel motor temperature changes were not affecting the measurements.

### *3.4.1 Linear Drag Force and Rotational Motor Torque Testing*

The linear drag force and rotational motor torque testing consisted of the following steps:

- Calibrate the motor torque load cell
- Set the wheel motor running at the appropriate speed for the wheel linear velocity to match tunnel velocity (initially 30kmhr)
- Calibrate the axial force load cell
- Set the wind tunnel running at the desired velocity
- Take five test readings of approximately 20 seconds each. Between each reading, decrease the wheel motor speed by 1000RPM and then accelerate back to test speed.
- After five readings have been taken, turn off the tunnel
- When the tunnel velocity has reached zero, repeat the axial force load cell calibration procedure and then turn the wheel motor off
- With the wheel now stationary, repeat the motor torque load cell calibration procedure. END OF TEST.

The above test procedure was then repeated for wheel and tunnel velocities of 40kmhr and 50kmhr.

### *3.4.2 Yaw Testing*

The experiments to assess the effect of having wind impacting on the wheels at varying yaw angles were based on experiments conducted by Tew and Sayers (1999).

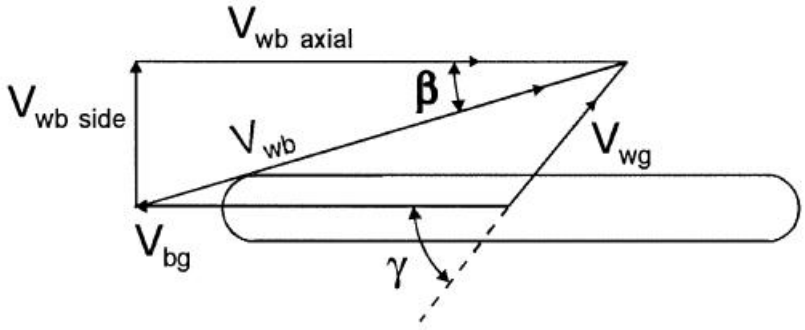


**Fig 3.8** – Velocity vectors for bicycle wheel (Tew & Sayers, 1999)

The experiment required that $V_{wb\ axial} = V_{bg}$ meaning that the axial wind speed is equal to the bicycle speed. This results in the velocity of the wind with respect to the ground being perpendicular to the axial velocity at all times.

The experiments were conducted as follows:

- Set the base plate at the desired yaw angle (initially 10°)
- Set the wheel motor running at the appropriate speed for the wheel linear velocity to match tunnel velocity (initially $V_{wb}$ axial = 30kmhr)
- Calibrate the axial force load cell
- Calibrate the side force load cell
- Set the wind tunnel running at the desired velocity
- Take a test reading of approximately 20 seconds

- Turn of the wind tunnel
- When the tunnel velocity has reached zero, repeat the axial force load cell and side force load cell calibration procedures and then turn the wheel motor off. END OF TEST

The above test is then repeated for $V_{wb}$ axial velocities of 40kmhr and 50kmhr and yaw angles of 20°, 30°, 40° and 50°.

### *3.4.3 Bare Rig Tests*

The axial drag and side force exerted on the rig was measured by performing the tests outlined in sections 3.4.1 and 3.4.2 with no wheel in the forks. This meant that the only items in the wind tunnel experiencing and transmitting a force to the load cells due the airflow were the forks and the driver arm. These 'bare rig' forces could then be subtracted from the forces measured for each wheel so that only the forces acting on the wheel remain.

The bare rig motor torque (the torque required to rotate the drive shaft, pulley and rig bearings) was measured by fixing the driver arm in the same location as if it were resting of the tyre. The load cell was calibrated and the motor was then set to run at each of the test speeds. Motor torque readings were taken at each speed and this torque was then subtracted from the wheel motor torque measurements.

Chapter 4

# Computational Fluid Dynamics

## 4.1 Introduction

Computational fluid dynamics (CFD) is a powerful tool available for the analysis of fluid flows and their interaction with objects. In this project, CFD was used to simulate the bicycle wheel rotating in the wind tunnel. Changes to the existing wheel geometry were made in computer aided design (CAD) software and then applied in the CFD models. The CFD simulations were used to estimate the effect of the changes on aerodynamic drag. This shortened the duration of the development process compared to designing, building and testing multiple physical models.

## 4.2 Model Creation

The geometry of the existing Dynamic Composites wheels was available in CAD format using the software Solidworks™.

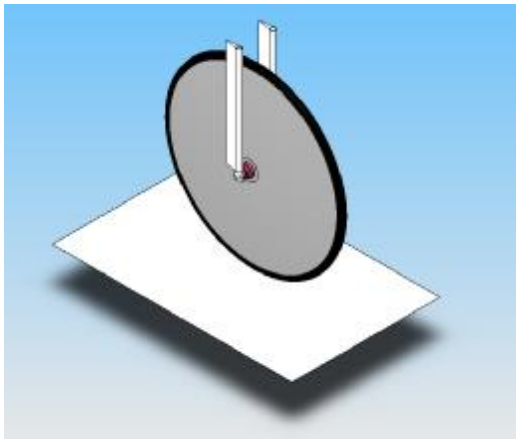

**Figure 4.1** Solidworks™ assembly of wheel and forks

To accurately represent the wind tunnel experiments, the model geometry contained:

- The wheel including tyre, hub caps and axle
- The steel forks and fairings
- The false ground plane mounted in the tunnel

The Solidworks™ assembly was then converted to STL files for importing into the meshing software.

### 4.3 Meshing

Fluid dynamics is governed by the equations of continuity, momentum and energy. In CFD, these governing equations are replaced by equivalent numerical descriptions which are then solved at discrete points (nodes) in the flow field using numerical techniques. Information on the dependent variables (velocity, pressure etc) can be gained from these numerical solutions at each node (Massey, 1998). The location of the nodes is governed by a 'mesh' which is created within the flow domain.

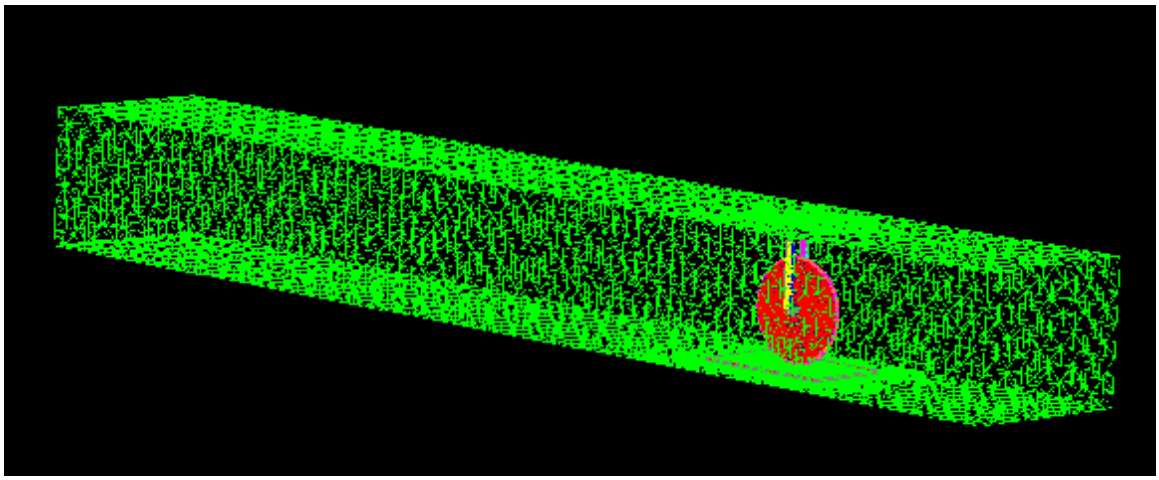

**Figure 4.2** Model mesh created in Harpoon™

The mesh was created using the software, Harpoon™. The geometry STL files were imported and the boundary limits were set to mimic the dimensions of the wind tunnel used for the force measurements. The flow domain extended 3 wheel diameters upstream of the wheel and 8 wheel diameters downstream. The flow domain was 1200mm wide x 910mm high x 8000mm long, which was sufficient to encompass all aspects of the flow around the wheel (separation of the flow around the hub and wake behind the wheel etc).

The flow domain was meshed using tetrahedral elements. Both hexahedral and tetrahedral elements were investigated to determine which would provide the most accurate results. CFD models using both element types were solved and compared to the experimental results, with the tetrahedral element model providing the best agreement.

It was initially intended to mesh the flow domain using the software Gambit™. However, Harpoon™ was found to be more appropriate in this application as the mesh generation time was significantly shorter and Harpoon™ proved more able to cope with the complex

geometry around the wheel hub. Fewer meshing errors and skewed elements were created when using Harpoon$^{TM}$ than when using Gambit$^{TM}$.

Harpoon$^{TM}$ provides several user options when generating the mesh. The meshes were generated using external meshing so that as the flow domain around the wheel was meshed, the growth rate was set to slow to give a smooth mesh and hanging nodes were removed.

### 4.4 Mesh Convergence

A mesh convergence study was performed to identify the correct size of mesh to use in the analysis. Generally, with a finer mesh there are more nodes present which can yield a more accurate solution. However, as the number of nodes increases, the computation time also increases so there is usually a mesh size limit based on the computing power or memory available. The mesh convergence study involved creating meshes in the flow domain with increasing numbers of nodes and calculating the solution. The disk wheel geometry was used for the analysis and it was assumed that the findings could be transferred to the spoked wheel models without detrimental effects to the solution accuracy. When the surface mesh size decreased from 3.125mm to 2.5mm (6,166,508 Nodes to 9,137,746 nodes) the resulting force on the wheel at 50km/hr only changed by 0.93%. This change is acceptable so a mesh containing surface nodes of 3.125mm was considered to be sufficiently accurate and had a shorter solution time than the finer, 2.5mm surface size mesh.

**Table 4.1** – Mesh convergence study results

| Surface Size (mm) | No. of nodes | Total Force (N) | Change (%) |
|---|---|---|---|
| 12 | 516370 | -2.154 | |
| 6.5 | 1747426 | -1.852 | -14.0 |
| 4 | 3961374 | -1.572 | -15.1 |
| 3.125 | 6166508 | -1.438 | -8.5 |
| 2.5 | 9137746 | -1.425 | -0.9 |

During the mesh convergence study, the difference between two turbulence models (k-ε and k-ω SST) was also investigated. The k-ω SST model was found to better reproduce the experimental results and is further explained in section 4.7.

### 4.5 CFD Software

After the mesh was created it was then exported for analysis within the CFD program Fluent™. Fluent™ calculates the solution of the numerical fluid dynamic equations at every element until the difference between the numerical solution and the exact solution is below as certain target point, known as the residual. For the analysis, a target normal residual of 0.0001 was used for all variables as the change in solution was negligible when residuals of 0.00001 were employed but the computation time to achieve the better agreement with the exact solution was approximately double the time required to reach a residual of 0.0001. When the target normalised residual reached 0.0001 for all parameters, the solution was said to have converged and the solution was complete.

### 4.6 Boundary Conditions

Several boundary conditions were created within the model. The wheels, forks, fairings, false ground plane and tunnel sides, top and bottom were set as walls with surface roughnesses and roughness constants as shown in Table 4.2.

**Table 4.2** Surface roughness boundary conditions for CFD model

| Component | Surface Roughness (m) | Roughness constant |
|---|---|---|
| Wheel | $2x10^{-6}$ | 0.5 |
| 19mm tyre | 0.0001 | 0.5 |
| 22mm tyre | 0.0005 | 0.5 |
| Forks, fairings, axles | $2x10^{-6}$ | 0.5 |
| False ground plane | $2x10^{-6}$ | 0.5 |
| Wind tunnel walls | $8x10^{-6}$ | 0.5 |

The surface roughness of the coating over the carbon fibre used on the wheel and fork fairing was measured using a Talysurf surface roughness measurement machine. The wind tunnel wall roughness was estimated based upon inspection and comparison with the wheel surface. The two different tyres used, 19mm and 23mm had different levels of tread with the 23mm tread being visibly larger than that of the 19mm tyre. The tyre roughnesses were estimated by taking several tube diameter readings with a digital vernier scale and interpreting the variation in diameter readings as the height of the tread.

The effect of changing the roughness constant ($C_s$) was investigated. According to Fluent$^{TM}$ (2005), $C_s$ is dictated by the type of roughness. The default roughness constant ($C_s$ = 0.5) reproduced Nikuradse's resistance data for pipes roughened with tightly

packed, uniform sand grains when using the k-ε turbulence model. There is some experimental evidence that for non-uniform sand grains, ribs and wire-mesh roughness (i.e. less evenly distributed roughness or looser packing), a surface roughness constant of $C_s$ = 0.5-1.0 is appropriate. This implies that the more evenly distributed the surface roughness, the lower the surface roughness constant. The carbon fibre surfaces are likely to have a very even roughness distribution so the roughness constant for these surfaces most likely lies at the smooth end of the roughness constant scale, $C_s$ = 0.1-0.5. In reality, it is unlikely that a surface roughness is more evenly distributed than uniform sand grains but $C_s$ = 0.1 was tested anyway to ensure that it was not having an effect on the predicted force. When these roughness constants of $C_s$ = 0.1 and $C_s$ = 0.5 were employed on the 3-spoke CFD model, there was a negligible difference in measured force (0.03%) between each run.

The tread of the tyre is evenly distributed, but less tightly packed than the surface roughness of the carbon fibre surfaces. The roughness constant of the tyre most likely lies between $C_s$ = 0.5-1.0. Increasing the $C_s$ to 1.0 (from 0.5) resulted in a 0.9% increase in force, which is negligible. Therefore, the roughness constant was left at the default value of 0.5 for all surfaces.

The right hand end of the fluid domain was set as a velocity inlet with an incoming velocity of 13.89m/s (50km/hr) normal to the inlet plane. The left hand end of the fluid domain was set as a pressure outlet with a gauge pressure 0Pa. This resulted in all of the air entering at the velocity inlet flowing through the domain to the left hand end where it

exits the domain. The turbulence intensity of the wind tunnel flow was measured using hot-wire anemometers to be 0.4% at 30km/hr and 40km/hr and 0.5% at 50km/hr and these values were used in the inlet and outlet flow conditions. The hydraulic diameter of the velocity inlet was 1.03m based on the average of the width and height of the test section.

The wheel was set to rotate clockwise at 41.7 rad/s to match the incoming fluid velocity. This was achieved by making each of the wheel surfaces, which rotate during normal wheel operation, a moving wall rotating about the origin at the appropriate angular speed.

### 4.7 Turbulence Model

Several turbulence models were tested to determine which model was most appropriate for this application. A simple model of a rotating disk (to mimic a wheel but without hub geometry) was generated and solved using various turbulence models.

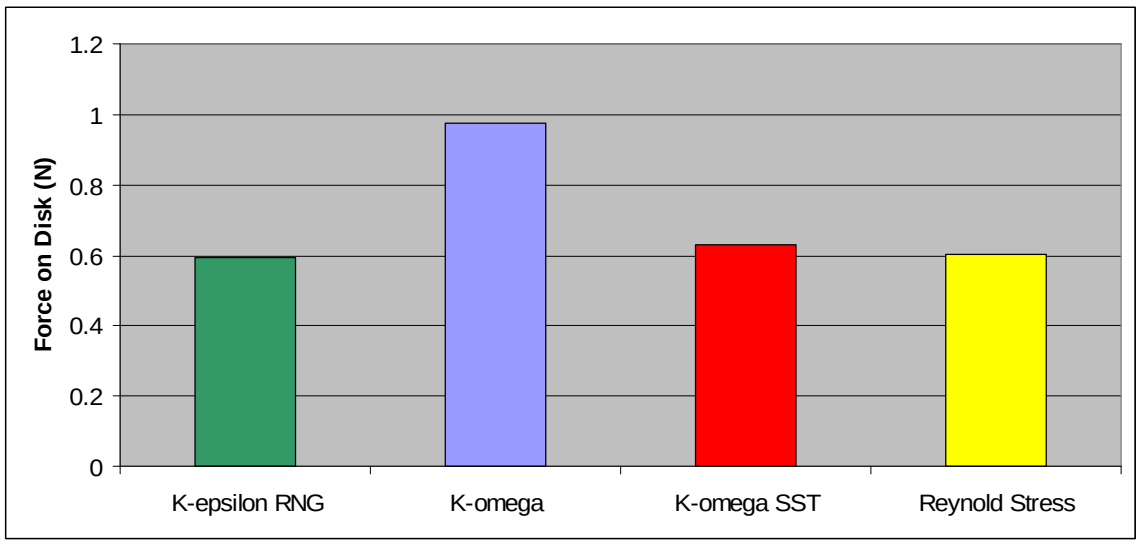


**Figure 4.3** – Force on disk with different turbulence models

Figure 4.3 shows that there is very little difference between the k-epsilon RNG, k-omega SST and Reynolds Stress models in terms of the force on the rotating disk. The k-omega standard model produced a significantly different result to the other three models so was discounted as an option. The Reynolds Stress model solves seven equations compared to the k-omega and k-epsilon models that each solve two equations so has a longer computation time. Therefore, it was decided to choose between the k-omega SST and k-epsilon RNG models.

The turbulence model chosen was the two equation k-ω shear stress transport (SST) model. The k-ω SST model is a blend of the k-ω and k-ε models and utilises a cross diffusion term which allows the k-ω model to be used near walls and the k-ε model in the outer flow. The k- ω SST model is known to more accurately predict flow separation compared to the k- ε models and as flow separation was visible in the experimental work it was deemed the most appropriate for this application.

The k-ω SST model works well in areas of large gradients but can sometimes be less accurate downstream. However, as we are only interested with the flow and forces on the wheel, the accuracy of the downstream flow this is not considered to be an important factor.

The k-ω SST model has the form:

$$\frac{\partial}{\partial t}(\rho k) + \frac{\partial}{\partial x_i}(\rho k u_i) = \frac{\partial}{\partial x_j}\left(\Gamma_k \frac{\partial k}{\partial x_j}\right) + \tilde{G}_k - Y_k + S_k \qquad (20)$$

$$\frac{\partial}{\partial t}(\rho\omega) + \frac{\partial}{\partial x_i}(\rho\omega u_i) = \frac{\partial}{\partial x_j}\left(\Gamma_\omega \frac{\partial \omega}{\partial x_j}\right) + G_\omega - Y_\omega + D_\omega + S_\omega \qquad (21)$$

In these equations, $\check{G}_k$ represents the generation of turbulence kinetic energy due to mean velocity gradients, $G_\omega$ represents the generation of ω. $\Gamma_k$ and $\Gamma\omega$ represent the effective diffusivity of *k* and ω, respectively. $Y_k$ and $Y\omega$ represent the dissipation of *k* and ω due to turbulence. $D_\omega$ represents the cross-diffusion term. $S_k$ and $S_\omega$ are user-defined source terms (Fluent, 2005).

The default constants for the k-ω SST model were used.

### 4.8 Discretisation Scheme

The CFD model employed a first-order, steady state discretisation scheme. While it was widely known that second-order discretisation schemes provide more accurate solutions, the good agreement between the CFD results (using first-order schemes) and the experimental results in terms of linear drag was considered sufficient and did not warrant a switch to the more computationally expensive second-order schemes.

### 4.9 2-D and 3-D Modelling

Both two-dimensional and three-dimensional models were employed in the analysis of the wheels. The 2-D models employed the same turbulence model, surface roughnesses and discretisation scheme as the 3-D models and the meshes were constructed with triangular elements, the two-dimensional equivalent of tetrahedral cells.

Chapter 5

# Finite Element Analysis

## 5.1 Introduction

Finite element analysis (FEA) is a method for numerical solution of field problems which require that the spatial distribution of one or more dependent variables is determined (Cook et al, 2002). In this project, the variation of stress and displacement of the bicycle wheels under loading is required to determine how geometric changes applied to the wheel to improve the aerodynamics change the structural performance. The FEA process is similar to the CFD process in that a model of the geometry is created, it is then divided up into many smaller elements and then numerical equations are solved at each of these elements to give the solution. The difference between FEA and CFD is that CFD solves the Navier Stokes equations which govern fluid flow and FEA solves structural stiffness matrices which govern how the body will behave when subjected to structural or thermal loads.

## 5.2 Modelling Software

The FE analysis was performed using ANSYS$^{TM}$ 11.0 academic research software. Pre-processing, processing and post-processing of the model were undertaken within ANSYS.

## 5.3 Pre-processing

The pre-processing stage of the FEA involved model geometry creation, choosing an element type, defining material properties and real constant information to the geometry to reflect its structure, meshing of the geometry into finite elements and applying boundary conditions to simulate a particular load scenario.

### *5.3.1 Model Geometry Creation*

The Zen disk and three-spoke wheel models were created by inputting keypoints to the model space, making lines between the keypoints and then making surfaces between the lines.

For the disk wheel, the keypoints and lines of the disk profile were created and then revolved around the central axis to create the entire wheel.

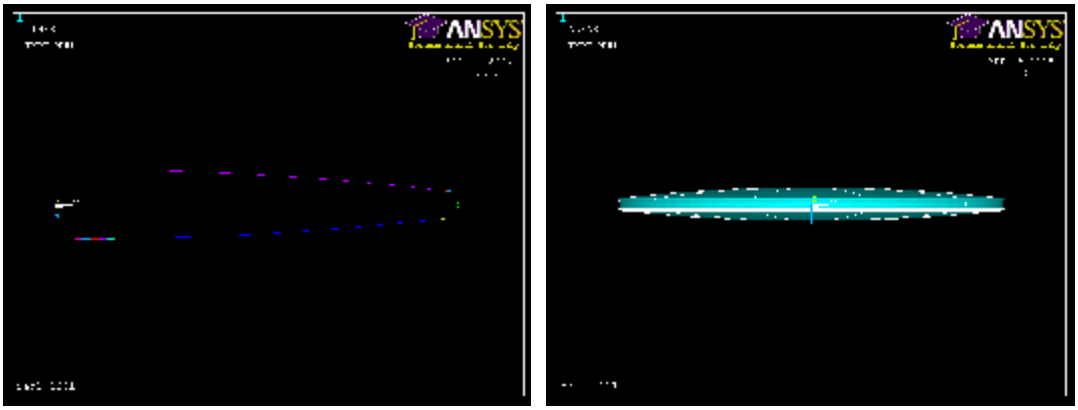


**Fig 5.1** Disk profile before (left) and after revolution about the central axis

The disk geometry also included a hub cap to simulate the gear side of a rear wheel. The structure of the disk wheel comprises two outer disks joined at the rim and the hub. Each outer disk is constructed of layers of carbon fibre over a honeycomb core.

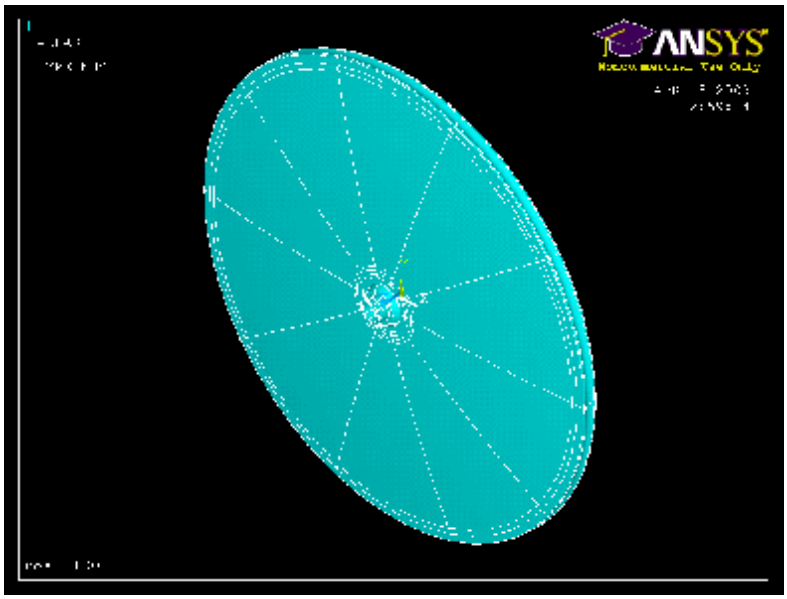


**Fig 5.2** Complete disk wheel geometry for analysis

The three-spoke wheel was created similarly to the disk wheel. Keypoints, lines and areas were created for one third of the wheel and this third was revolved around the central axis to create the whole wheel. Each of the three portions had to be 'glued' together as part of the analysis so that ANSYS$^{TM}$ recognised that they were connected.

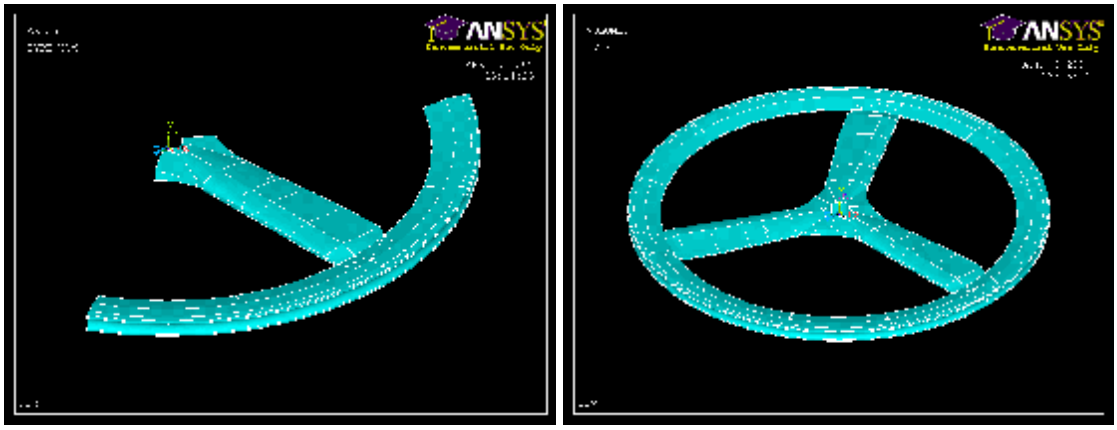

**Fig 5.3** 3-spoke geometry before (left) and after revolution about the central axis

Due to the complexity of the 3-spoke geometry and carbon-fibre construction, the hub and hub-caps were removed from the analysis. The 3-spoke structure comprises a honeycomb core with carbon fibre sheets layered over the outside to provide strength and stiffness.

*5.3.2 Choosing Element Type*

ANSYS™ provides several elements suitable for modelling the anisotropic nature of carbon-fibre composite materials. The most commonly used shell element types are SHELL 91 and SHELL 99. SHELL 99 was chosen for the analysis as SHELL 91 requires that the input layers are symmetrical about a central axis which is incorrect for the layers used in manufacturing the particular wheels in this analysis.

SHELL 99 creates linear layered structural shell 3D elements with 8-nodes each with six degrees of freedom. It is designed to model shell structures with side-to-thickness ratios of 10 or greater so it is appropriate for our thin walled wheels.

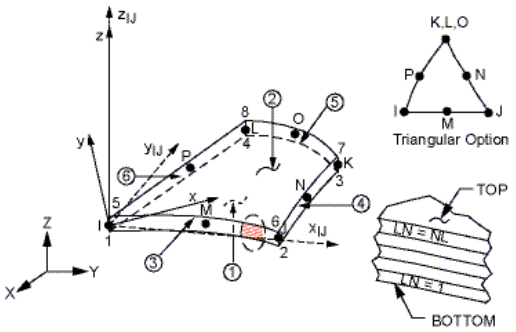


**Fig 5.4** SHELL 99 Element (ANSYS, 2007)

Both the disk and 3-spoke models also required solid elements to accurately represent the structure. In the disk wheel, the hub cap was modelled as a solid structure of carbon and aluminium and the interior of the 3-spoke wheel was modelled as a solid as in reality it is filled with a foam core. The solid element chosen was SOLID 92, which is a 3D, 10 node tetrahedral structural solid element. The tetrahedral shape and mid-element nodes allows easier meshing of complex geometries of which there are several in the wheel models.

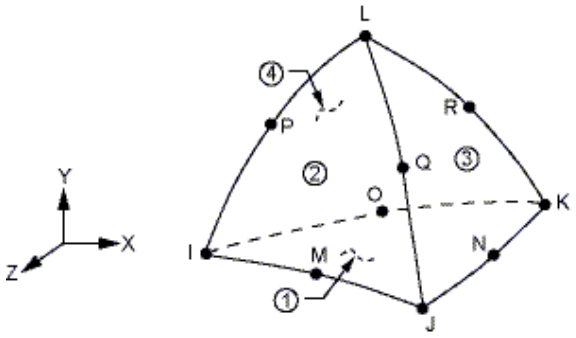


**Fig 5.5** Solid 92 element (ANSYS, 2007)

*5.3.3 Defining Materials*

In order for ANSYS$^{TM}$ to accurately model the problem, the properties for each material have to be entered. For elements described in section 5.3.2, the only material properties required are the Young's modulus (E), Poisson's ratio ($\nu$) and shear modulus (G) in each direction. The material properties used are listed in Table 5.1.

**Table 5.1** Material properties

| MATERIAL | $E_x$ (GPa) | $E_y$ (GPa) | $E_z$ (GPa) | $\nu_x$ | $\nu_y$ | $\nu_z$ | $G_x$ (MPa) | $G_y$ (MPa) | $G_z$ (MPa) |
|---|---|---|---|---|---|---|---|---|---|
| **Carbon Fibre (Unidirectional)** | 246.1 | 8.7 | 3.1 | 0.25 | 0.25 | 0.25 | 2.9 | 2.9 | 2.9 |
| **Carbon cloth** | 66.4 | 66.4 | 3.1 | 0.30 | 0.30 | 0.30 | 25.5 | 25.5 | 25.5 |
| **Honeycomb** | 44.5 | 4.4 | 79.5 | 0.26 | 0.22 | 0.02 | 0.5 | 14.6 | 8.6 |
| **Al 6061** | 68.9 | 68.9 | 68.9 | 0.33 | 0.33 | 0.33 | 26.0 | 26.0 | 26.0 |

### *5.3.4 Defining Real Constants*

The real constant set for each element defines the element's geometric properties. For the SHELL 99 elements, the real constant set contain the information of what layers of material are present, the layer order and the thickness of the layers. As the composition of materials varies between different parts of the wheel, the real constants defined at different areas must also be different. The wheel geometries were made with surface areas corresponding to the different areas of material composition.

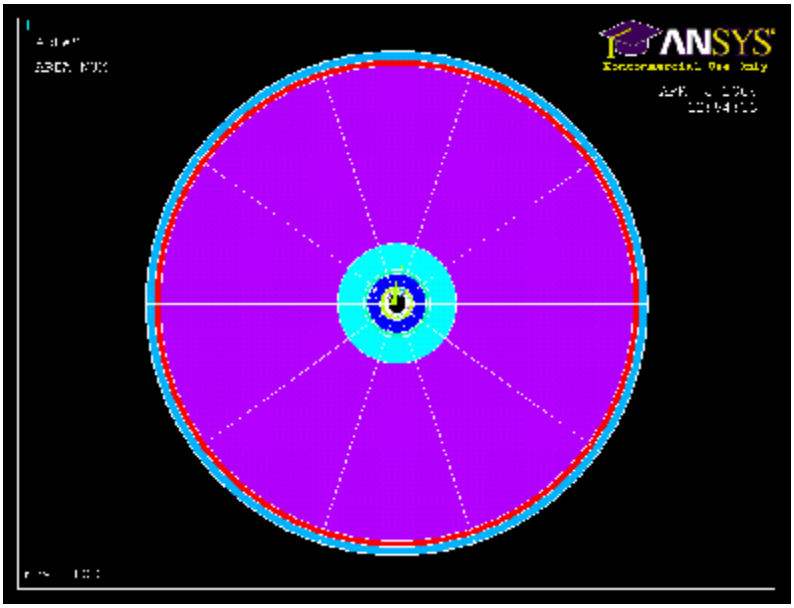


**Fig 5.6** Real constant areas for disk wheel

For example, figure 5.6 shows areas of the disk wheel and the different colours indicate that a different real constant set should be applied. This is because the material composition of the sides of the wheel is different to areas nearer the rim and at the hub.

The 3-spoke material composition was far more complex than that of the disk wheel and required a greater number of real constants to be defined. Figure 5.7 indicates the areas created in the 3-spoke model which required real constant definition and figure 5.8 shows how the real constants were allocated among the areas.

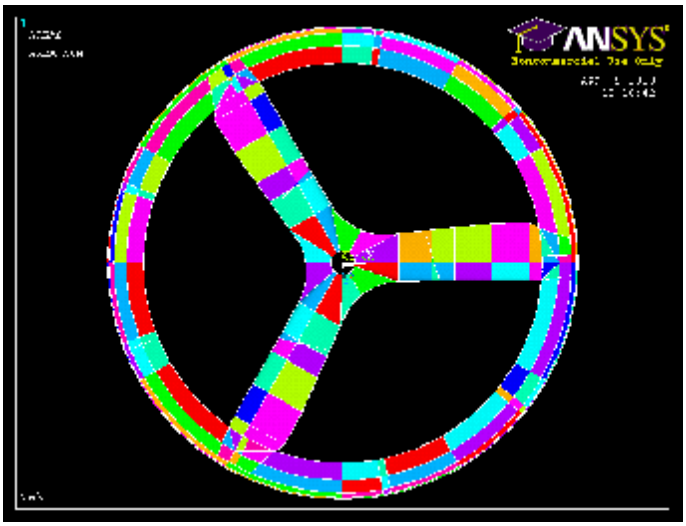


**Fig 5.7** Areas of 3-spoke model

**(a)** Rim

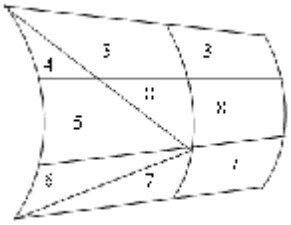

**(b)** Spoke head

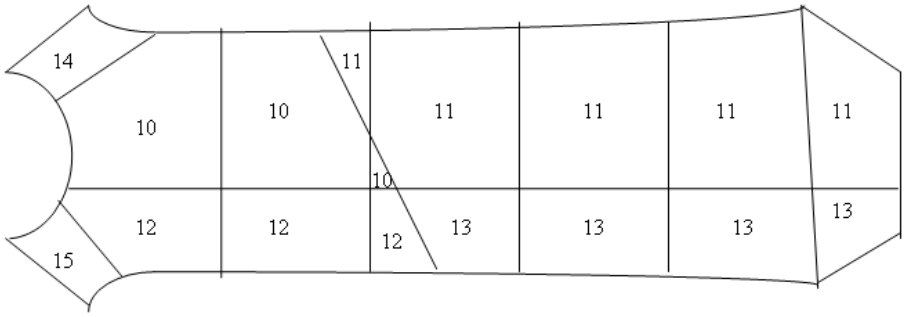


**(c)** Spoke

**Fig 5.8** Real constant allocation for areas of 3-spoke model

*5.3.5 Boundary Conditions*

The boundary conditions of the analysis were set to match the method used to test the stiffness of the wheels. The wheels were laid upon a rig with contact points on the rim on opposite sides of the wheel. Masses totalling 30kg were placed at the centre of the wheel and the resulting deflection at the centre of the wheel was measured with the dial gauge to be 2.2mm for the disk wheel.

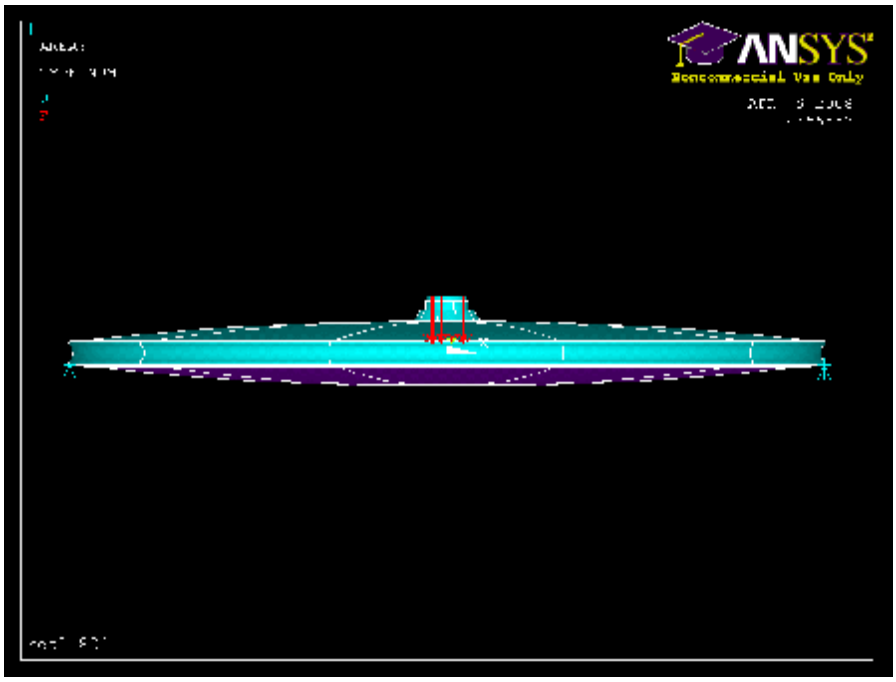


**Fig 5.9** Side of restraints (blue arrows at rim) and 30kg load application area (red arrows)

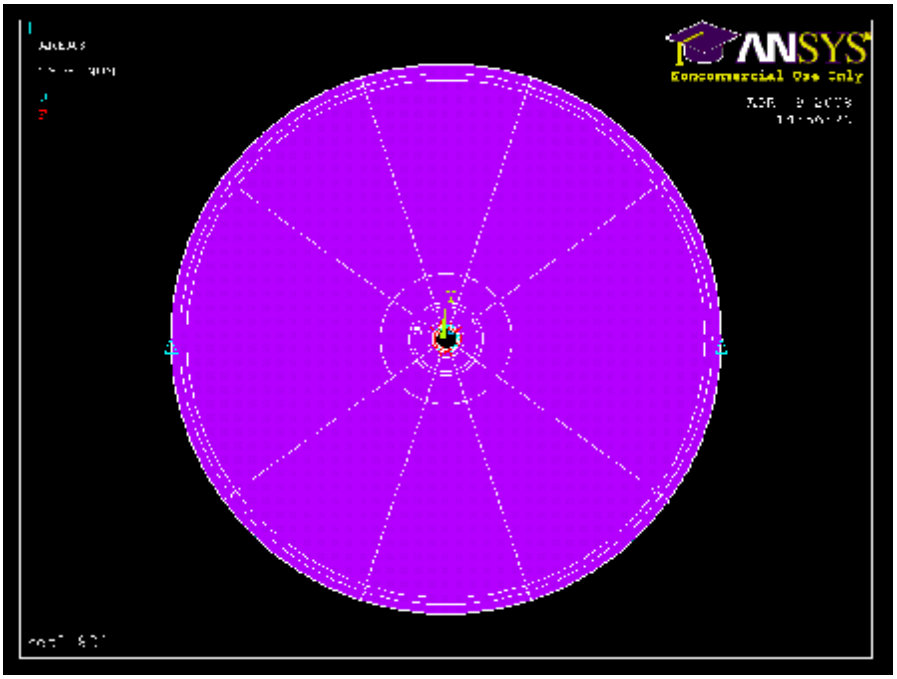


**Fig 5.10** Top view of restraints (blue arrows) and 30kg load application area (red dots)

Figures 5.9 and 5.10 show the restraints in the vertical and horizontal direction at which the rim displacement, under the applied loading was set to zero. Also visible in figs. 5.9 and 5.10 is the load application area where the 30kg was placed to cause the wheel to deflect. In ANSYS™, the load was input as a downward force of 14.715N at twenty different key points around the hub equating to 294.3N total (30kg).

*5.3.6 Meshing*

The meshing process involved selecting areas and then choosing the appropriate real constant, element type and coordinate system. The most efficient way to do this is to mesh one real constant at a time, selecting all required areas until all real constants are meshed. The smart sizing function within the software was utilised. This involved specifying a level of mesh definition (1 = fine, 10 = coarse). As with CFD, the finer the

mesh, the more elements are being solved and the longer the computation time. The coarseness of the mesh was limited due to the complex area geometry required to describe the different structural layers. For the disk wheel, the coarsest possible mesh occurred with a 'smart size' of 7 and contained 88,264 nodes. The fineness of the mesh was limited by the power of the computer processor. The finest mesh occurred with a 'smart size' of 4 and contained 109,757 nodes.

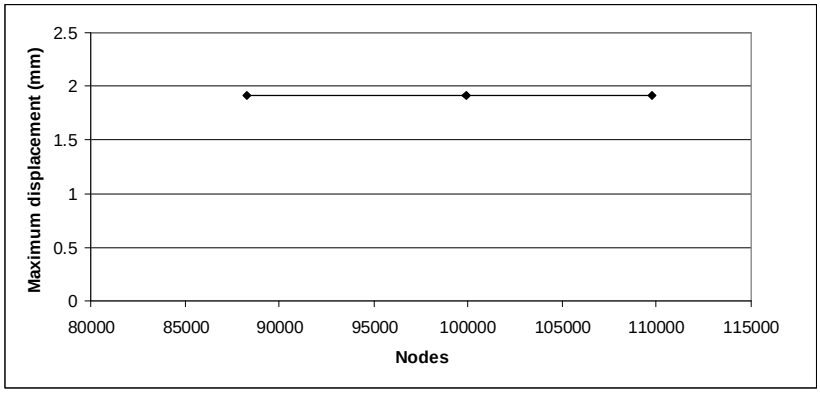


**Fig 5.11** Mesh convergence tests of maximum displacement

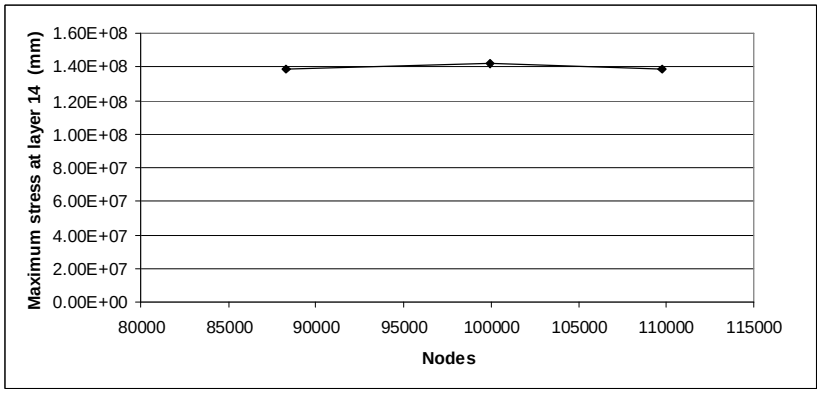


**Fig 5.12** Mesh convergence of maximum stress

The parameters chosen for the mesh convergence testing were the maximum displacement of the centre of the disk wheel and the maximum stress in the disk wheel.

Figure 5.11 shows that the predicted maximum displacement of the centre of the wheel does not change as the number of nodes increases. The predicted figure also compares well with the experimental result of 2.2mm deflection with a 30kg load. Figure 5.12 indicates that the maximum stress is identical at both 88,264 nodes and 109,757 nodes. There is a 2.1% variation in the maximum displacement between 99912 nodes and 109757 nodes which is an acceptable variation.

Therefore, it was decided that either the 88,262 nodes or 109,757 nodes model would provide sufficiently accurate results.

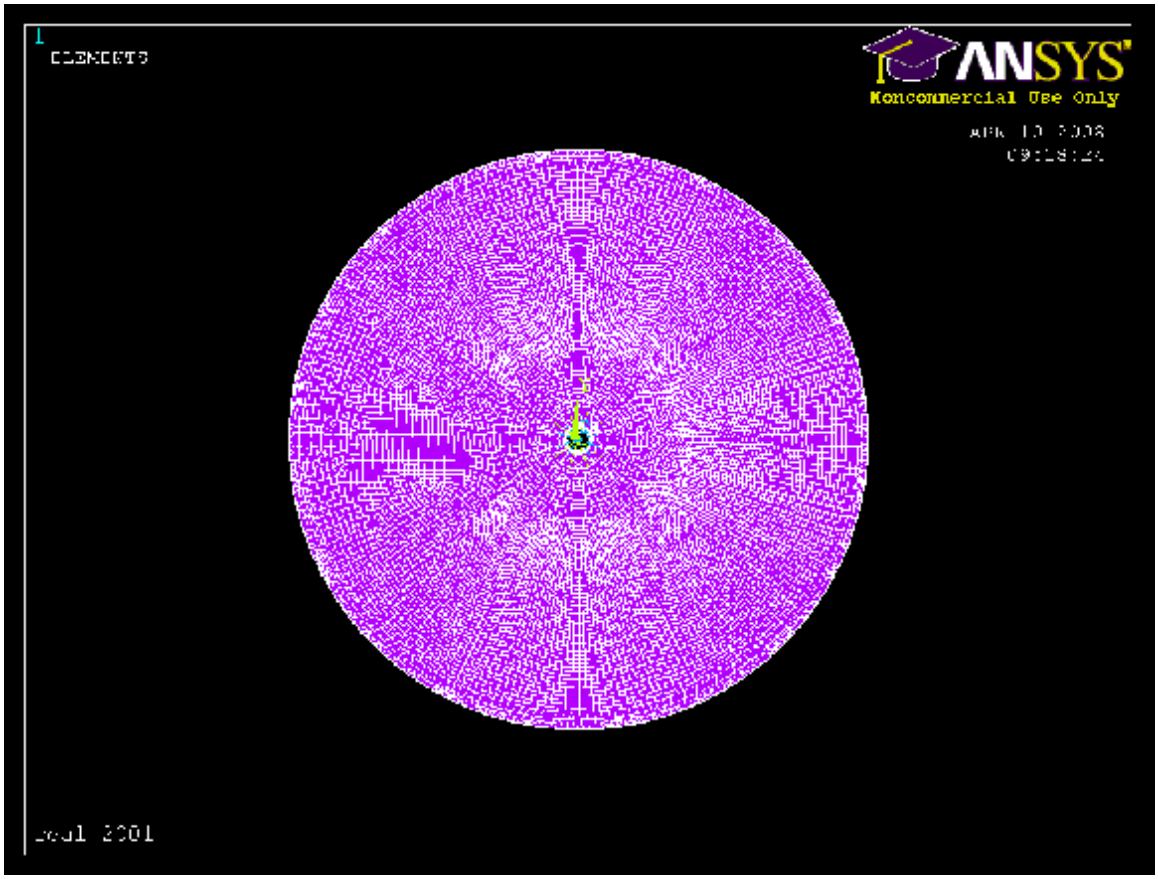


**Fig 5.13** ANSYS mesh with 88,262 nodes (smart sizing level 7)

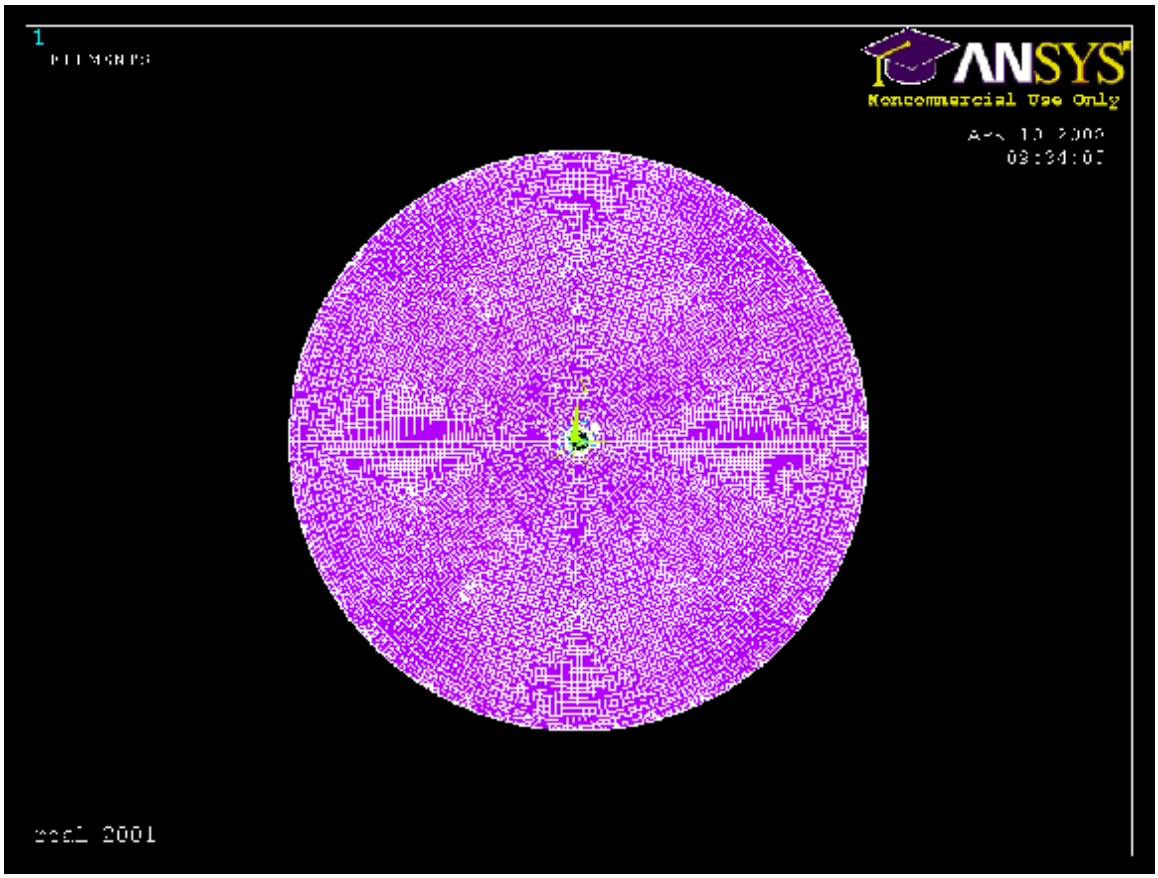


**Fig 5.14** ANSYS mesh with 109,757 nodes (smart sizing level 4)

Upon examining the two mesh options, it was seen that the mesh created with 109,757 nodes (Fig 5.14) appeared much smoother and more evenly distributed than the mesh with 88,262 nodes (Fig 5.13). Therefore, it was decided to use the mesh with 109,757 nodes for subsequent calculations as the computational time penalty was negligible but the mesh was improved.

An identical process of determining mesh convergence was undertaken for the 3-spoke wheel. Convergence for both deflection and maximum von-Mises stress was achieved with a mesh containing 177,178 nodes.

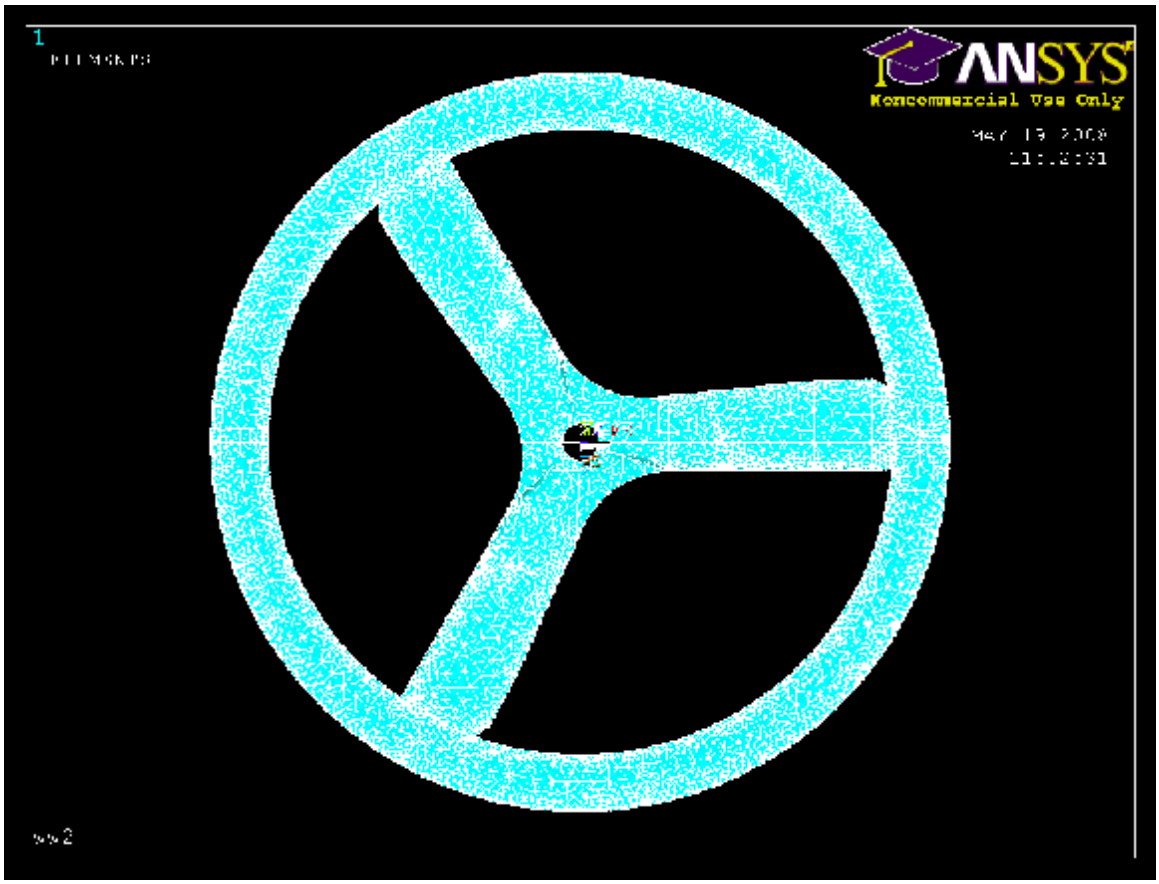


**Fig 5.15** Finite elements for 3-spoke wheel

Figure 5.15 shows the finite elements used to solve the 3-spoke wheel loading problem. Regions of high element concentration are visible on the spoke due to small surface areas in those positions. A more evenly distributed mesh of ~700,000 nodes was tested but the deflection and stress predictions did not change. Therefore, due to the significantly shorter computation time, the 177,178 node mesh was used.

### 5.4 Solution Generation and Post-processing

Model solution generation and post-processing was also performed in ANSYS™. The default solution control settings were used.

Chapter 6

# Current Disk Wheel

## 6.1 Introduction

Disk wheels are characterised by one continuous skin from hub to tyre over the usual spoke area of a wheel. They are currently the preferred option for track cycling and as a rear wheel for outdoor time trials as they are perceived by many riders to be the most aerodynamic wheels available. However, their large side areas can leave them susceptible to large cross wind forces and their weight can have an effect on the acceleration of the bicycle and rider system

This chapter will discuss the experimental testing of three differently shaped disk wheels and the computational fluid dynamics and finite element analyses performed on the Zen disk wheel.

## 6.2 Experimental Testing

Three rear disk wheels were tested in the wind tunnel: the Corima flat disk, the Zen convex disk and the Mavic convex disk. The Mavic convex disk is especially popular among elite riders around the world.


Zen Disk Mavic Disk Corima Disk

**Figure 6.1** – Photos of disk wheels tested

**Table 6.1** Characteristics of disk wheels tested

| Wheel | Mass (g) | Width at hub (mm) | Width at rim (mm) | Profile |
|---|---|---|---|---|
| Corima disc | 1082 | 20 | 20 | Flat |
| Zen disc | 1070 | 53 | 20 | Convex |
| Mavic disc | 1112 | 60 | 20 | Convex |

All wheels were tested with the same 19mm tyre, inflated to 100psi.

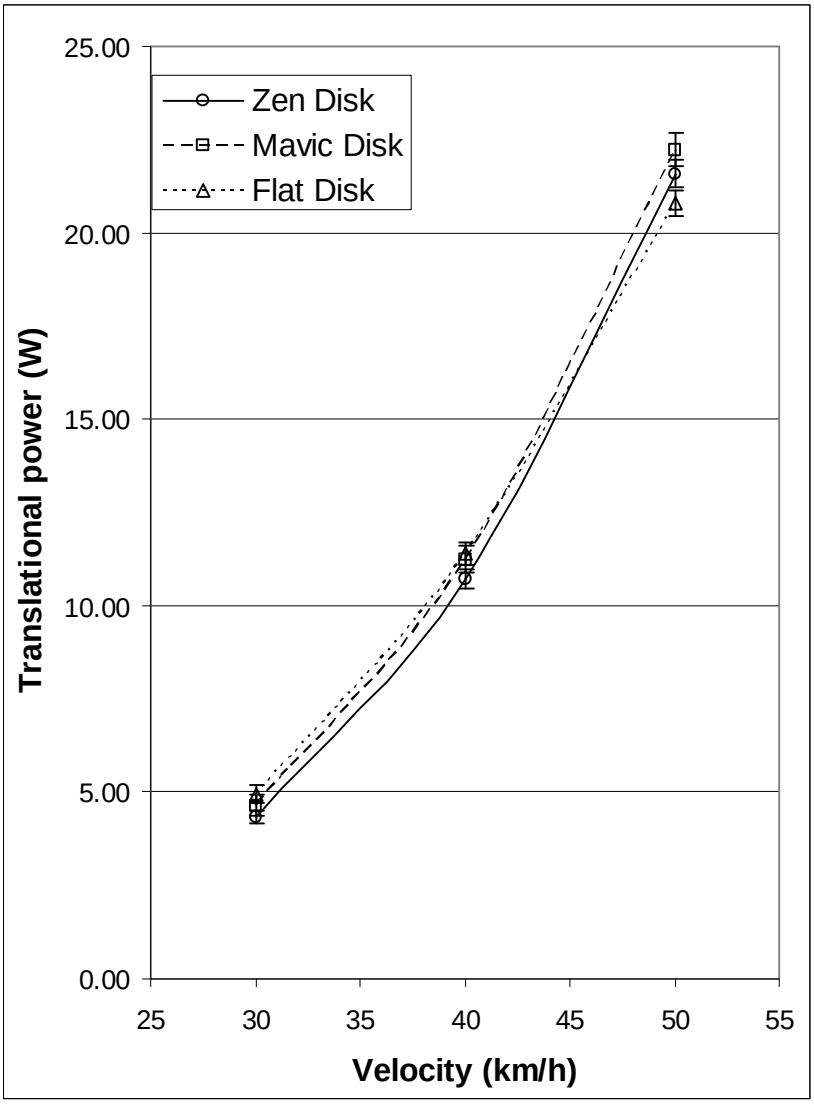


**Fig 6.2** Translational power of disk wheels

Figure 6.2 shows the power required to translate the disk wheels in a forward direction. The wheels differ in power requirement by up to 12%. The differences in power are very small despite the great differences in hub width between the flat and convex disks (20mm to 60mm). The flat wheel requires the most power to translate forward until the velocity rises to 50km/hr where it requires the least power. At speeds up to and including 40km/hr, the Zen disk requires the least power. Below 50km/hr the differences in power

requirements between all of the wheels is less than the uncertainty (Moore et al, 2008). At 50km/hr, the difference in power between the flat wheel and the convex wheels is greater than the uncertainty while the difference between the convex wheels is less than the uncertainty. An example of an uncertainty calculation is provided in Appendix A.

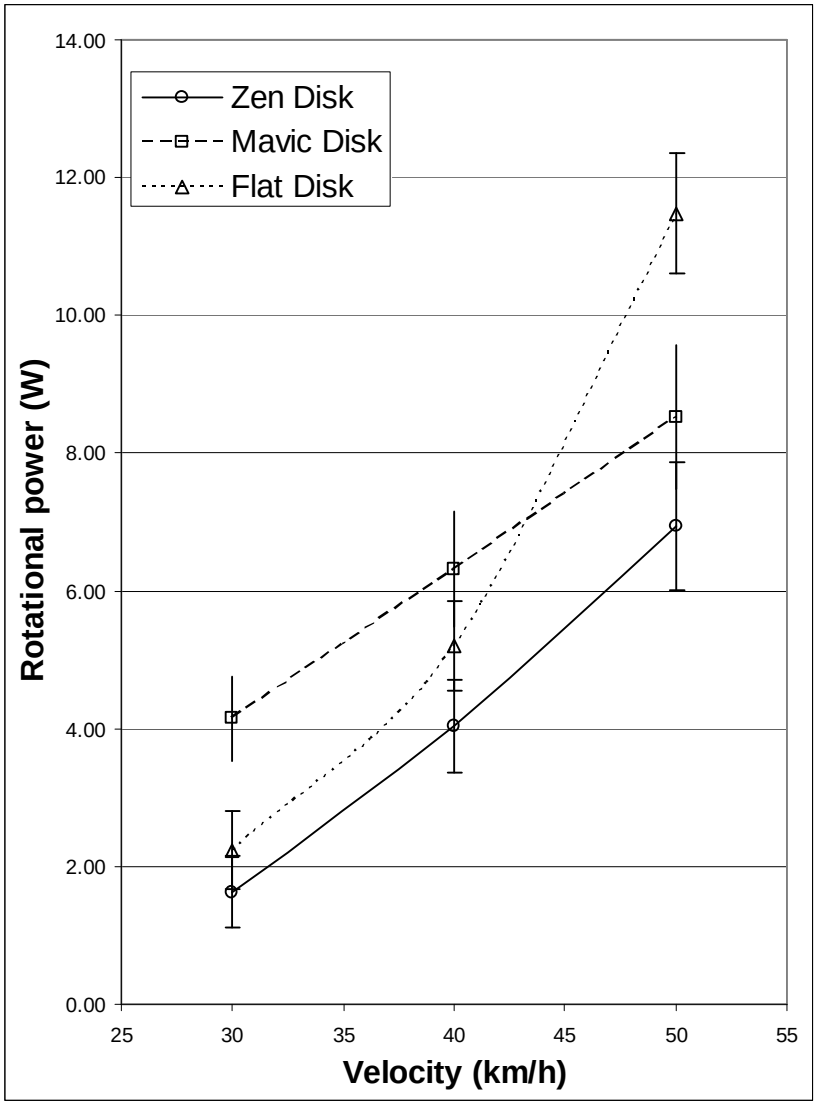


**Fig 6.3** Rotational power of disk wheels

Figure 6.3 plots the power required to rotate the wheels. With differences between the wheels up to 40% it is this component of power than sets the wheels apart. As the

velocity increases, the flat disk shows a much larger increase in required rotational power than the other two wheels (Moore et al, 2008). The rotational power of the Zen convex wheel is consistently lower than that of the Mavic convex disk. The rotational power of the Zen and Mavic convex disks increases proportionally with velocity while the flat disk rotational power appears to have a squared relationship with velocity.

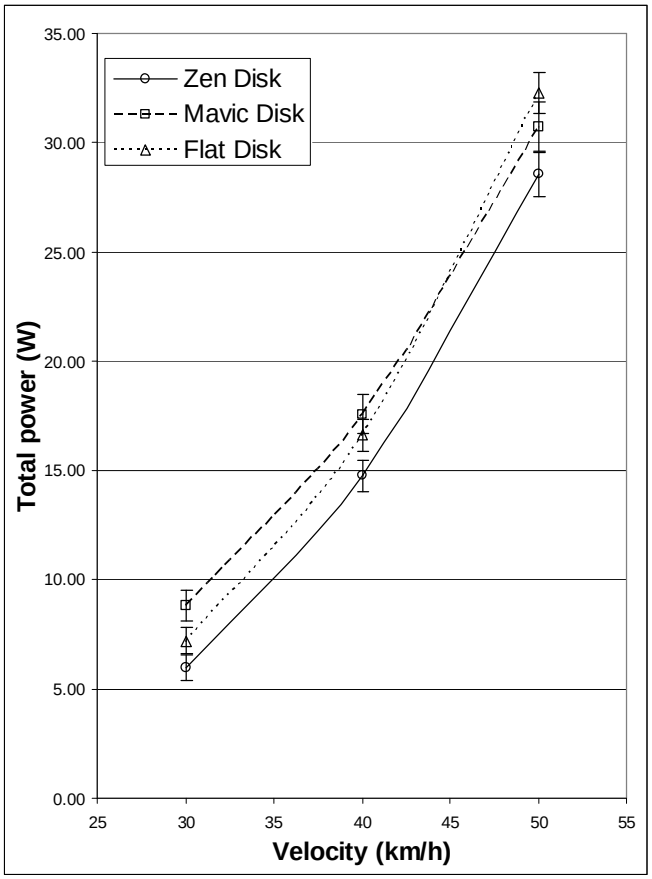


**Fig 6.4** Total power of disk wheels

Figure 6.4 shows the sum of translational and rotational power. The disk wheels require significantly more power to translate than they do to rotate. The trend in total power matches that of translational power except at 50km/hr where the rotational power of the flat disk gives it the greatest total power. At all speeds tested, the Zen disk requires the

least power. The differences between the wheels are greater than the uncertainty. With the surface area of the convex disks being greater than the flat disk, it was expected that the rotational power for the convex disks would be higher than for the flat disk. The experimental results, however, show no clear trend between surface area and rotational profile (Moore et al, 2008).

The final experimental test performed on the existing Zen disk wheel was to measure the power requirements when it is fitted with a larger tyre. Different tyres are used for different riding conditions and there is currently debate among some international athletes as to which tyre is better for velodrome riding. The Zen disk wheel was tested with a 22mm tyre to compare with the results from previous tests which used a 19mm tube.

**Table 6.2** Experimental results with differing tyre diameters

| | Linear Power (W) | Rotational Power (W) | Total Power (W) |
|---|---|---|---|
| 19mm tyre | 21.58 | 6.95 | 28.53 |
| 22mm tyre | 27.33 | 8.85 | 36.18 |

The experimental results in Table 6.2 indicate a 27% increase in both linear and rotational power when the tyre size is increased from 19mm to 22mm. Combined with the increased rolling resistance of a larger tyre due its larger area in contact with the ground, there appears to be no reason why a larger tyre should be used instead of a smaller tyre for indoor velodrome riding if the cyclist is already comfortable using the smaller tyre. For outdoor riding, a larger tyre is often used as it provides a more comfortable ride on the road surface, which is generally much rougher than a velodrome

track. In this case, the aerodynamic penalty is offset by the increase in comfort, especially for long races.

### 6.3 CFD Analysis

A computational fluid dynamics study of the Zen rear disk wheel was performed as described in Chapter 4. The forces on the wheel and axles were extracted from the data to compare them with the experimental forces. The CFD results are presented and compared with the experimental findings in Table 6.3.

**Table 6.3** CFD Analysis and experimental power results at 50km/hr

| | Linear Power (W) | Rotational Power (W) | Total Power (W) |
|---|---|---|---|
| CFD | 19.97 | 5.16 | 25.13 |
| Experimental | 21.58 | 6.95 | 28.53 |

The linear power predicted by CFD is within 7.5% of the experimental data, which is considered a good agreement. The rotational power, however, does not compare as well with a 26% discrepancy between the results. This leads to the CFD total power result being within 17% of the experimental data. When the experimental uncertainty is taken into account, and the CFD result is compared to the lower limit of the experimental data (21.22W), the difference between results is reduced to 5.9%. This indicates that while the CFD model is not simulating the flow entirely accurately, overall it has a reasonable agreement with the experimental results and the model can be used for further analysis of the wheels.

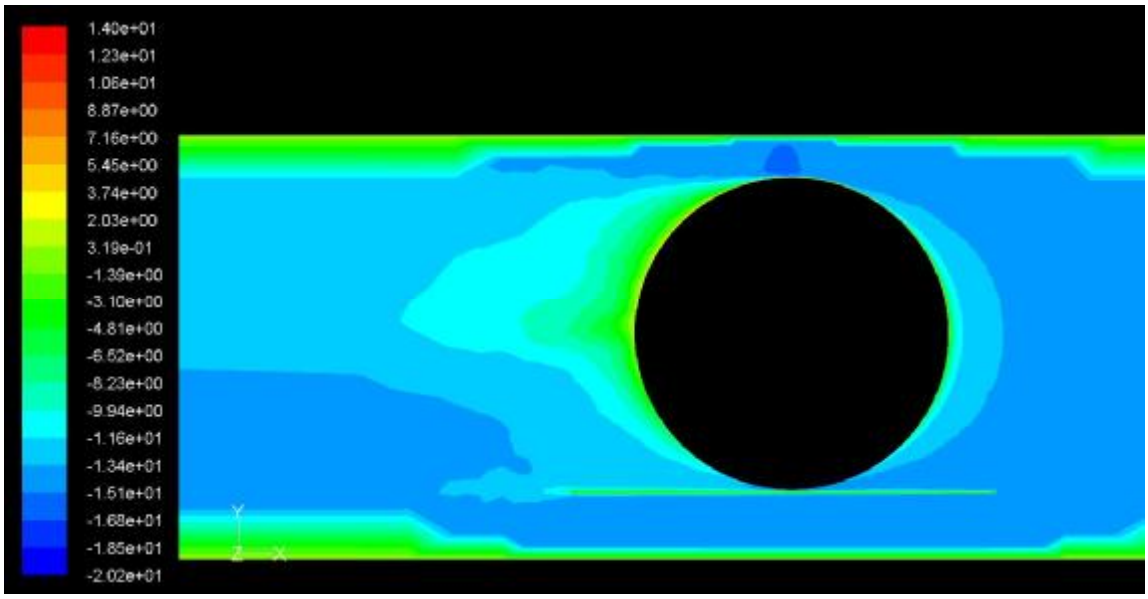


**Fig 6.5** Flow velocity in the x-direction around the Zen disk wheel at 50km/hr

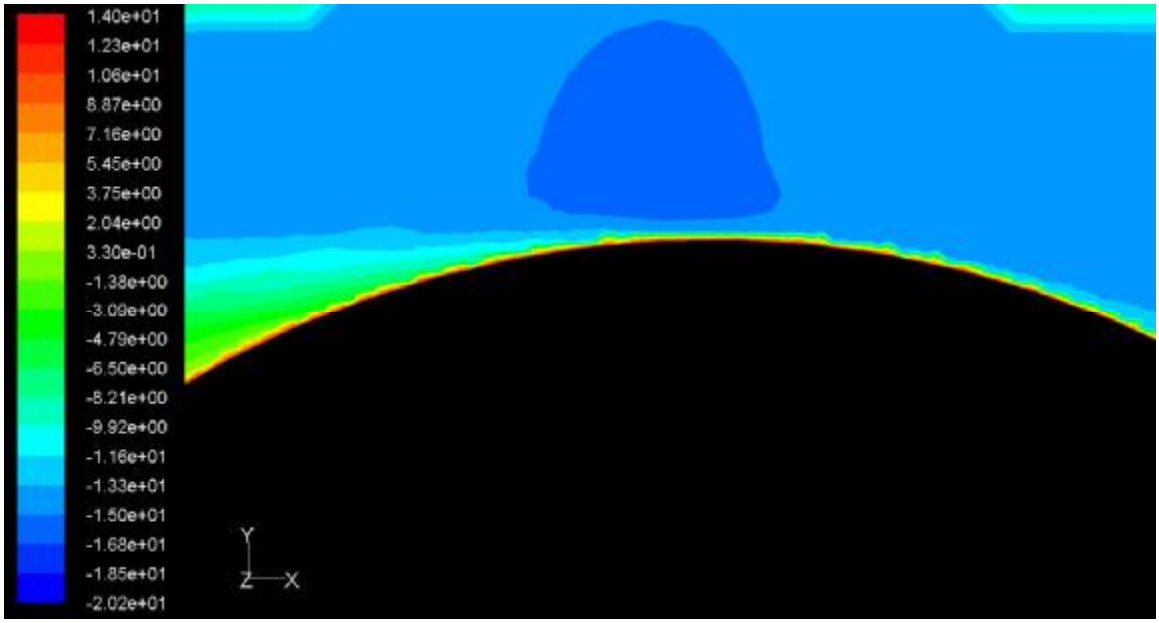


**Fig 6.6** Flow velocity at top of Zen disk wheel at 50km/hr

Fig 6.5 shows the velocity in the x-direction when the wheel is rotating and subjected to an airflow of 50km/hr. The wake develops behind the upper half of the wheel where the forks are having an influence on the flow. The flow across the bottom half of the wheel is

much less disturbed and the resulting wake is smaller. The rotation of the wheel also has the effect of pulling the flow in a clockwise direction. This is seen in Fig 6.6 where a boundary layer with a high velocity in the opposite direction to the bulk flow is visible at the top of the tyre. This indicates the importance of choosing the right tyre for the conditions – racing with a tyre with more tread (higher surface roughness) than is actually required to maintain control on the riding surface has an aerodynamic penalty in addition to the additional rolling resistance where the wheel is in contact with the ground. Fig 6.5 also illustrates the difference in boundary layer development between the wind tunnel floor and the false ground plane, confirming the reasoning for including the false ground plane in the experimental setup (refer section 3.3).

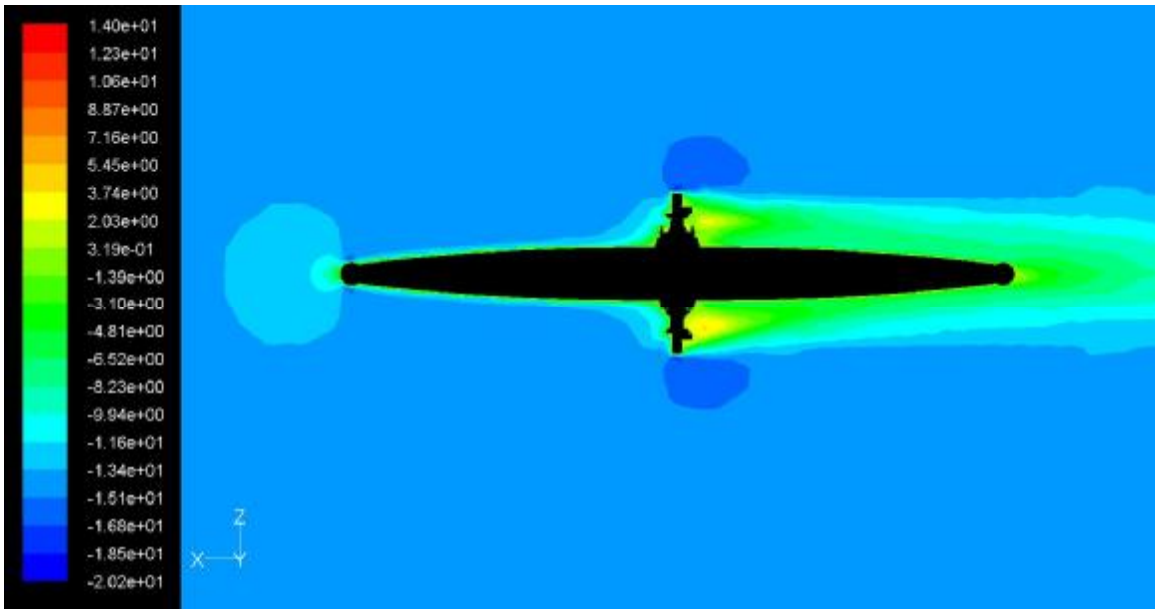


**Fig 6.7** Flow velocity in the x-direction around the Zen disk wheel at 50km/hr (top view)

Figure 6.7 shows the velocity in the x-direction around the wheel at a plane through the centre of the wheel. The flow stagnates at the front of the wheel. The flow follows the curvature of the wheel closely until it reaches the hub after which the wake develops. The

width of wake appears dominated by the width of the hub and axle. Some of the separated flow reattaches to the wheel surface toward the back of the wheel. An area of flow recirculation is visible behind the hub on each side of the wheel. This is indicated by the yellow, positive velocity contour region in figure 6.7 and is further illustrated using x-velocity vectors in fig 6.8. A single recirculating eddy is located behind the drive hub while two eddies are located behind the non-drive hub.

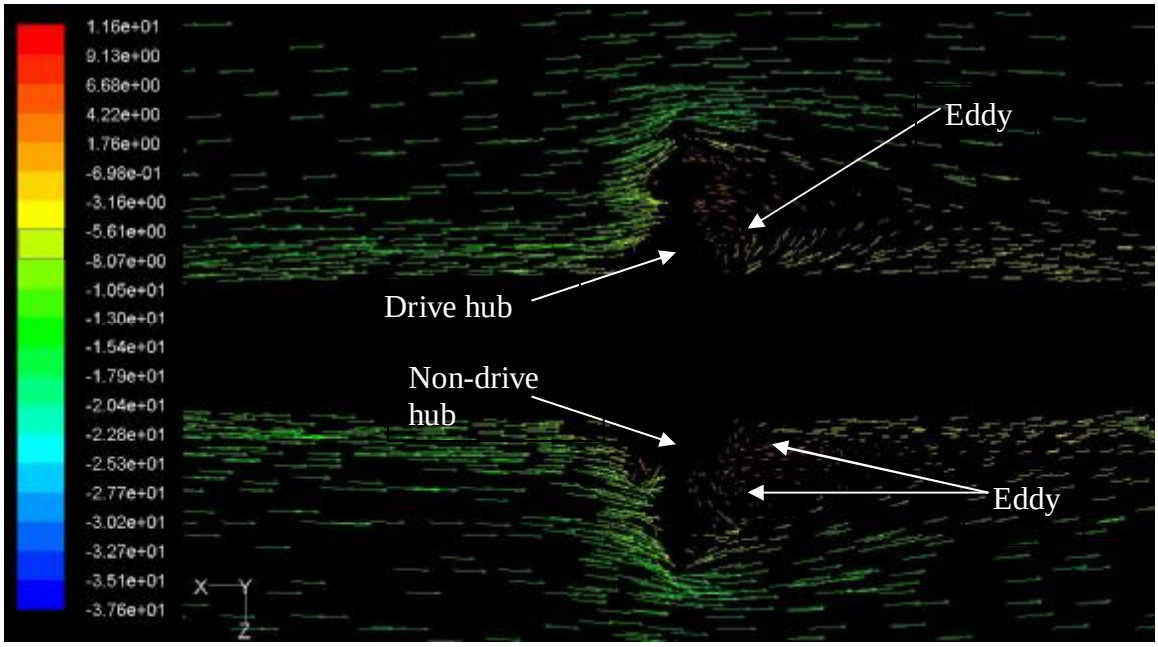


**Fig 6.8** Velocity vectors behind Zen disk wheel hub at 50km/hr

It should be noted, however, that the number and location of small eddies in CFD is very sensitive to convergence and mesh size. The number of eddies seen here may not be significant.

### 6.4 Finite Element Analysis

As described in chapter 5, a model of the disk wheel was constructed within the software ANSYS$^{TM}$ 11.0 and analysed using finite element methods. The focus of the analysis was on the strength and stiffness of the wheel structure when subjected to 30 kg load at the hub.


**Fig 6.9** Experimental deflection test

An experiment was performed to validate the results of the finite element analysis. The experiment consisted of mounting the disk wheel on each side of the wheel and placing a 30kg load at the hub (fig 6.9). The deflection of the centre of the wheel when the 30kg load was applied was measured with a dial gauge to be 2.2mm +/- 2%. The dial gauge had an accuracy of +/- 0.01mm and the 30kg mass had and accuracy of +/- 0.1kg.

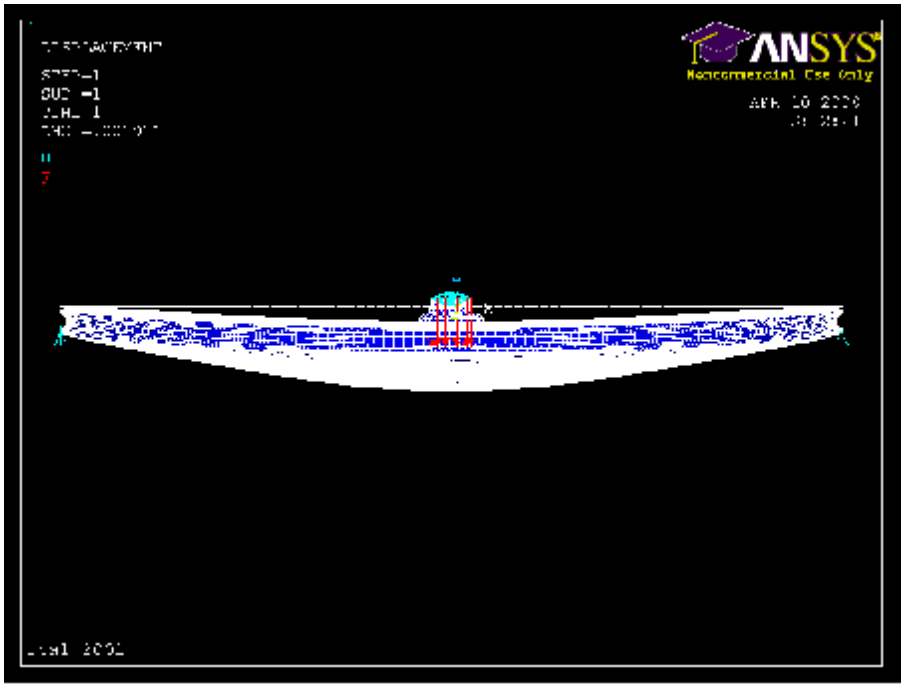


**Fig 6.10** Wheel deflection under a 30kg load (boundary conditions shown)

The FE analysis predicted the deflection to be 1.911mm (DMX in fig 6.10) which is within 13.1% of the experimental results. Therefore, the FE analysis is providing sufficiently accurate results so the model can be used to examine any implications on strength and stiffness due to changes to the wheel geometry based upon aerodynamic findings.

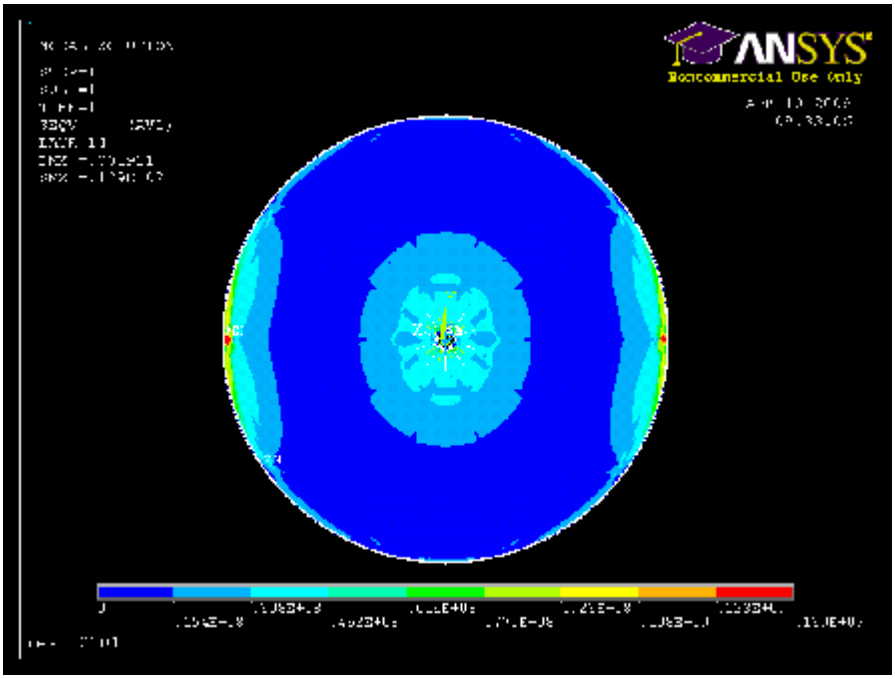


**Fig 6.11** Von Mises stress in layer 14 (unidirectional carbon fibre layer) with 30kg load

The maximum von-Mises stress in the wheel under this bending condition occurred in layer 14 which is a layer of unidirectional carbon fibre mat. The maximum stress of 139MPa is tensile as the layer is being elongated due to the bending. The M40JB fibres within the mat have a tensile strength of 4400MPa (Torayca, 2005) so the safety factor under this loading is 31.7 which is more than adequate. The areas of maximum stress are located at the boundary condition points – the wheel support points and the load application points. The stiffness of the wheels means that the highest stresses are contained within these areas and do not spread further into the wheel structure.

## 6.5 Optimisation of Disk Width

The experimental testing found that disk wheels of differing hub widths have different aerodynamic properties. A curve fitted through the total power requirements of the disk wheels at 50km/hr indicated that there is a potential minimum power requirement achievable with a disk between 20-53mm wide. An extensive CFD and FEA analysis of disk wheels with hub width between 20-53mm was performed but can only be broadly described in this thesis due to the results being commercially sensitive.

A CFD analysis was conducted by testing hub widths increasing in 5mm increments. CFD predicted a point of minimum total power requirement in the same hub width range as the experimental results suggested. The CFD analysis narrowed the optimum hub width range to ±5mm of a particular hub width.

A FE analysis of the disks wheels with different hub widths was also undertaken. The analysis looked at the changes to the wheel structural stiffness due to changing the hub width. Different materials to those currently in the wheel were tested in the finite element model and the deflection of these wheels was compared to the original deflection. The final result of the FE analysis was that a new material configuration, which achieved wheel deflection within ±10% of the current wheel deflection, was determined.

## 6.6 Conclusion

The experimental testing of the existing disk wheel has demonstrated the difference in aerodynamic properties between disk wheel of different widths. The choice of which sort

of wheel to ride in a race is often determined by rider ‘feel’ or common perceptions about aerodynamic performance of a type of wheel. Subjective comparisons are difficult. Therefore, having reliable experimental data concerning the aerodynamic properties of different disk wheels is an important first step in optimising the disk wheel design. The CFD and FEA models described in this chapter, having been validated by the experimental results, were further used to optimise the width of the convex disk wheel. Due to the commercially sensitive nature of the results of the optimisation process, they cannot be commented on further within this thesis.

Chapter 7

# Current Spoked Wheel

## 7.1 Introduction

Spoked wheels are the most common bicycle wheels available. Wheels with 16-32 wire spokes in tension between the rim and the hub are commonly found on both road and mountain bikes. Increasingly common are spoked wheels with fewer spokes, generally 3-5 spokes, with the spokes being in compression similar to traditional wooden or steel wheel. These 3-5 spoke wheels are manufactured from carbon fibre to utilise the high strength/weight ratio of this material. They are often used as the front wheel in competitive time trial events as their reduced side projected area makes them less susceptible to cross winds. It is perceived by some riders, however, that the reduced side force experienced by a spoked wheel is overshadowed by the increase in turbulence and flow separation due to rotating spokes compared to a disk wheel.

This chapter will discuss the experimental testing of different spoked wheels which are commonly used in cycling events and the computational fluid dynamics and finite element analyses performed on the Zen 3-spoke wheel.

### 7.2 Experimental Testing

Five front spoked wheels were tested in the wind tunnel: the Zen 3-Spoke, the Mavic 5-Spoke, the Zipp 808, Zen wire-spoke and the HED 3-Spoke. The Zen 3-Spoke, Mavic 5-Spoke and HED 3-Spoke are manufactured from carbon fibre and their spokes are in compression. The Zipp 808 and Zen wire-spoke wheels have carbon fibre rims and wire spokes and the spokes are in tension.

Zen 3-Spoke

Mavic 5-Spoke

Zipp 808

Zen Wire Spoke


HED 3-Spoke

**Fig 7.1** – Photos of spoked wheels tested

**Table 7.1** Characteristics of spoked wheels tested

| Wheel | Mass, (g) | Width at widest point of rim (mm) | Depth of rim (mm) (from outermost carbon fibre to inner edge of rim) | Side projected area ($m^2$) | Type of spoke | No. of spokes |
|---|---|---|---|---|---|---|
| Zen 3-spoke | 840 | 19 | 50 | 0.19 | Composite, compression | 3 |
| Mavic 5-spoke | 890 | 19 | 55 | 0.23 | Composite, compression | 5 |
| Zipp 808 | 694 | 26 | 80 | 0.19 | Wire, tension | 18 |
| Zen wire spoked | 511 | 19 | 40 | 0.13 | Wire, tension | 16 |
| HED 3-spoke | 724 | 19 | 53 | 0.20 | Composite, compression | 3 |

Two Zen 3-spoke wheels were tested – one in good condition and one with crash damage. The crash damage comprised a deep score in the rim near the tyre and the stickers on the wheel were creased. All wheels were tested with the same 19mm tyre inflated to 100psi.

Note the difference in spoke profiles between the Zen 3-spoke, Mavic 5-spoke and HED 3-spoke. The spokes on the Zen wheel are widest at the rim and taper in toward the hub while the Mavic and HED wheels have a much more constant chord length along the entire spoke.

### *7.2.1 Translational and Rotational Drag Measurements at 0° Yaw Angle*

The first experiments undertaken tested the spoked wheels at 0° yaw (in line with the wind direction). Each wheel was tested at tunnel and wheel rotational speeds of 30km/hr, 40km/hr and 50km/hr.

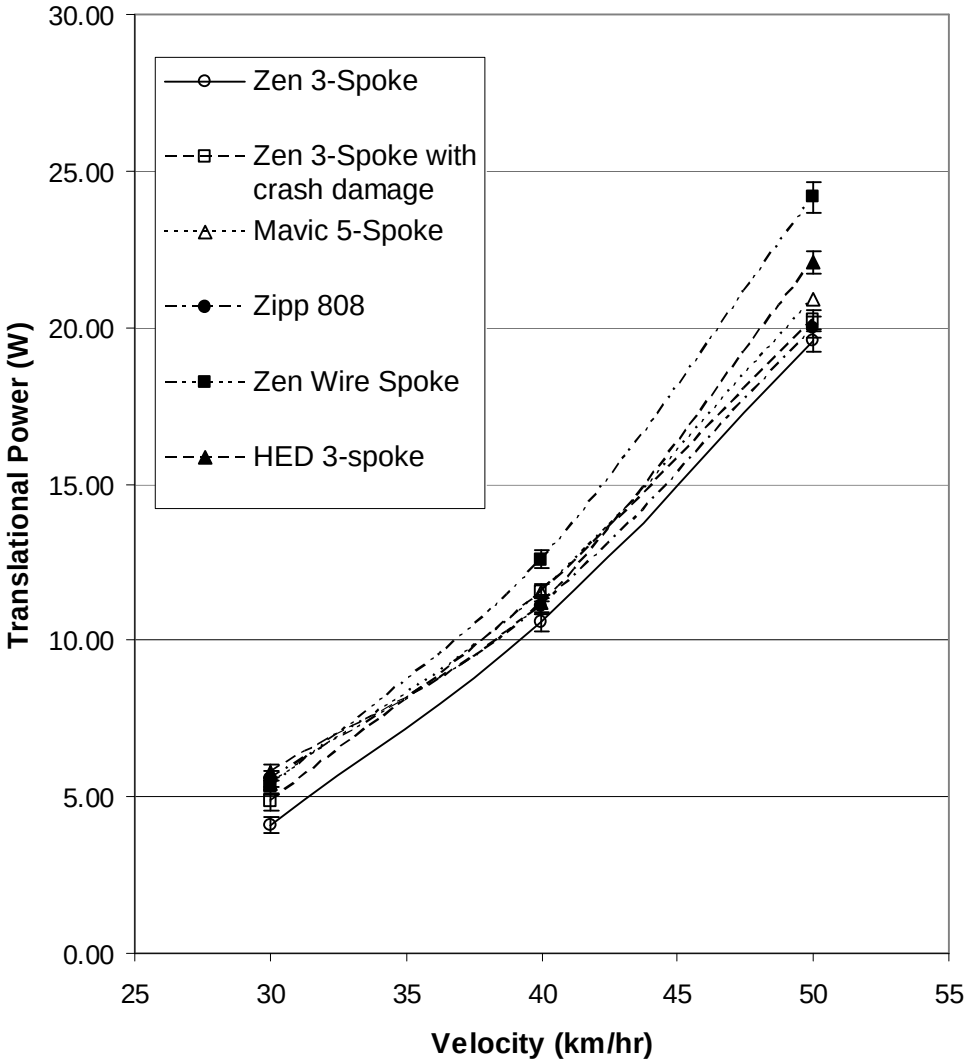


**Fig 7.2** Translational power of spoked wheels

Figure 7.2 shows the translational power of the spoked wheels. The Zen 3-spoke wheel (in good condition) has the lowest translational drag. As with the disc wheels, the translational power requirement is similar for all compression spoked wheels, The Zipp 808 wire spoked wheel requires similar power to the Zen and Mavic compression spoked wheels but the Zen wire spoke requires considerably more power than all other wheels when the velocity is 40km/hr and above. The differences in translational power are

slightly greater than the uncertainty ranges. The crash damage possibly increases the translational power required by the Zen wheel, but by less than the measurement uncertainty (Moore et al, 2008). The HED 3-spoke wheel has higher translational power reading than the Zen 3-spoke at every speed, with the differences at 40km/hr and 50km/hr being greater than the uncertainty.

For comparison, Zipp report the axial force on the 2004 model 808 wheel as 189g at 48kmh. The present data indicates 147±4g at 50kmh. The discrepancy may be due to differences in the wheel (yearly model changes) or tyre, or to differences in the rig (bare rig drag and efficacy of bare rig correction). The data at nonzero yaw cannot be compared directly as the wind conditions in the Zipp tests are not known (Zipp, 2006).

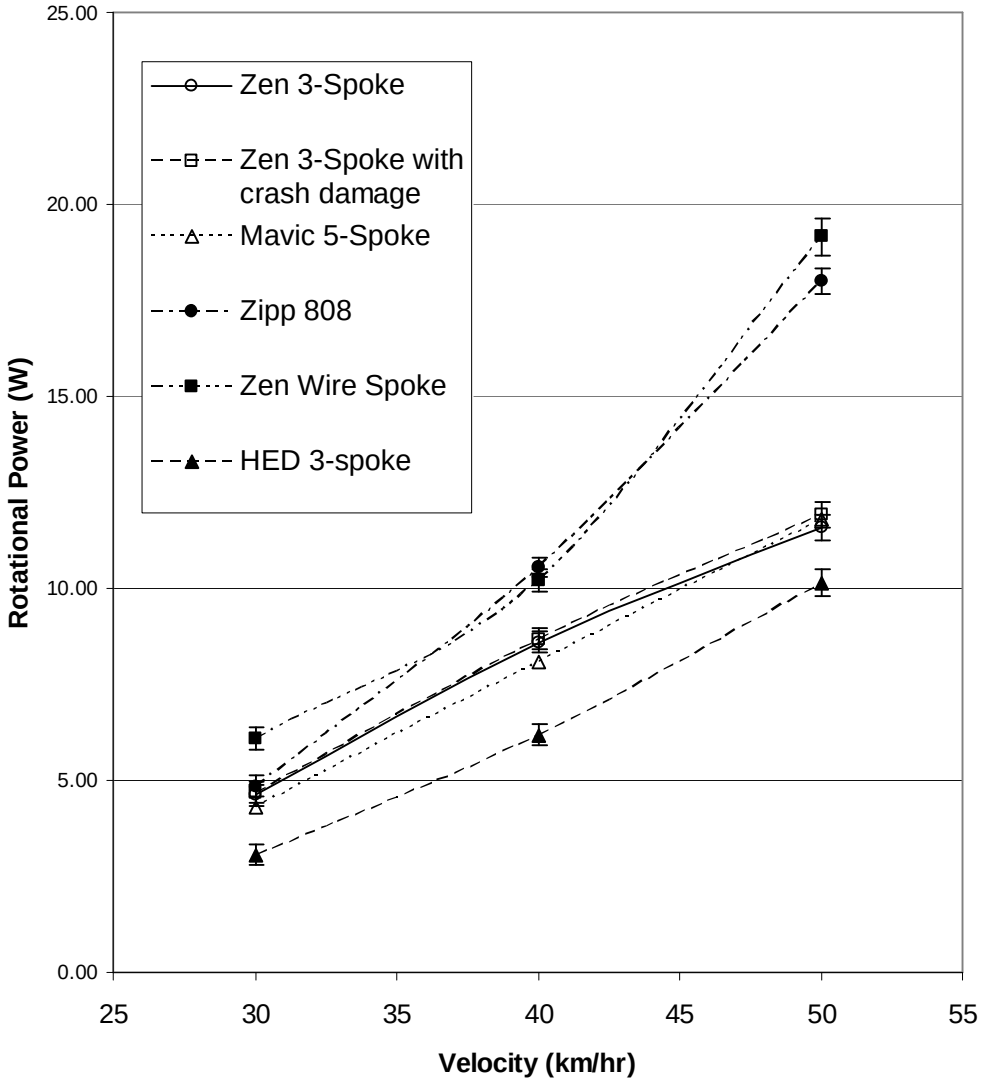


**Fig 7.3** Rotational power of spoked wheels

As with the discs, the rotational power of the spoked wheels (Figure 7.3) shows greater dependence on wheel design. There is a clear difference between wire and compression spoked wheels, with wire spoked wheels requiring significantly higher rotational power than the compression spoke wheels. The HED 3-spoke wheel shows significantly lower rotational power than all other wheels tested. There is little difference in rotational power between the Zen and Mavic compression spoked wheels, in fact the differences are less than the uncertainty ranges (Moore et al, 2008).

As with the disc wheels, the spoked wheels require slightly more power to translate than to rotate, though the ratio of rotational to total power is higher for the spoked wheels (45-55% for wire spoked, 37-55% for compression spoked wheels), than the discs (25-50%) (Moore et al, 2008).

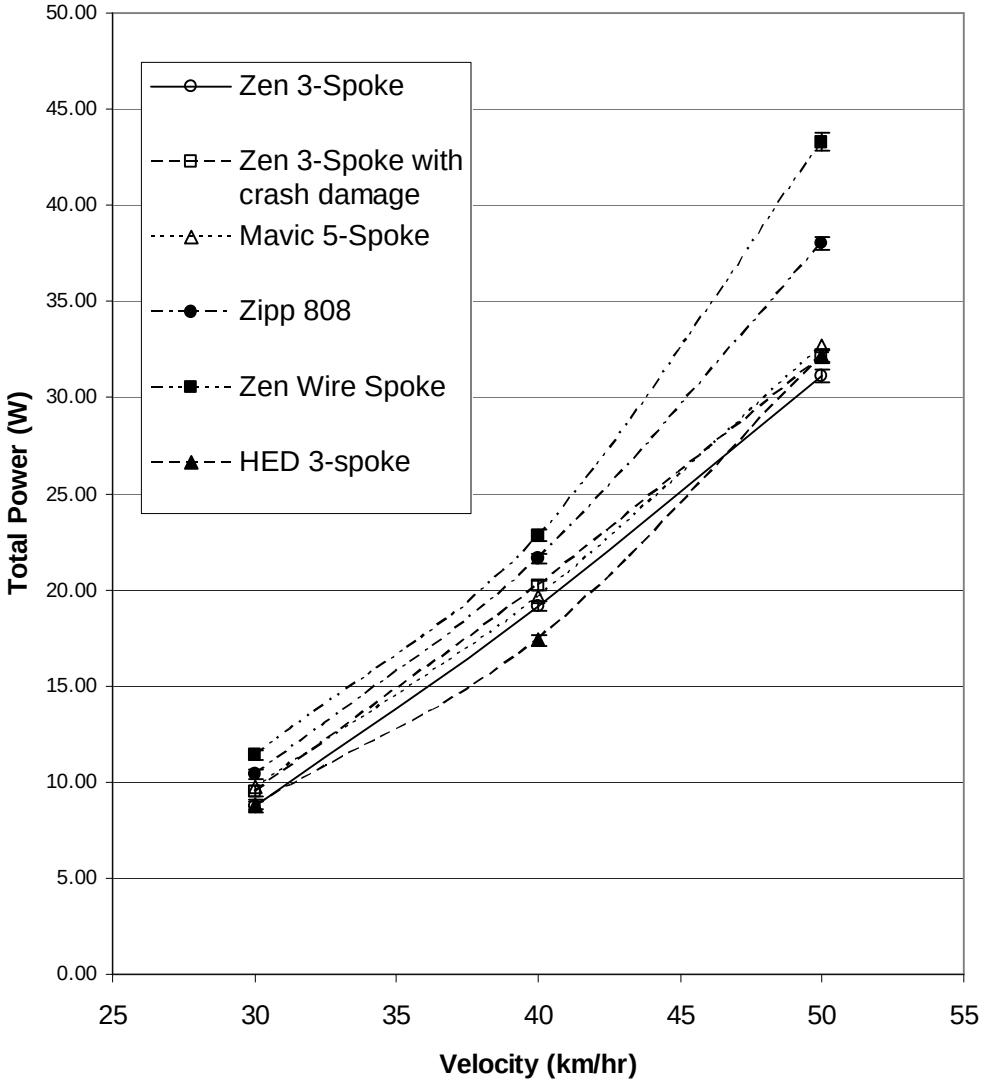


**Fig 7.4** Total power of spoked wheels

The total power for the spoked wheels, plotted in Fig. 7.4, shows the compression spoked wheels requiring less power than the wire spoked wheels at all speeds. The differences between the good and damaged finish of the Zen 3-spoke wheel, and the Mavic 5-spoke wheel, are within the uncertainty range and it is not possible to choose between these wheels on the basis of power at zero yaw (Moore et al, 2008). The HED 3-spoke wheel shows distinctly lower power at 40km/hr but at 30km/hr and 50km/hr, its total power requirement cannot be separated from the other compression spoked wheels due to the uncertainties.

The crash damage increases the total power requirement of the Zen wheel, but by less than the measurement uncertainty. That indicates that, while a smooth surface finish is important, it is the geometry which dominates the aerodynamic properties of each wheel (Moore et al, 2008).

### *7.2.2 Measurements with the Wheel at a Yaw Angle to the Airflow*

Each spoked wheel was tested in the wind tunnel at yaw angles of 10°, 20°, 30°, 40° and 50° and tunnel speeds of 30km/hr, 40km/hr and 50km/hr.

The yawed wheel data is presented in Figs. 7.5-7.7 as force on the wheel, resolved into two components: longitudinal (parallel to the wheel) and side (perpendicular to the wheel). The Zen 3-spoke wheel measured at yaw was in good condition with no crash damage.

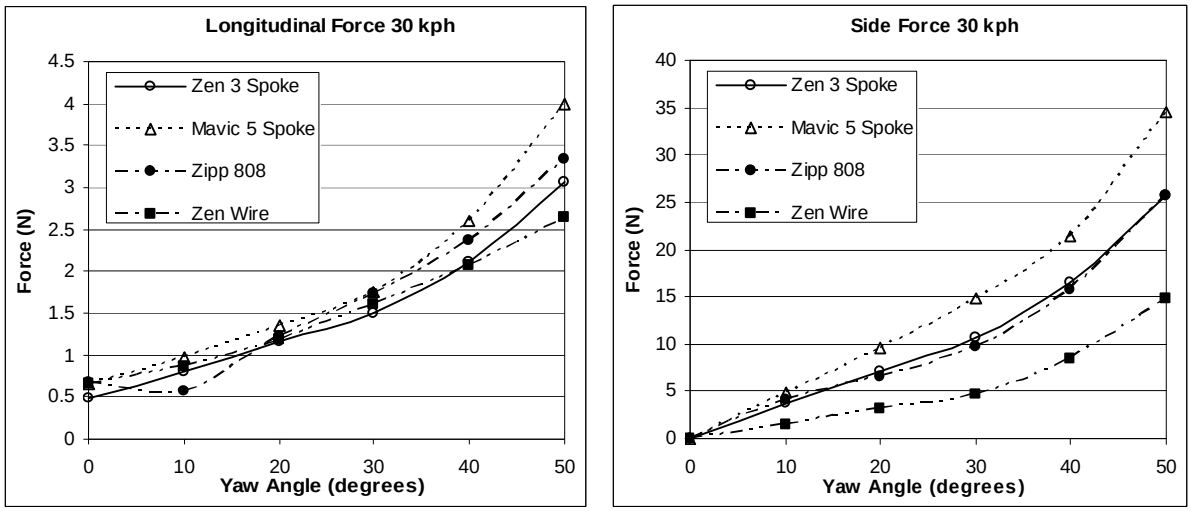


**Fig. 7.5** Longitudinal and side force versus yaw for spoked wheels at 30km/hr

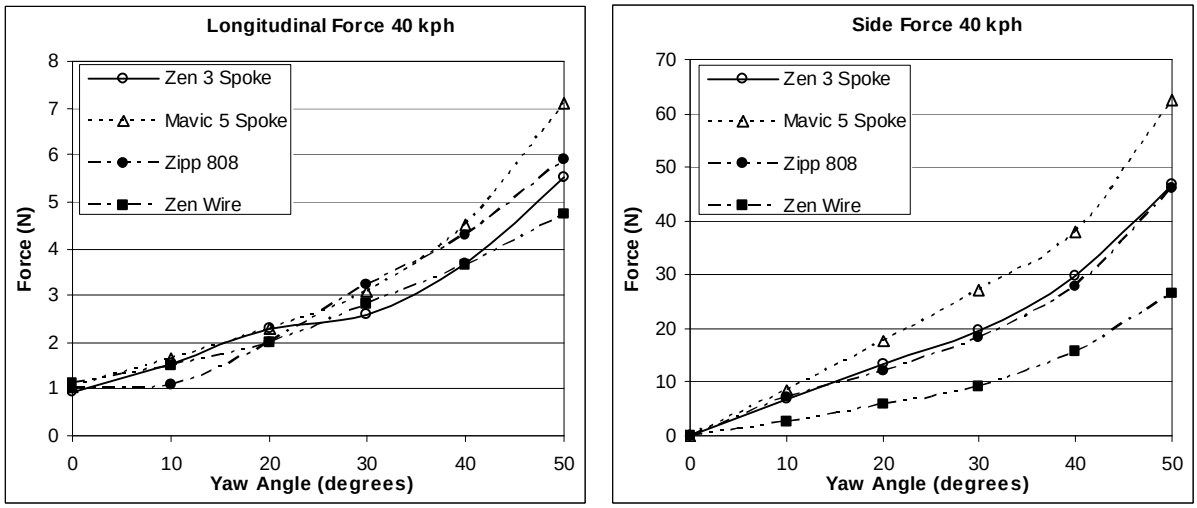


**Fig. 7.6** Longitudinal and side force versus yaw for spoked wheels at 40km/hr

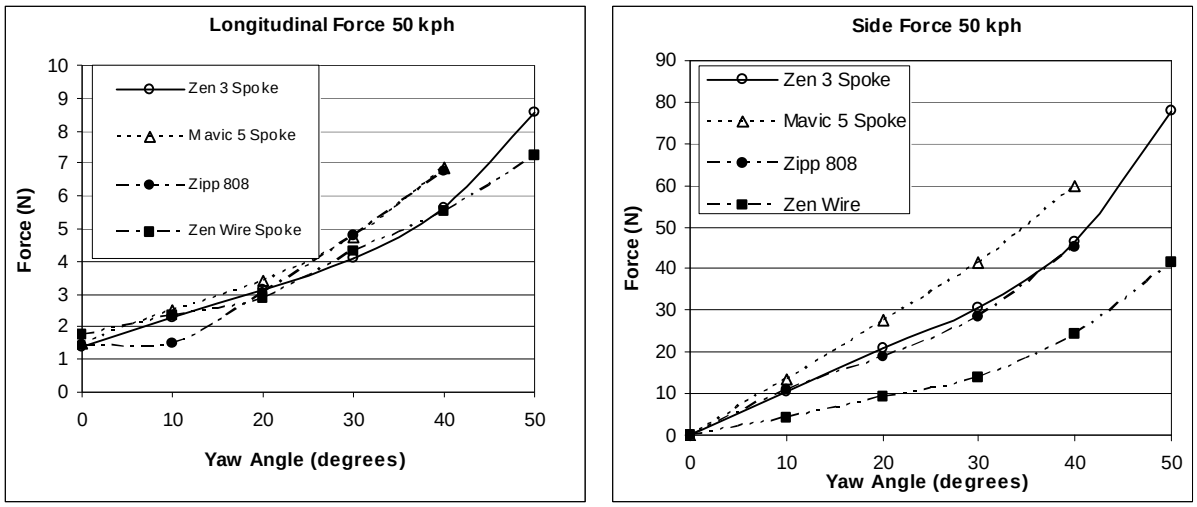


**Fig. 7.7** Longitudinal and side force versus yaw for spoked wheels at 50km/hr

Figs. 7.5-7.7 show the result that the wire spoked wheels experience much lower side force than the compression spoked wheels, as expected from their much lower projected area. However the Zen 3-spoke wheel experiences only slightly greater side force than the Zipp 808. In fact with the deep rim of the Zipp 808, these two wheels have very similar side projected area. Side force correlates with side projected area of the wheels. The correlation is not linear across the range of wheels, although the difference in side force between the two compression spoke wheels is ≈20%, very similar to the difference in side projected area, 17% (Moore et al, 2008).

The trends in side force are similar at all speeds. When the wheels are ranked in order of side force, the rank does not vary with speed or with yaw angle. The trends in longitudinal force are a little more complicated. At yaw angles of 40-50° the rank of the wheels in order of longitudinal force is unaffected by speed. At angles up to and including 30° the order depends on both yaw angle and speed. Some clear trends emerge.

The Mavic 5-spoke wheel always experiences longitudinal force at least as great as any other wheel tested. At 10° the Zipp 808 consistently experiences considerably lower longitudinal force than any of the other wheels. This is in line with the data presented on the Zipp website and with Zipp's stated design intention, to use the bulging, textured rim to keep the flow attached at the most frequently encountered yaw angles, 10-20° (Moore et al, 2008).

At 10° all wheels except the Zipp experience very similar longitudinal force, the Zipp being lower. At 20° all wheels, including the Zipp, show very similar longitudinal force. At 30° the Zen 3-spoke shows consistently lower longitudinal force than the other wheels, though the advantage is not as marked as the Zipp's at 10° (Moore et al, 2008).

Apart from the Zipp 808's reduced longitudinal force at $10^{o}$, the other wheels show a monotonic rise in longitudinal and side force with yaw angle. The Zen 3-spoke longitudinal force curve flattens at 20-30°, but only for 40kmh (Moore et al, 2008).

Comparing the two compression spoked wheels, they experience very similar drag force at zero yaw, but there is a clear difference in behaviour at yaw, with the Zen experiencing significantly lower longitudinal drag and side force (Moore et al, 2008).

This answers an important question for wheel designers; whether to design wheels with three, four or five spokes. These results indicate that at 0° yaw, there is little difference between the compression spoke wheels with different numbers of spokes, but at yaw

angles there is a definite advantage to keep the projected side area to a minimum i.e. have as few spokes as possible.

### *7.2.3 Measurement of Impact of Tyre Size on Drag*

It is likely that the 3-spoke wheel will be mostly used as an outdoor wheel as it compares well in cross-wind situations to the Zipp 808 which is currently a popular road racing wheel. The Zen disk also has a lower power requirement than the 3-spoke so is likely to be chosen ahead of the 3-spoke for track riding where no crosswinds are present. It was of interest to make improvements to the performance of the 3-spoke wheel when fitted with a 22mm tyre (compared to the 19mm tyre used in the wind tunnel tests) as larger tyres are more popular for outdoor use. Therefore, the Zen 3-spoke wheel was retested in the wind tunnel with a 22mm tyre to provide experimental results to use to validate the subsequent CFD models of the wheel.

**Table 7.2** Zen 3-Spoke power requirements with differing tyre sizes

| | Linear Power (W) | Rotational Power (W) | Total Power (W) |
|---|---|---|---|
| 19mm tyre | 19.57 | 11.57 | 31.14 |
| 22mm tyre | 25.57 | 13.17 | 38.67 |

The results in table 7.2 show that the increase in tyre size of just 3mm increases the linear power requirement by 31%, the rotational power requirement by 14% and the total power requirement by 24%. This is largely due to the increased frontal area with the bigger tyre and to a lesser extent, the increase in surface area, which affects the level of skin friction

drag. It is interesting to note that when the tyre was changed from 19mm to 22mm, the linear drag increased by 44g on both the Zen disk and 3-spoke wheel.

The Zen 3-spoke wheel was not originally designed for a 22mm tyre and drag could be improved with a 22mm tyre if the rim was made wider.

## 7.3 CFD Analysis

### *7.3.1 Translational and Rotational Power Prediction by CFD*

A computational fluid dynamics study of the front Zen 3-Spoke wheel with a 19m tyre was performed as described in Chapter 4. The forces on the wheel and axles were extracted from the data to compare them with the experimental forces. The CFD results are presented and compared with the experimental findings in Table 7.3.

**Table 7.3** CFD Analysis and experimental power results

| | Linear Power (W) | Rotational Power (W) | Total Power (W) |
|---|---|---|---|
| CFD | 23.29 | 6.18 | 29.48 |
| Experimental | 25.57 | 13.17 | 38.67 |

The linear power predicted by CFD is within 9% of the experimental data, which is an acceptable agreement. Just as with the disk wheel CFD simulations, the rotational power does not compare so well with a 53% discrepancy between the results. This large difference results in a 24% difference between the total power predicted by CFD and the experimental results. Therefore, the CFD results used for predicting wheel aerodynamic

improvements will focus on the trends of the data rather than the exact figures. Note that the CFD rotational power result for the 3-spoke wheel is higher that that predicted by CFD for the disk wheel, which matches the trend of the experimental results.

CFD indicated that the total force on the wheel was 72% pressure drag and 28% viscous drag. This indicated that modifying the wheel geometry to reduce pressure drag is an important area in which to investigate potential reductions in translational power.

### *7.3.2 Potential Sources of Rotational Power Error*

The discrepancy between the rotational power requirement predicted by CFD and that measured in the wind tunnel may be caused by several factors. Firstly, as the wheel rotates, each wheel is passing though the turbulent wake of the spoke before it. The turbulence model, while accurately predicting translational drag, may not be accurately predicting the turbulent flow between the spokes. A second cause of the error could be that the two-equation turbulence models are designed for use with high Reynolds number flows, such as around an airfoil, and lose accuracy at lower Reynolds numbers such as this. The adjustable constants used in the standard two-equation models are chosen as a compromise to give reasonably accurate predictions over a range of situations but are chosen for higher Reynolds numbers than the wheel experiences (0-100,000). These two effects may be improved by using a turbulence model such as the Large Eddy Simulation (LES) model, which can model turbulence more accurately than the simpler models (such as the k-ω SST model) but is significantly more expensive in terms of the computational power and time requirements (Fluent, 2006).

Another possible cause of the rotational power error is the potential for periodic vortex shedding off the trailing edges of the rim and spokes which would not be predicted in the steady-state simulation. This was investigated by running the converged, steady-state model as an unsteady simulation for 20 time steps of $7.53 \times 10^{-3}$ s each so that one rotation of the wheel at 50km/hr was modelled. The resultant force and moment on the wheel, and consequently the translational and rotational power, did not change between steady and unsteady simulations, ruling this out as a source of the error.

A further potential error source investigated was the fineness of the surface mesh. The convergence testing process described in section 4.4 concentrated on finding convergence of the linear drag force result rather than the rotational moment. Therefore, a simulation was undertaken with a surface mesh of 2mm, which provided an additional two million nodes to the simulation. The results of this simulation saw linear power drop by 3.0%, the rotational power increase by 4.5% and overall the total power dropped by 1.4% which can be considered a negligible change.

Therefore, it is concluded that the most likely cause of the rotational power error is that the turbulence model is not sufficiently accurate for this low Reynolds number situation.

*7.3.3 Discussion of CFD Results*

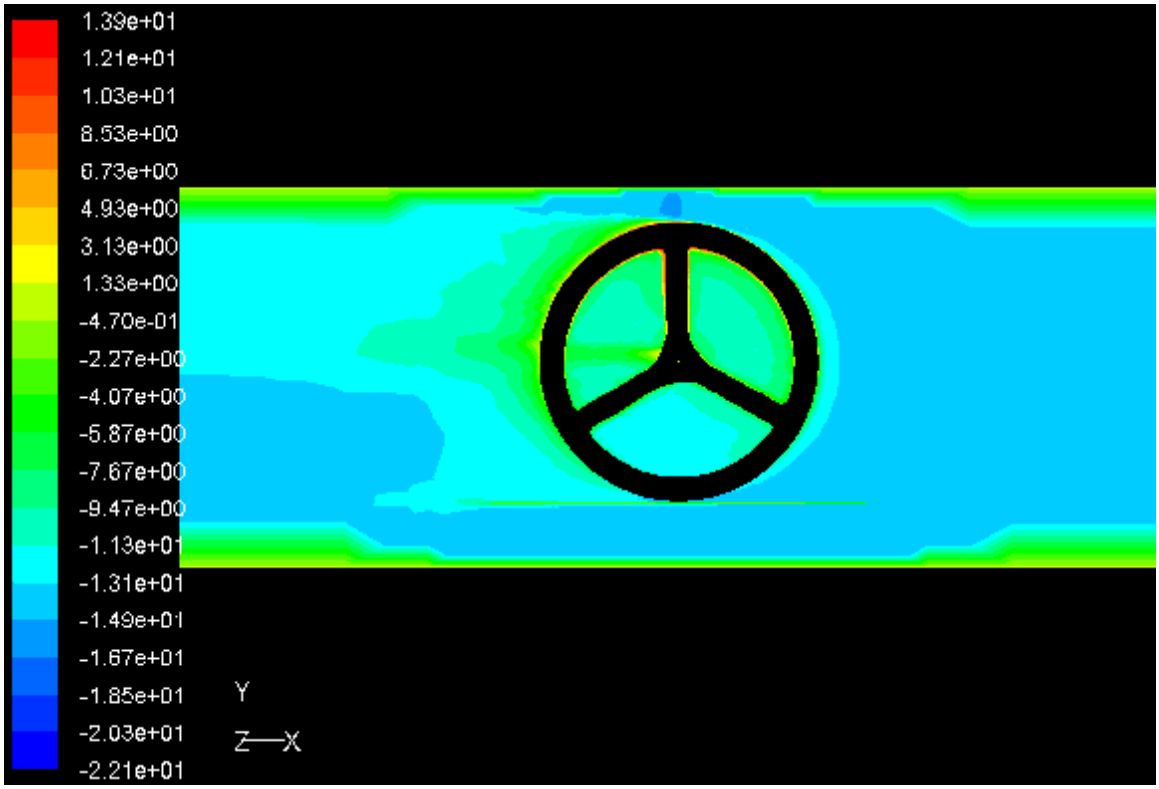


**Fig 7.8** Flow velocity in the x-direction around the Zen 3-Spoke wheel at 50km/hr

Figures 7.8-7.14 present results of the 3-D Fluent™ simulations. Fig 7.8 shows the velocity in the x-direction when the wheel the wheel is rotating and subjected to an airflow of 50km/hr. As was seen with the disk wheel, the wake develops behind the upper half of the wheel behind the forks which are influencing the flow.

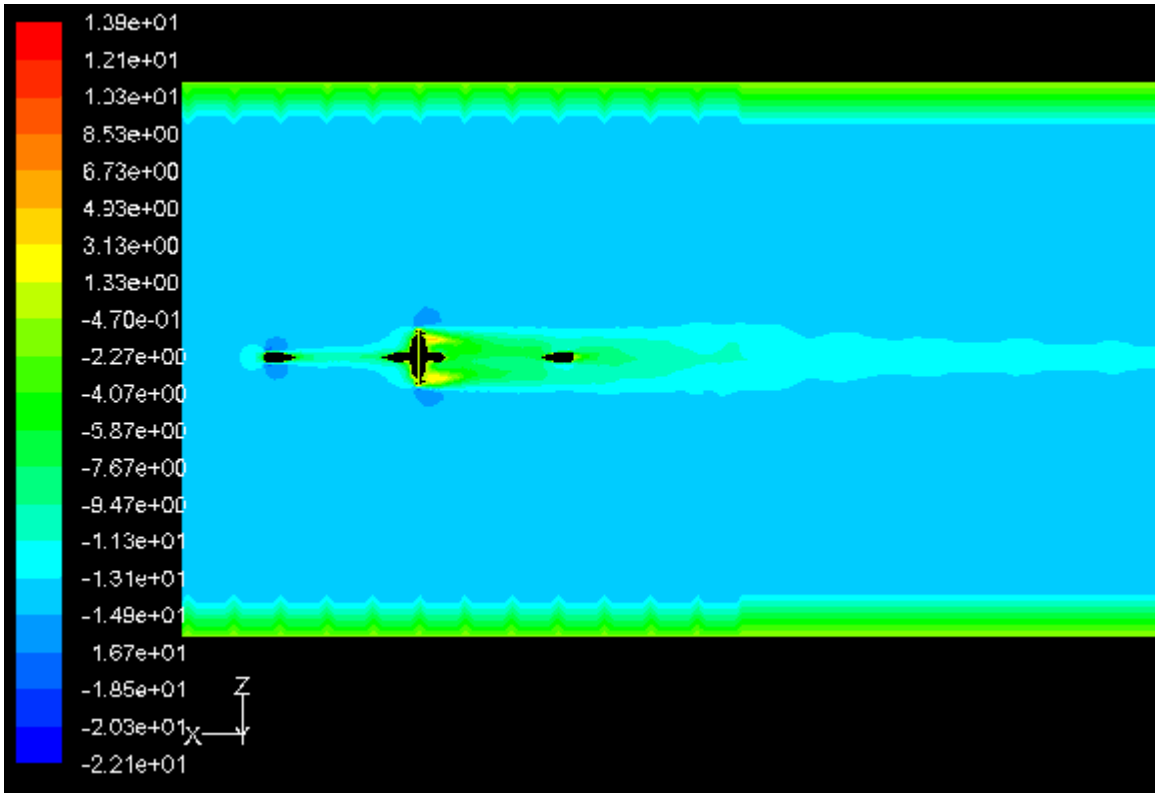


**Fig 7.9** Flow velocity in the x-direction around the Zen 3-Spoke wheel at 50km/hr (top view)

Figure 7.9 shows that, similar to the disk wheel, the width of the wake is governed by the width of the hub. Note, behind the hub, the regions of airflow in an opposite direction to the free stream (shown in yellow/red contours). This indicates that a recirculation eddy is present in this region. The percentage of translational drag from each of the wheel components is shown in Table 7.4.

**Table 7.4** Components of translational drag

| Wheel Component | Percentage of Translational Drag |
|---|---|
| Tyre | 54.5 |
| Wheel | 32.7 |
| Hub | 9.8 |
| Axle | 3.0 |

Table 7.4 indicates that the largest source of drag is from the tyre, which not a surprising result as the tyre meets the airflow front on. The wheel gives the next greatest portion of the drag due to it easily having the largest surface area.

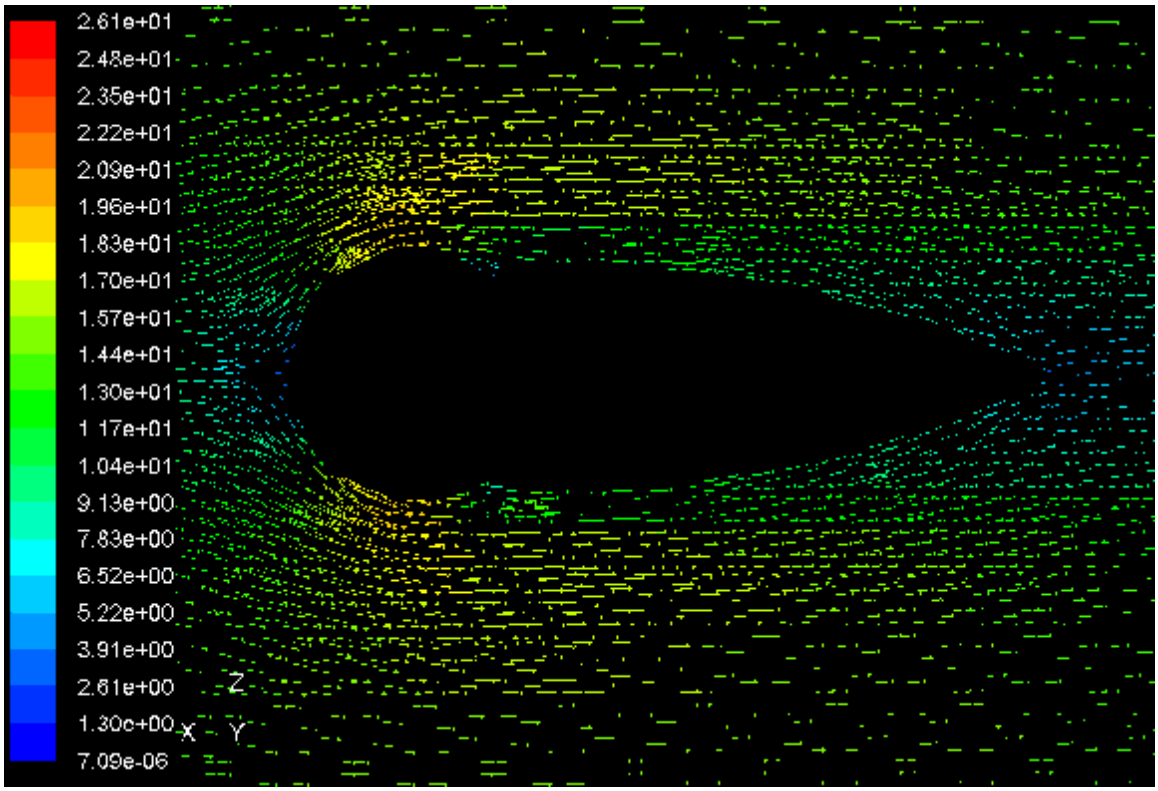


**Fig 7.10** Global vectors around front of wheel at mid-plane

A stagnation point is visible in figure 7.10 at the front of the wheel as the airflow meets the tube. A region of lower velocity flow directly behind the rim is also visible.

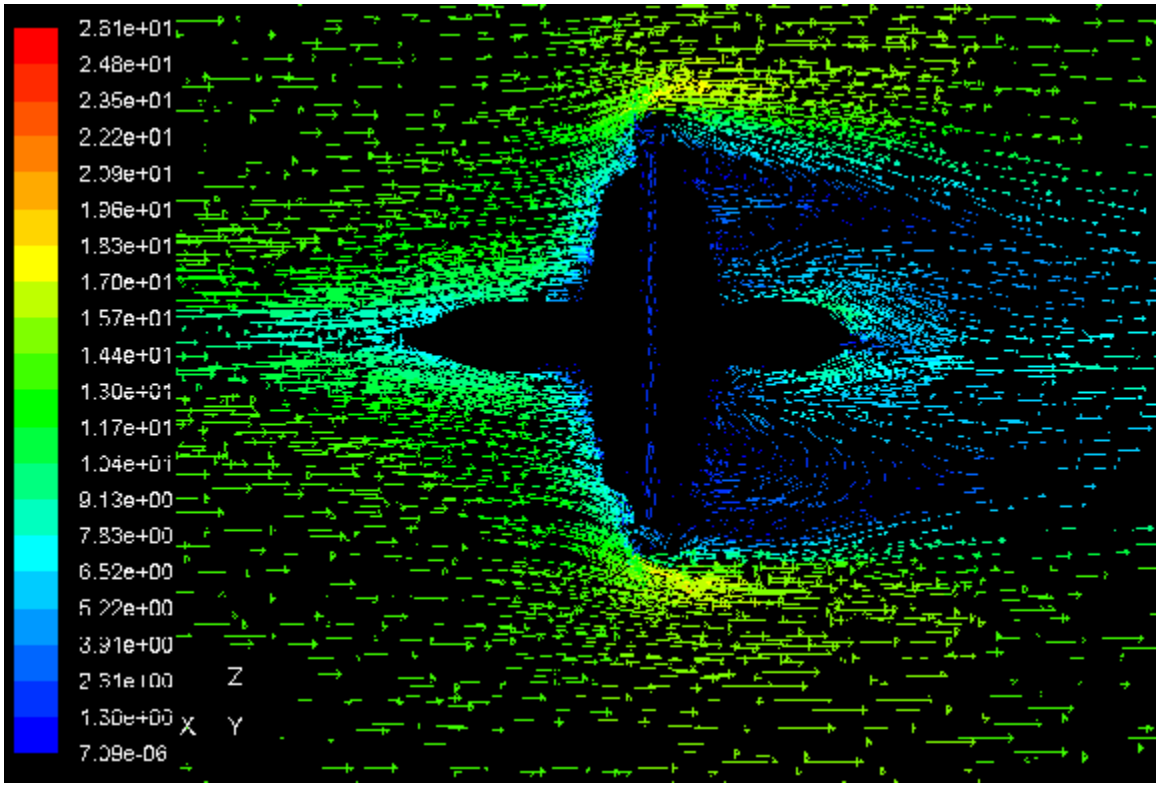


**Fig 7.11** Global velocity vectors around the hub at mid-plane

While the velocity vectors cause the hub to look like a significant source of drag, CFD predicts that only 10% of the drag on the wheel is caused by the hub. Two recirculation eddies are visible behind each hubcap and correspond to the contours of velocity showing reversed flow direction in figure 7.9. The low velocity vectors through the middle of the hub are due to a hole in the CAD model through the middle of the hub in which Fluent™ is assuming air is present. The airflow in this region is negligible and does not affect the translational drag.

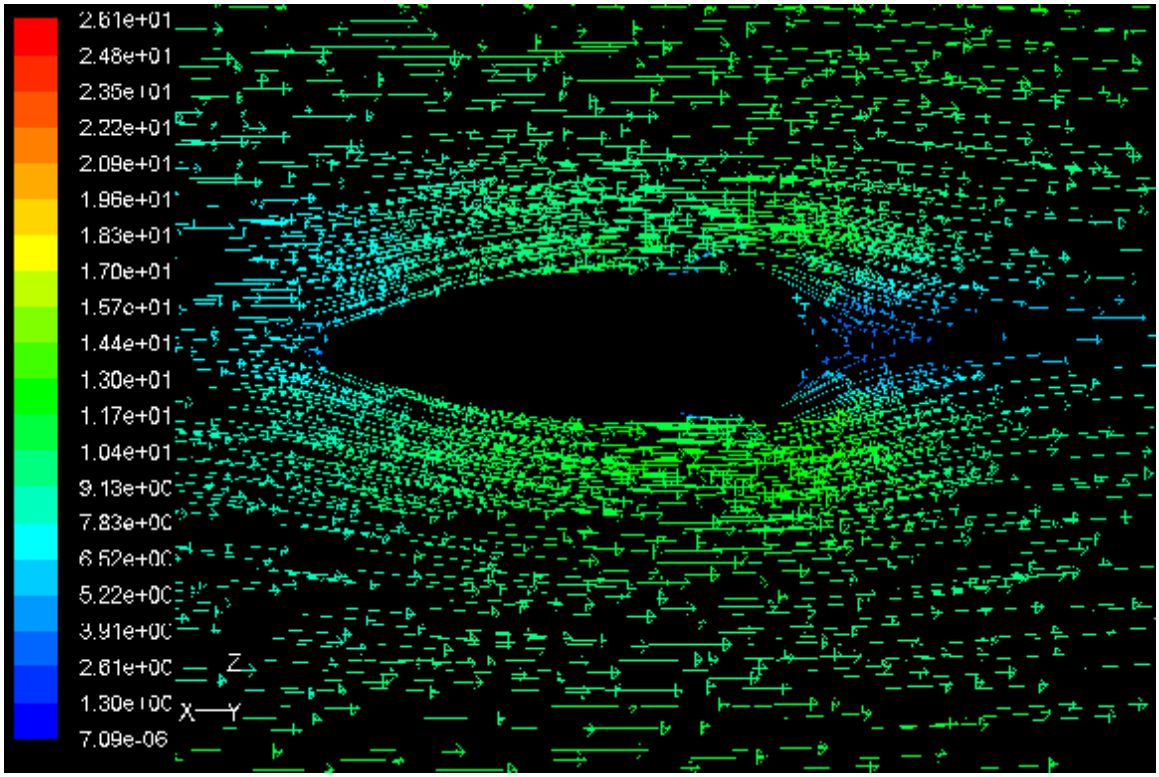


**Fig 7.12** Global velocity vectors at the rear of the wheel at mid-plane

Figure 7.12 shows stagnation points at both the front and back of the rim at its rear position. The area of stagnation at the trailing edge of the rim could be reduced by narrowing the trailing edge thickness (currently 2mm) or eliminating the current corner on the trailing edge by curving the geometry. The size of the stagnation point on the tyre is governed by the tyre size and surface roughness, which further supports the need to carefully pick the most appropriate tyre for a particular event. Flow separation is visible at the rear of the tyre.

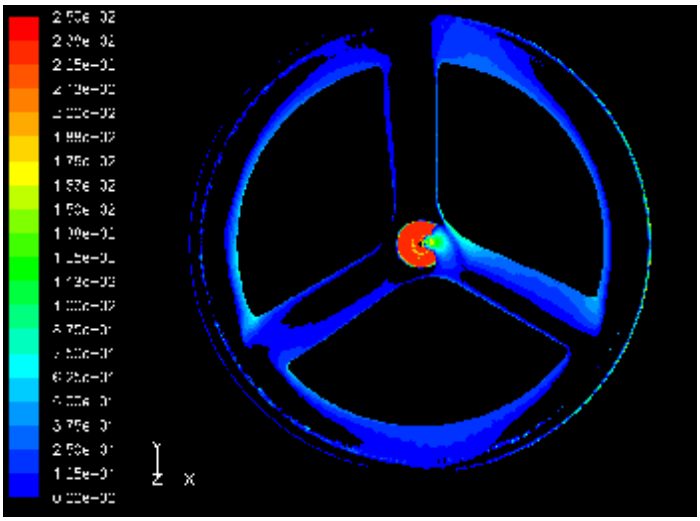

**Fig 7.13** Contours of positive pressure coefficient on the wheel surface at 50km/hr

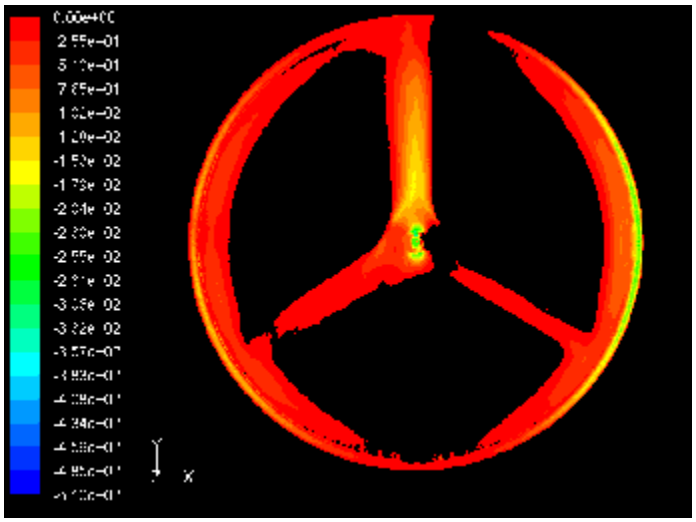

**Fig 7.14** Contours of negative pressure coefficient at 50km/hr

Figures 7.13 and 7.14 shows the contours of positive and negative pressure coefficients on the 3-spoke wheel. Note the high pressure coefficient on both sides of the hubcap (Fig. 7.13) as it has flow acting on it from both the front (bulk flow) and back (recirculation eddies).

At intermediate Reynolds numbers (~a few 1000 to ~500,000) laminar separation bubbles can form. They are known to form on some airfoils which have been optimised for higher Reynolds numbers. The bubbles increase drag significantly. Trips and turbulators are known to destroy the bubbles and reduce drag (Carmichael, 1981) (Selig, 1984). Therefore, trips and turbulators may have potential for reducing the drag on the 3-spoke wheel, which has many airfoil-like profiles.

### 7.4 Finite Element Analysis

As described in chapter 5, a model of the 3-spoke wheel was constructed within the software ANSYS$^{TM}$ 11.0 and analysed using finite element methods. Just as for the disk wheel, the focus on the analysis was on the strength and stiffness of the wheel structure when subjected to 30 kg load at the hub.

An experiment was performed to validate the results of the finite element analysis. The experiment consisted of supporting the 3-spoke wheel on each side of the wheel and placing a 30kg load at the hub. Two rim loading scenarios were tested as shown in fig. 7.15, the red dots indicating the rim mounting positions.

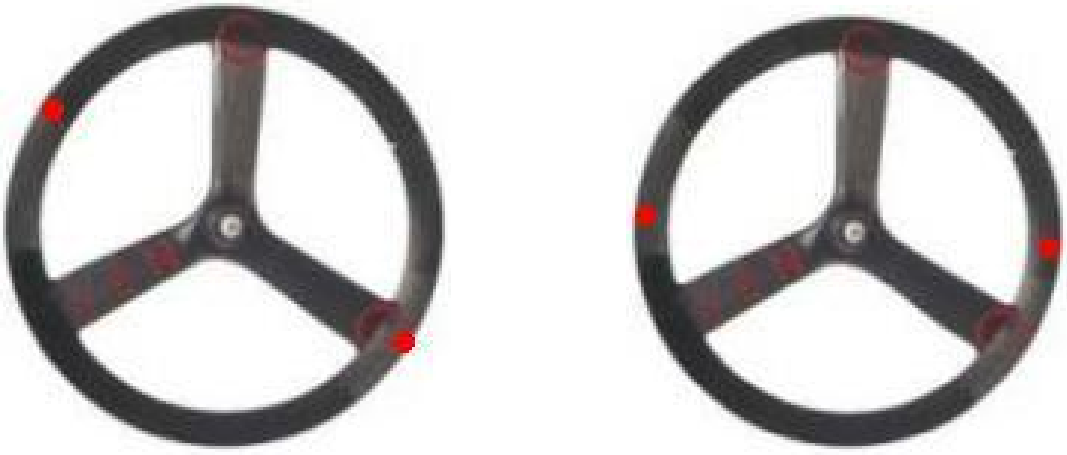

a) Rim held at position in-plane with spoke b) Rim held out of plane with spokes

**Fig 7.15** 3-Spoke wheel deflection tests

The deflection of the centre of the wheel when the 30kg load was applied was measured with a dial gauge to be 1.7mm for loading scenario no.1 (Fig 7.15a) and 2.0mm for loading scenario no.2 (Fig 7.15b). The finite element model used the loading scenario no. 2.


**Fig 7.16** Boundary conditions for 3-spoke ANSYS$^{TM}$ model

Due to the complex nature of the wheel geometry, and difficulties with modelling the interaction between the hub caps and the spokes for the three spoke wheel, it was decided to simplify the model by excluding the hub caps from the analysis. It is common in FE analysis to simplify the geometry in order to simulate the problem efficiently.

The FE analysis predicted the deflection at the centre of the wheel to be 8.1mm. This is greatly different to the experimental results and the discrepancy is thought to be due to the removal of the hub cups from the analysis. However, the result has the same order of

magnitude as the experimental result so is considered a reasonable basis for further investigation of the 3-spoke wheel structure.

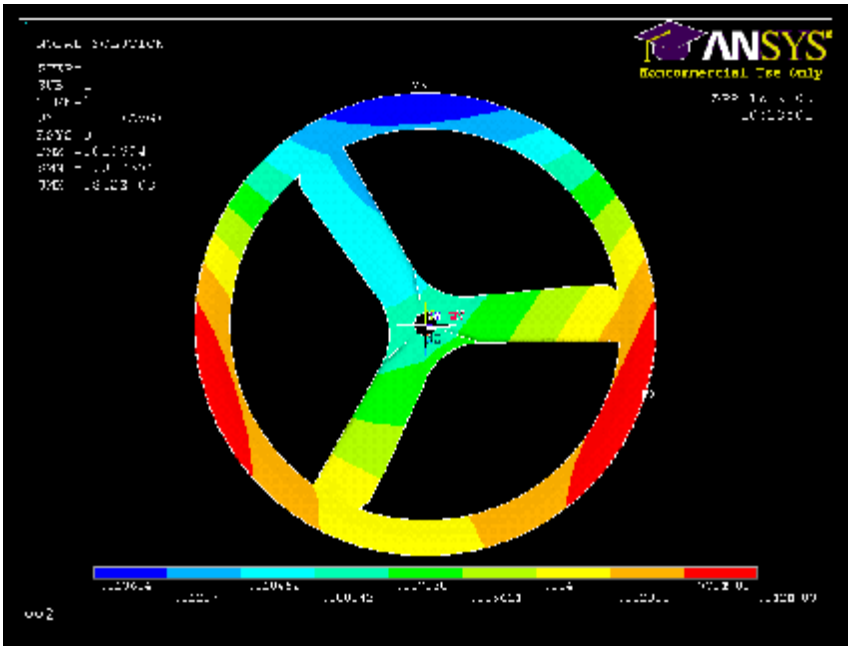


**Fig 7.17** Contours of vertical displacement for 3-spoke wheel with 30kg load (top view)

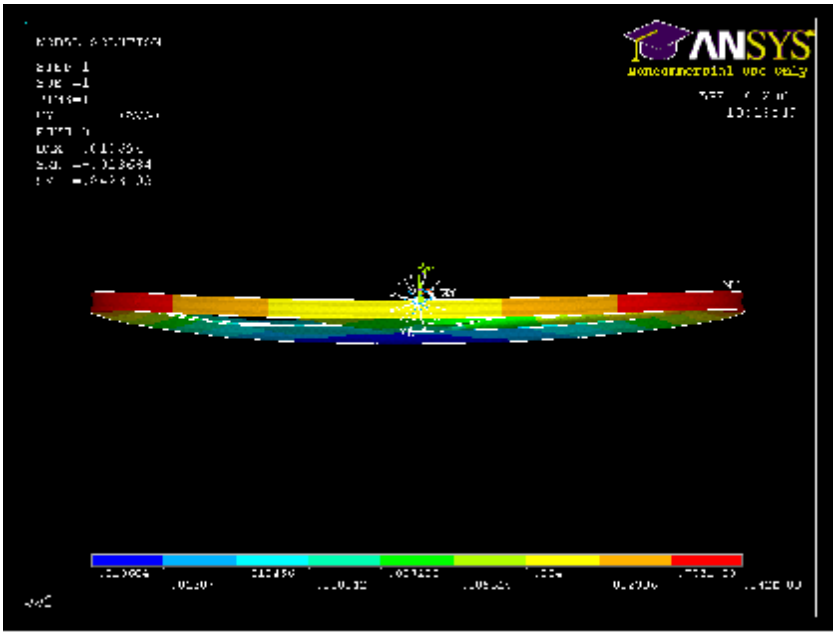


**Fig 7.18** Contours of vertical displacement for 3-spoke wheel with 30kg load (front view)

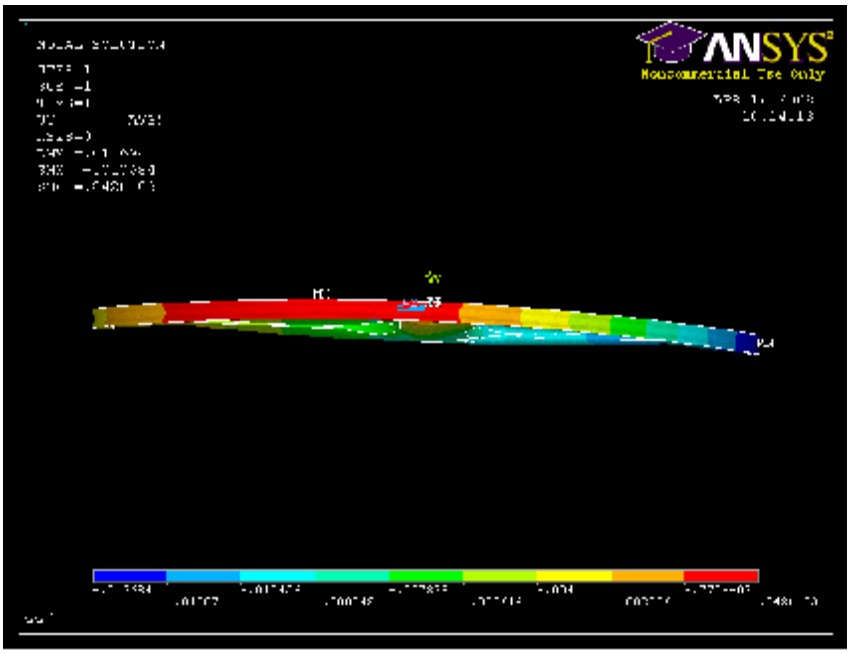


**Fig 7.19** Contours of vertical displacement for 3-spoke wheel with 30kg load (right view)

Figs. 7.17-7.19 show the vertical displacement of the 3-spoke wheel when 30kg is applied at the hub and the rim is restrained vertically at two points. It can be seen that the unsymmetrical geometry of the 3-spoke wheel is causing an uneven distribution of displacement around the rim. One third of the rim deflects downward to a greater degree than the other rim sections. This is thought to be due to the load path between the spoke and rim being different for each spoke in this loading situation. The airfoil spoke profile requires that the geometry at the join of each spoke and rim is different at the front and at the back of the spoke.

The maximum von-Mises stress in the wheel under this bending condition occurred in layer 12, which is a layer of unidirectional carbon fibre mat. The maximum stress of 611MPa is tensile as the layer is being elongated due to the bending. The tensile strength

of the M40JB fibres within the mat have a tensile strength of 4400MPa (Torayca, 2005) so the safety factor under this loading is 7.2. This safety factor is the minimum safety factor in the wheel. The areas of maximum stress are located at the boundary condition points – the wheel support points and the load application points.

### 7.5 Spoked Wheel Improvements

Several methods of reducing aerodynamic drag of the Zen 3-spoke wheel were investigated. Due to the commercially sensitive nature of the results, the findings of this investigation can only be broadly described in this thesis.

Paint applied to the wheel, which was then rotated in the wind tunnel with an oncoming airflow, showed that separation was occurring on some areas of the wheel. As mentioned in section 7.3.3, trips and turbulators are a method used to delay or prevent separation of airfoils. Therefore, the application of turbulators to different regions of the wheel was tested in the wind tunnel. A 3.8% reduction in the total power requirement for the wheel at 50km/hr was achieved with a particular turbulator configuration.

An extensive CFD investigation into possible geometry changes to the rim and wheel was conducted. Many possible shapes were tested, first in two-dimensional models and then in three-dimensional models if aerodynamic drag reduction was indicated. This investigation determined several geometric changes to the rim and spokes which had the effect of reducing the total power requirement of the wheel, with the best result being a 7.1% reduction in total power required to rotate and translate the wheel at 50km/hr.

In tandem with the CFD investigation, the geometric changes were applied to the finite element model to assess how the modified geometry affected the structural performance of the wheel. Options for changing wheel materials to maintain existing stiffness levels with the changed geometries were investigated.

### 7.6 Conclusion

The investigation of the spoked wheels produced a number of interesting findings:

- At 0° yaw, wire tension spoked wheels have a greater drag than compression spoked wheels
- At 0° yaw, it cannot be stated which of the Zen 3-spoke or Mavic 5-spoke performs better aerodynamically within the uncertainty of the measurement
- At yaw angles up to 50°, the Zen 3-spoke performs better than the Mavic 5-spoke due to the 3-spoke wheel having a lower side projected area
- The Zipp 808 shows the lowest axial force of all wheels at 10° yaw angle, confirming Zipp's design intention to keep flow attached in the most common yaw angles of 10°-20°

The investigation of the existing wheels also saw the development of CFD and FEA models which were used to make aerodynamic improvement to the 3-spoke wheel. These improvements cannot be commented on further due to them being commercially sensitive.

Chapter 8

# Research Conclusions

This research can be broadly divided into three main areas; experimental testing of bicycle wheels in the wind tunnel; determining an optimum width for the disk wheel; and developing improvements to the Zen 3-spoke wheel.

A test rig to measure translational and rotational drag of bicycle wheels in the closed circuit wind tunnel was designed and manufactured. The test rig has far greater accuracy and repeatability than the previous rig used for wheel research. Experimental testing of disk wheels found that wheels of varying hub widths have different aerodynamic properties. The translational power requirements of the wheels were similar and it was the rotational power requirement which set the wheels apart. The Zen convex disk wheel, which is 53mm wide at the hub, had a lower power requirement at 50km/hr than the Mavic convex disk (60mm) and Corima flat disk (20mm). The total power requirement of the disk wheels was 50-75% translational power and 25-50% rotational power.

Experimental testing of spoked wheels found that compression spoked wheels of three and five spokes required less power to translate and rotate than wire spoked wheels. The translational drag of the compression spoked wheels could not be separated due to the experimental uncertainty. The rotational power of the Mavic 5-spoke and Zen 3-spoke

also could not be separated but the HED 3-spoke had significantly lower rotational power than the other compression spoked wheels. The total power requirement of the compression spoked wheels was 50-62.5% translational power and 37.5-50% rotational power. The HED 3-spoke showed the lowest total power requirement at 40km/hr. At all other speeds, the difference in total power between the compression spoked wheels was smaller than the uncertainty.

The behaviour of the spoked wheels at yaw angles to the wind was also tested in the wind tunnel. The most significant result of the yaw testing was that the Zen 3-spoke wheel experienced very similar side forces to the Zipp 808, which is commonly considered as a good option for outdoor riding. The Zipp 808 wheel, however, had the lowest axial drag of all wheels at 10˚, which agrees with their claim of designing the wheel for best aerodynamic performance between 10˚-20˚ yaw angle.

A CFD analysis of disk and 3-spoke wheels was conducted. The translational drag predicted by CFD was in good agreement with the experimental results. The rotational drag did not achieve good agreement, most likely because the turbulence model used was designed for higher Reynolds number airflows.

A FE analysis was also conducted on the disk and 3-spoke wheels. The FE model of the disk wheel achieved good agreement with experimental deflection tests but the 3-spoke wheel model did not achieve as good agreement. This is most likely due to the hub being removed from the FE model to simplify the geometry.

Improvements to the aerodynamic properties of the disk wheel and 3-spoke wheel were identified via CFD, FEA and experimental testing but cannot be reported further here due to the commercially sensitive nature of the findings.

Chapter 9

# Future Work

During the course of this research into aerodynamic improvements of bicycle wheels, a number of areas have been identified as having potential for future research and work.

1. The experimental rig would benefit from having the load cell data acquisition system and the motor system controlled within one piece of software (i.e. LabView$^{TM}$).
2. Several disk wheels of hub widths around the predicted optimum width could be tested in the wind tunnel to confirm the optimum disk wheel width.
3. Prototypes of the 3-spoke wheel with the modified geometries could be manufactured and tested in the wind tunnel.
4. A detailed analysis of available CFD turbulence models including, perhaps, tuning of the model constants to best suit the wheel simulations may help improve the accuracy of the CFD values compared to the experimental results.
5. The ANSYS$^{TM}$ model of the 3-spoke wheel could be made more realistic by adding the hub structure.
6. Experimental testing of the effect of yaw angles on disk wheels would add to the understanding of disk wheel performance
7. The interaction between the wheel and forks was not investigated as part of this research so it would useful to know how the forks affect the aerodynamic properties of the wheels

8. The wheels tested and simulated were all in the front wheel position. Further investigation of the aerodynamics of the wheel positioned at the back of the bike, where the airflow is disturbed by pedalling legs and bicycle frame, would be useful.

# References


Carmichael, B. (1981). Low Reynolds Number Airfoil Survey, NASA CR-1165803.

Cook, R. D., Malkus, D. S., Plesha, M. E., & Whitt, R. J. (2002). *Concepts and applications of finite element analysis* (4th ed.). New York: John Wiley & Sons Ltd.

Daugherty, A. (1983). A study of the drag reduction of a two-wheeled human powered vehicle. *AIAA, 83-0655*(January 1983).

Fluent. (2005). *Fluent 6.2 User's Guide*

Fluent. (2006). *Fluent 6.3.26 User's Guide*

Greenwell, D. I., Wood, N. J., Bridge, E. K. L., & Addy, R. J. (1995). Aerodynamic characteristics of low-drag bicycle wheels. *Aeronautical Journal, 99*(1995), 109-120.

Grimshaw, P. (2007). *Sport and exercise biomechanics.* New York: Taylor & Francis.

Hopkins, M. W., Principe, F. S., & Kelleher, K. J. (1990, April 2-5, 1990). *Beyond Materials: Du Pont's Aerodynamic Bicycle Wheel.* Paper presented at the 35th International SAMPE Symposium.

Kühnen, R. (2005). Gegen den Wind (Special report on competition wheels). *Tour Magazine, 9,* 24-30.

Kyle, C., & Burke, E. (1984). Improving the racing bicycle. *Mechanical Engineering, September 1984,* 36-45.

Kyle, C., & Weaver, M. (2004). Aerodynamics of human-powered vehicles. *Proc. Inst. Mech. Engrs. Part A J. Power and Energy, 218,* 141-154.

McManus, J., & Zhang, X. (2006). A Computational Study of the Flow Around an Isolated Wheel in Contact with the Ground. *Journal of Fluids Engineering, 128,* 520-530.

Massey, B. S. (1998). *Mechanics of Fluids* (7th ed.). Cheltenham, England: Stanley Thornes.

Moore, J. K., Bloomfield, M., & Jermy, M. C. (2008). Linear and rotational aerodynamic drag of composite construction bicycle wheels. *Journal of Sports Engineering, (In review).*

Rouesartisanales. (2008). Retrieved February, 2008, from http://www.rouesartisanales.com/article-15505311.html

Sayers, A. T., & Stanley, P. (1994). Drag force on rotating racing cycle wheels. *Journal of Wind Engineering and Industrial Aerodynamics, 53*(3), 431-440.

Selig, M. (1984). The Design of Airfoils at Low Reynolds Numbers. *Soar Tech, 3*.

Shimano. (2006). Retrieved 5th May, 2008, from http://techdocs.shimano.com/media/techdocs/content/cycle/EV/actionsports/WH/EV-WH-R561-F-2563_v1_m56577569830608670.pdf

Sunter, R., & Sayers, A. (2001). Aerodynamic drag of mountain bike tyres. *Sports Engineering, 4*, 63-73.

Tew, G. S., & Sayers, A. T. (1999). Aerodynamics of yawed racing cycle wheels. *Journal of Wind Engineering and Industrial Aerodynamics, 82*(1-3), 209-222.

Torayca. (2005). *Carbon Fibre Properties*. Retrieved 10th April, 2008, from www.torayca.com/properties/en/images/report_eng01_2.html

Willett, K. (2006). *Zipp 808 vs. Specialized Trispoke*, from http://www.biketechreview.com/

Wilson, D. (2004). *Bicycling Science* (3rd ed.). Cambridge, Mass: MIT Press.

Zdravkovich, M. M. (1992). Aerodynamics of bicycle wheel and frame. *Journal of Wind Engineering and Industrial Aerodynamics, 40*(1), 55-70.

Zhang, X., Toet, W., & Zerihan, J. (2006). Ground Effect Aerodynamics of Race Cars. *Applied Mechanics Reviews, 59*, 33-49.

Zipp. (2006). *A note on spoke count in aerodynamic bicycle wheels, A note on spoke shape in modern aerodynamics bicycle wheels, A note on rim width, tire sensivity and rim depth in high performance bicycle wheels*. Retrieved 10th December, 2007, from www.zipp.com

Zipp. (2007). *Zipp Wheel Instruction Manual*. Retrieved January 15, 2008, from http://www.zipp.com/portals/0/support/documents/ZIPP_A6_Wheel%20Manual_0306.pdf

Zipp. (2008). *Zipp Speed Weaponry 2008*. Retrieved April 1st, 2008, from http://www.zipp.com/Portals/0/Files/ZippCatalog2008.pdf

# Appendix A – Sample Test Rig Uncertainty Calculation

**Table A1** Uncertainty Calculation Nomenclature

| Symbol | Description | Unit | Error term |
|---|---|---|---|
| $D_R$ | Translational drag of bare rig | kg | $E_{DR}$ |
| $D_{R+W}$ | Translational drag of rig and wheel | kg | $E_{DRW}$ |
| $D_W$ | Translational drag of wheel only | kg | $E_{DW}$ |
| $M_R$ | Rotational drag of bare rig | kg | $E_{MR}$ |
| $M_{R+W}$ | Rotational drag of rig and wheel | kg | $E_{MRW}$ |
| $M_W$ | Rotational drag of wheel only | kg | $E_{MW}$ |
| $F_T$ | Translational force | N | $E_{FT}$ |
| $P_T$ | Translational power | W | $E_{PT}$ |
| $F_R$ | Rotational force | N | $E_{FR}$ |
| $T_R$ | Rotational torque | Nm | $E_{TR}$ |
| $P_R$ | Rotational power | W | $E_{PR}$ |
| $P_{TOTAL}$ | Total power | W | $E_{PTOTAL}$ |
| | Standard error of reading | kg | $E_S$ |
| | Load cell calibration | kg | $E_{LC}$ |
| | Calibration weight uncertainty | kg | $E_{CW}$ |
| v | Tunnel velocity | km/hr | $E_v$ |
| v-mot | Motor speed | rpm | $E_{v\text{-}mot}$ |
| $r_{pulley}$ | Drive pulley radius | m | $E_{rpulley}$ |
| $r_{wheel}$ | Wheel radius | m | $E_{rwheel}$ |
| $r_{lever}$ | Radius of lever arm | m | $E_{rlever}$ |

## Translational Power

$D_R$ = 0.1038kg ± 0.0014kg

$E_{DR}$ = ± ($E_S$ + $E_{LC}$ + $E_{CW}$)
= ± (0.00274 + 0.001 + 0.0001)
= ± 0.0014kg

$D_{R+W}$ = 0.2522kg ± 0.0019kg

$E_{DRW}$ = ± ($E_S$ + $E_{LC}$ + $E_{CW}$)
= ± (0.008197 + 0.001 + 0.0001)
= ± 0.0019kg

$D_W$ = $D_{R+W}$ - $D_R$
= 0.2552kg – 0.1038kg
= 0.1484kg ± 0.0024kg

$E_{DW} = \pm\sqrt{E_{DR}^2 + E_{DRW}^2}$
$= \pm\sqrt{0.0014^2 + 0.0019^2}$
= ± 0.0024kg

$F_T$ = $D_W$ x gravity
= 0.1484kg x 9.81m/s$^2$
= 1.456N ± 0.023N

$E_{FT}$ = ± ($E_{DW}$ x 9.81)
= ± 0.0024kg x 9.81
= ± 0.023N

$P_T$ = $F_T$ v/3.6
= (1.456N x 50km/hr)/3.6
= 20.2W ± 0.3W

$E_{PT}$ =

$$\pm\frac{P_T}{3.6}\sqrt{\left(\frac{E_{FT}}{F_T}\right)^2+\left(\frac{E_v}{v}\right)^2+\left(\frac{E_{v-mot}}{v-mot}\right)^2+\left(\frac{E_{rpulley}}{rpulley}\right)^2+\left(\frac{E_{rwheel}}{rwheel}\right)^2}$$

=

$$\pm\frac{72.79}{3.6}\sqrt{\left(\frac{0.023}{1.456}\right)^2+\left(\frac{0.2}{50}\right)^2+\left(\frac{5}{7871}\right)^2+\left(\frac{0.00005}{0.016585}\right)^2+\left(\frac{0.001}{0.333}\right)^2}$$

= ± 0.3W

**Rotational Power**

$M_R$ = 0.0578 ± 0.0014kg

$M_{R+W}$ = 0.0842 ± 0.0016kg

$M_W$ = $M_{R+W}$ - $M_R$
= 0.0842kg – 0.0578kg
= 0.0264kg ± 0.0021kg

$F_R$ = $M_W$ x gravity
= 0.0264kg x 9.81m/s$^2$
= 1.259N ± 0.021N

$T_R$ = $F_R$ x $r_{lever}$
= 1.259N x 0.055m
= 0.014Nm ± 0.001Nm

$P_R$ = $T_R \omega$
= $\frac{0.014\text{Nm} \times 50\text{kmhr}}{3.6 \times 0.016585\text{m}}$
= 11.9W ± 1.0W

***Total Power***

$P_{TOTAL}$ = $P_T$ + $P_R$
= 20.2W + 11.9W
= 32.1W ± 1.0W

$E_{MR}$ = ± ($E_S$ + $E_{LC}$ + $E_{CW}$)
= ± (0.002972 + 0.001 + 0.0001)
= ± 0.0014kg

$E_{MRW}$ = ± ($E_S$ + $E_{LC}$ + $E_{CW}$)
= ± (0.004505+ 0.001 + 0.0001)
= ± 0.0016kg

$E_{MW} = \pm\sqrt{E_{MR}^2 + E_{MRW}^2}$
$= \pm\sqrt{0.0014^2 + 0.0016^2}$
= ± 0.0021kg

$E_{FR}$ = ± $E_{MW}$ x 9.81
= 0.021N

$$E_{TR} = \pm T_R\sqrt{\left(\frac{E_{FR}}{F_R}\right)^2 + \left(\frac{E_{rlever}}{rlever}\right)^2}$$
$$= \pm 0.014\sqrt{\left(\frac{0.021}{1.259}\right)^2 + \left(\frac{0.0005}{0.055}\right)^2}$$
= ± 0.001Nm

$$E_{PR} = \pm P_R\sqrt{\left(\frac{E_{TR}}{T_R}\right)^2 + \left(\frac{E_v}{v}\right)^2 + \left(\frac{E_{rpulley}}{rpulley}\right)^2 + \left(\frac{E_{v-mot}}{v-mot}\right)^2 + \left(\frac{E_{rwheel}}{rwheel}\right)^2}$$

$$= \pm 11.91\sqrt{\left(\frac{0.001}{0.014}\right)^2 + \left(\frac{0.2}{50}\right)^2 + \left(\frac{0.00005}{0.016585}\right)^2 + \left(\frac{5}{7871}\right)^2 + \left(\frac{0.001}{0.333}\right)^2}$$

= 1.0W

$E_{PTOTAL} = \pm\sqrt{E_{PT}^2 + E_{PR}^2}$
$= \pm\sqrt{0.3^2 + 1.0^2}$
= ± 1.0W

# Appendix B – LabView™ Program User's Guide

**Instructions for using LabView to take force measurements.**

1. Open LabView from Start menu>Programs>LabView

2. Select the file “WheelRig01JKM6”

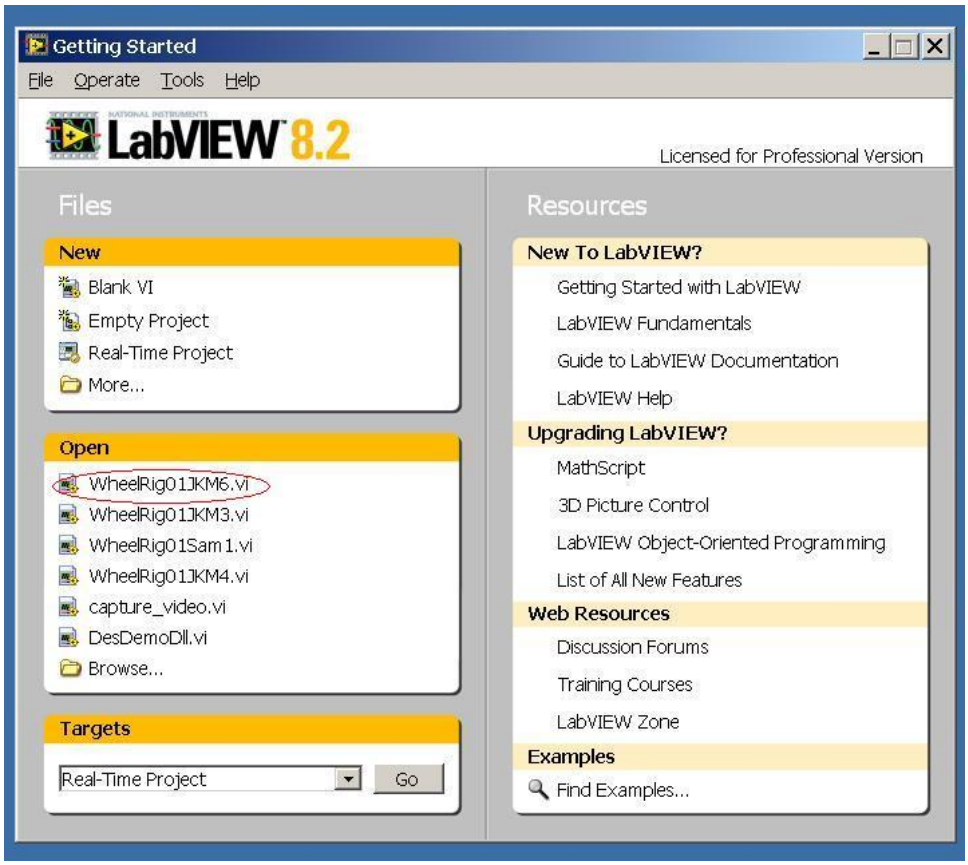


3. On the LabView front screen, set the load cell sampling parameters as shown below:

**4.** On the LabView block diagram, ensure ‘1000’ is typed the boxes circled in red below.

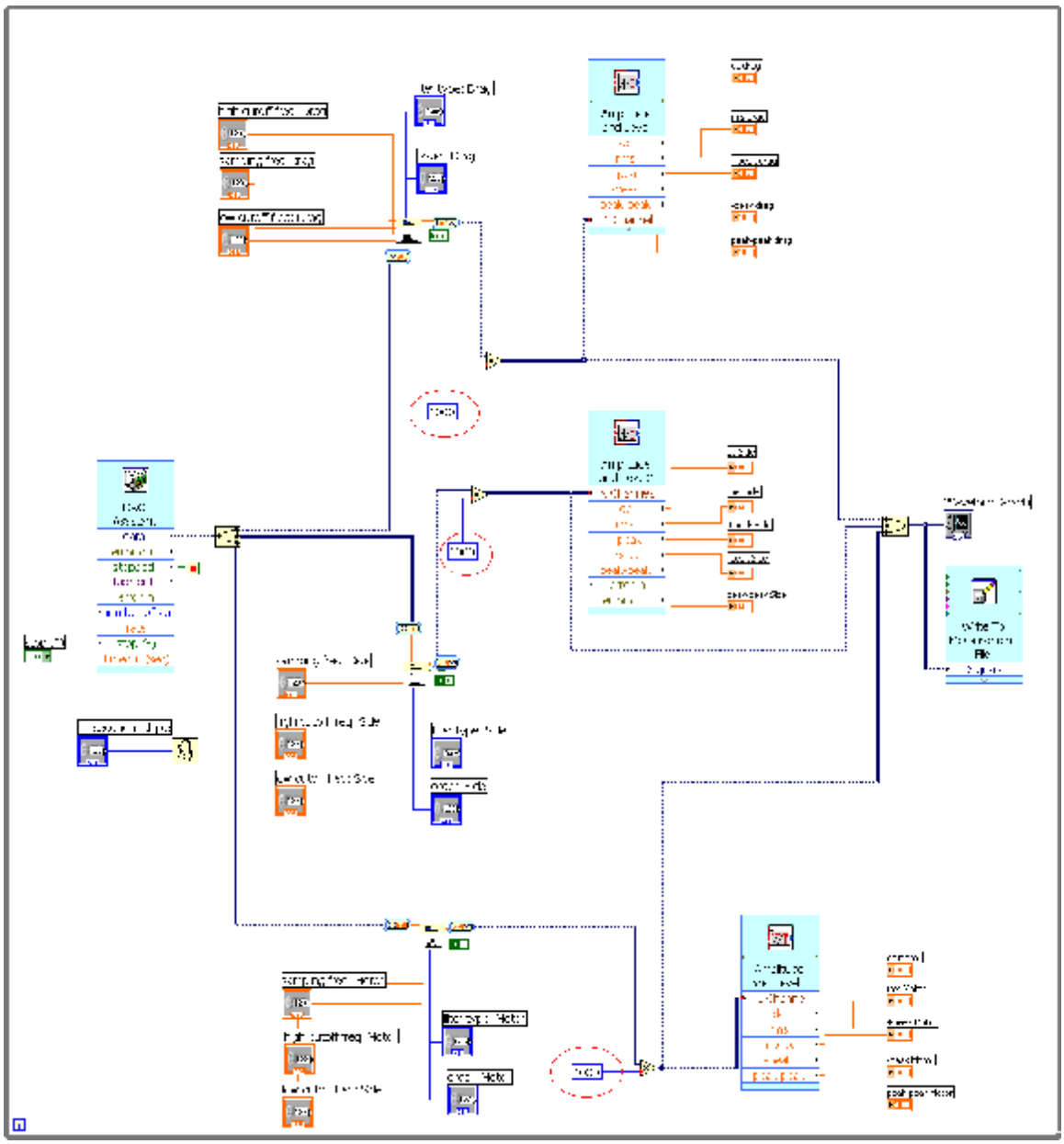

5. To start a run, click on the black arrow button at the top left of the LabView frontscreen.

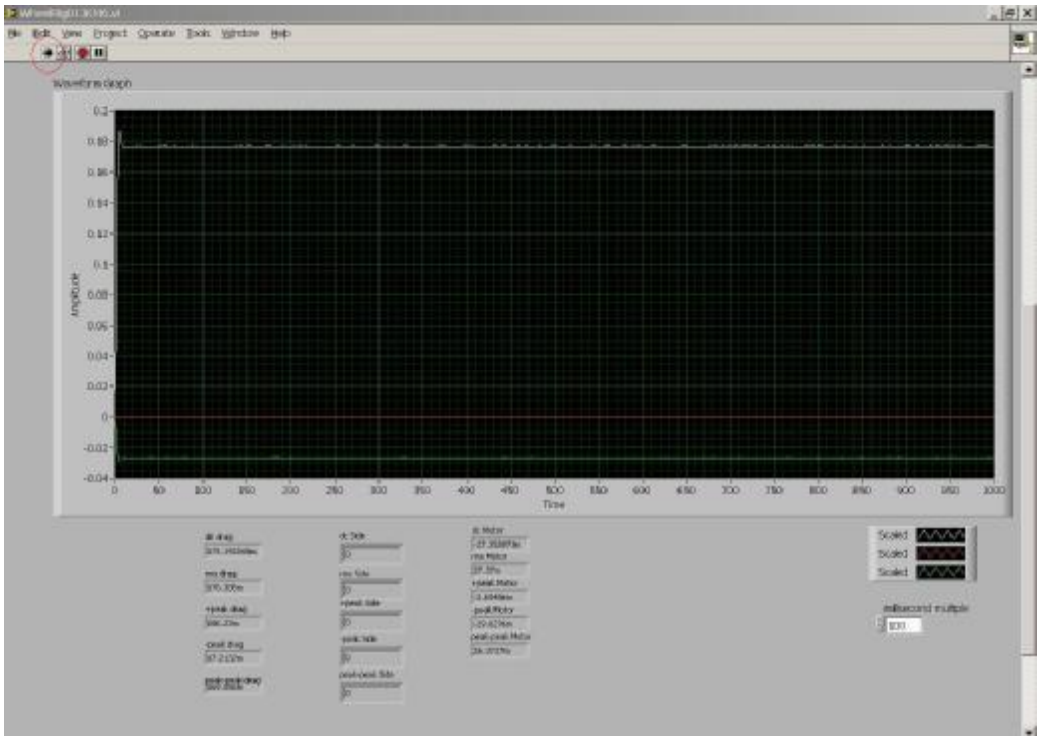

6. Type a file name into the box when prompted

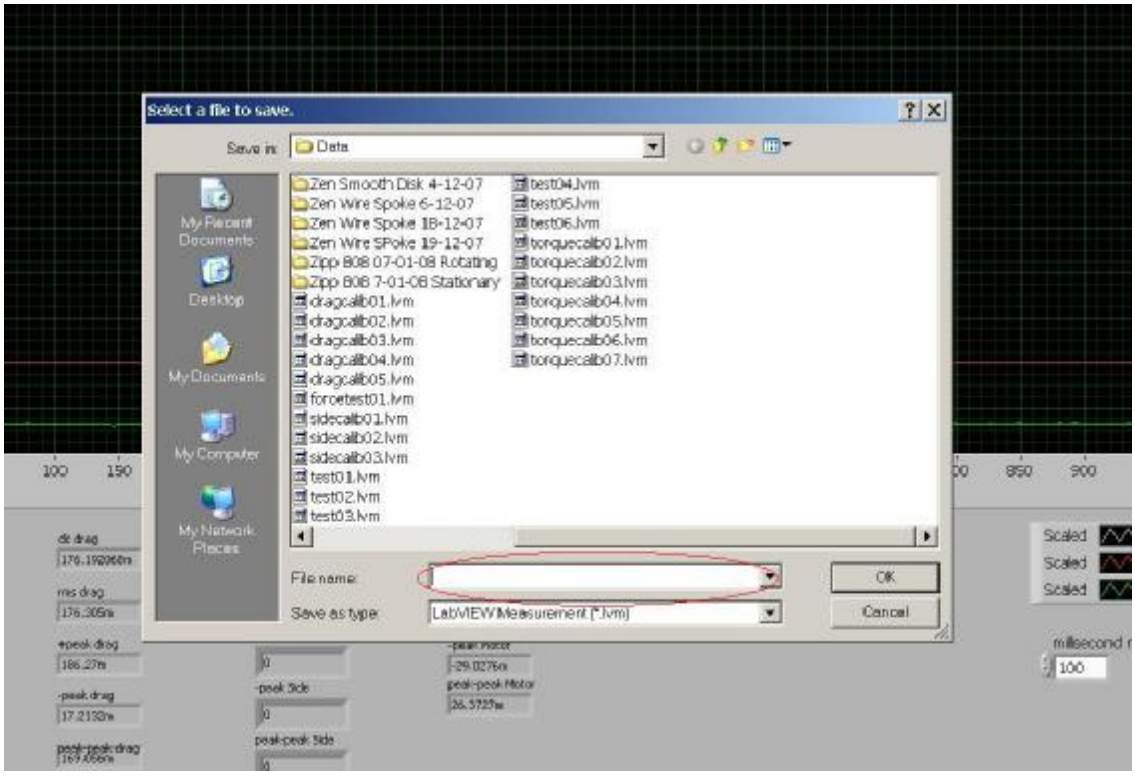

**7.** The data is now being recorded into a ".lvm" file. When you have taken enough data (usually around 20 seconds) press the red button at the top left of the LabView front screen.

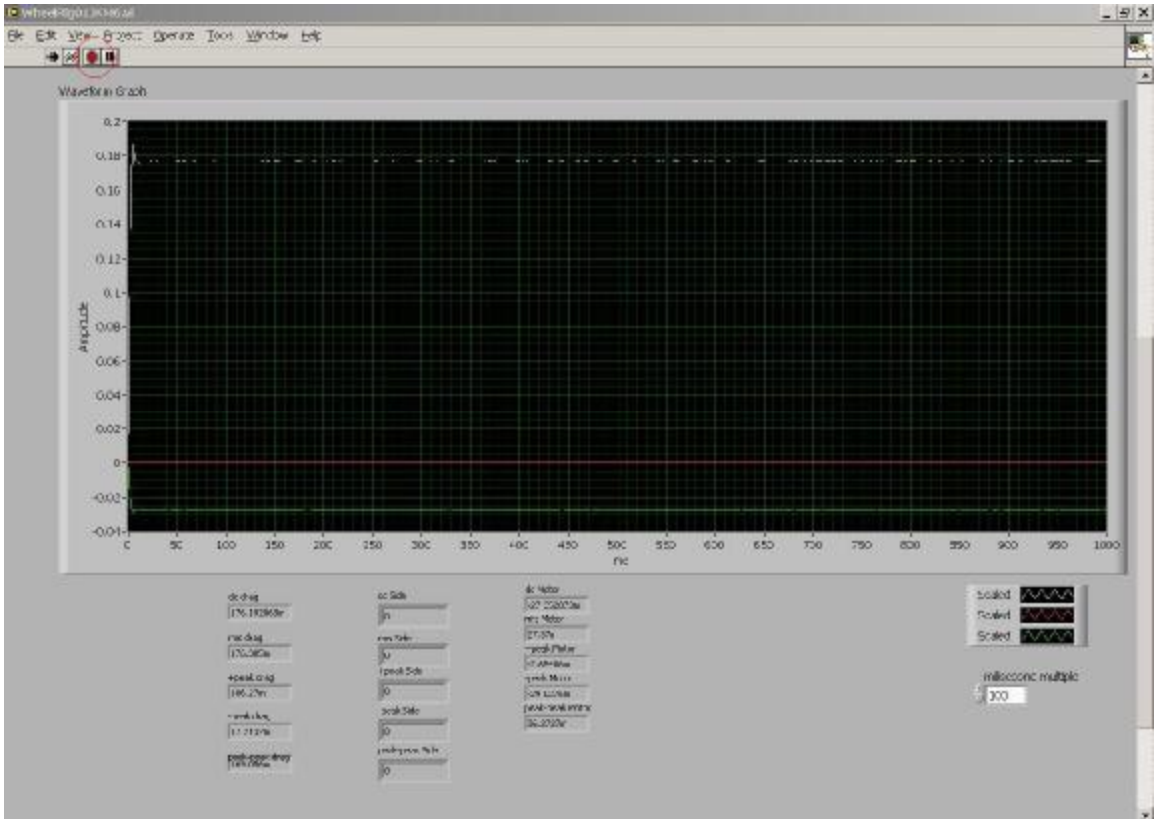


8. Import the data to Excel user the data import function.

# Appendix C – Maxon Motor Contoller User's Guide

**Instructions for using the motor control program**

1. Open the program “DES UserInterface v 1.15”

2. Click OK

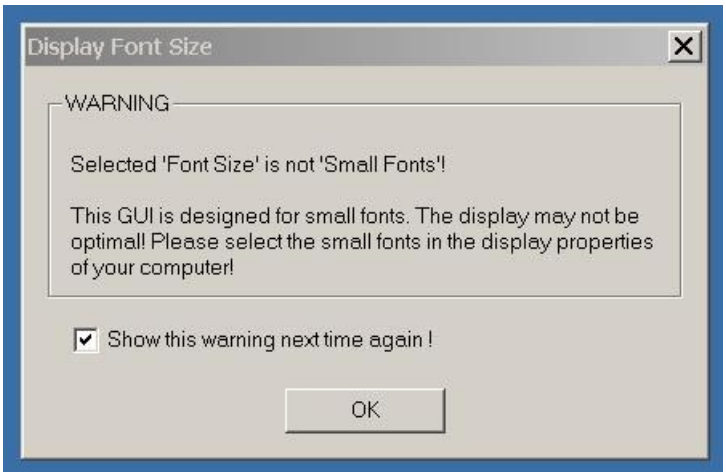


3. Click on “Confirm that you’ve read the operating instructions”

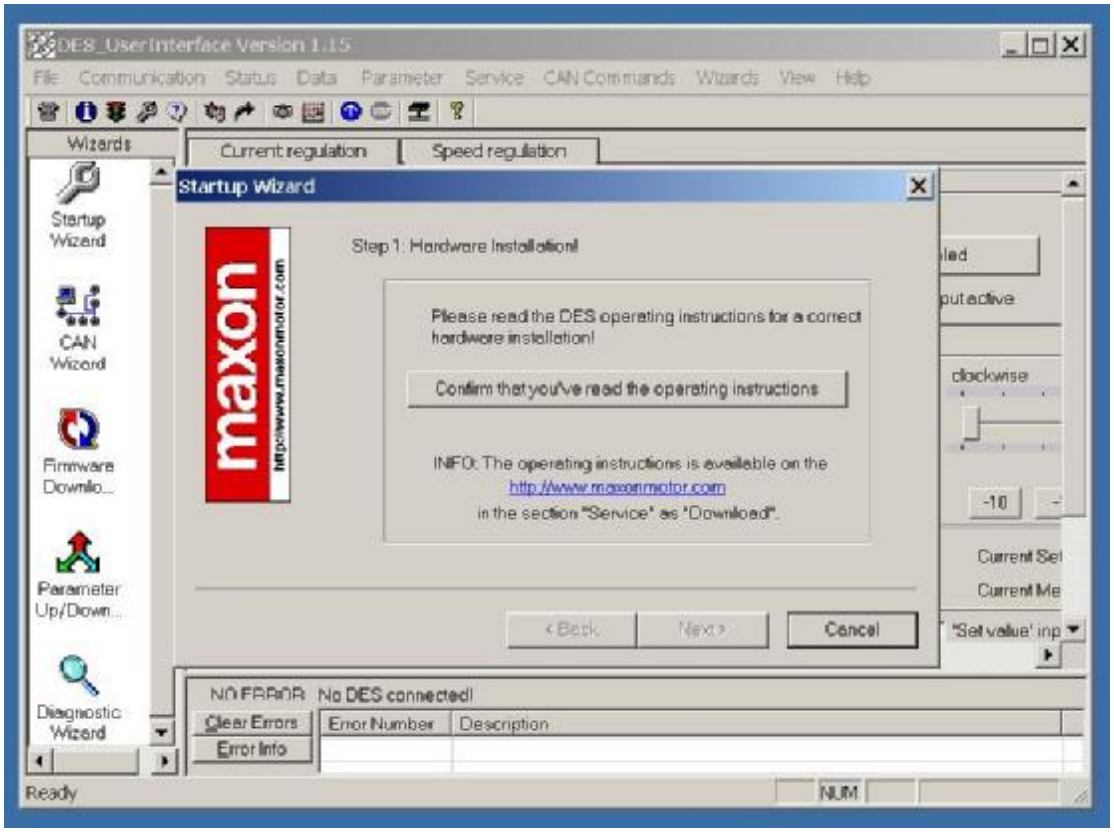


4. Click on “Next”

5. Click “Confirm that you’ve connected the cable”

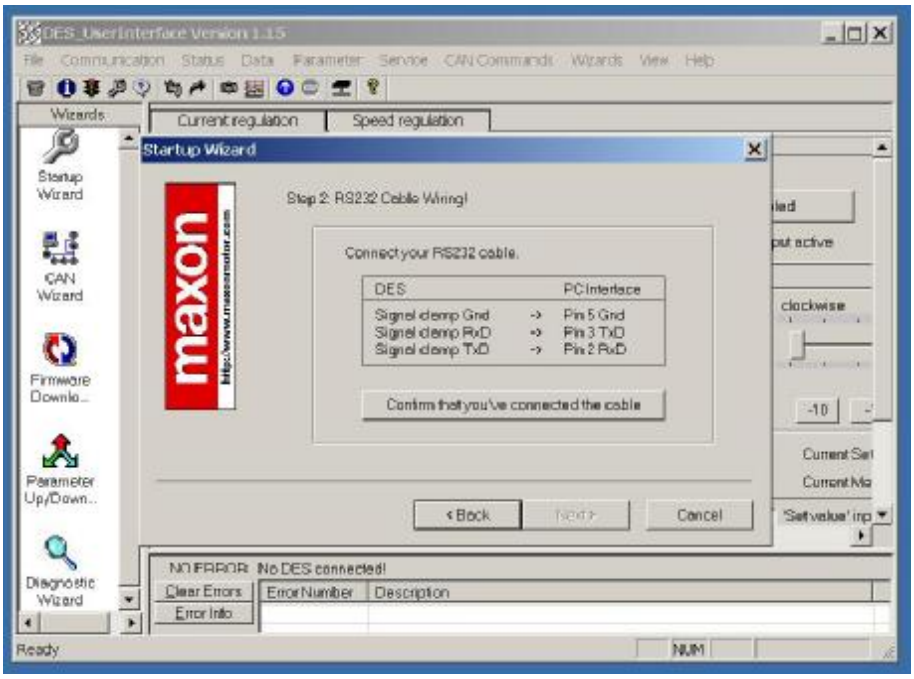


6. Click “Next”

7. Check that Serial Port is “COM2” and baudrate is 38,400 baud

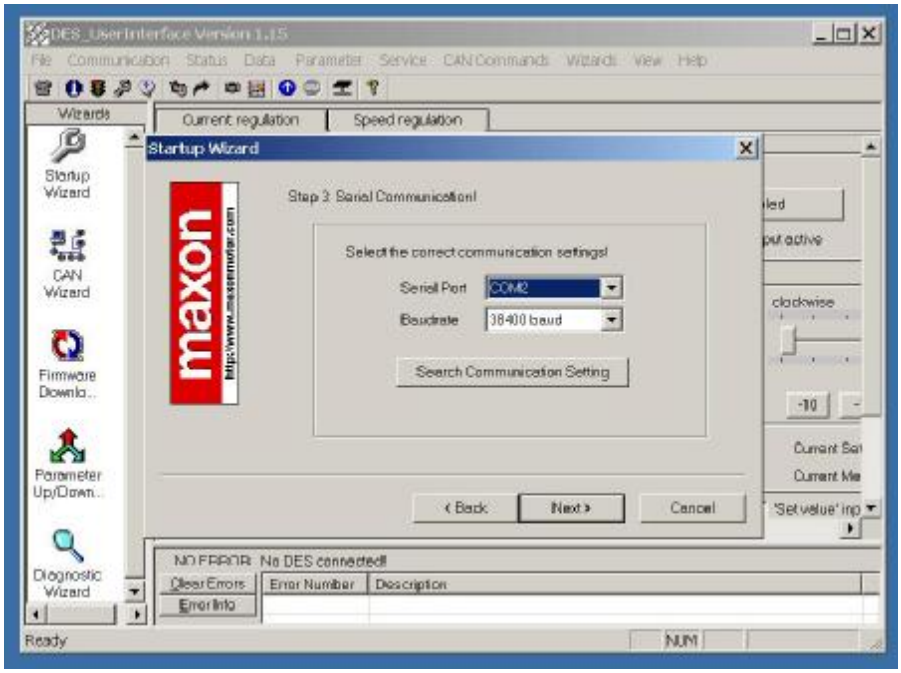


8. Click “Next”

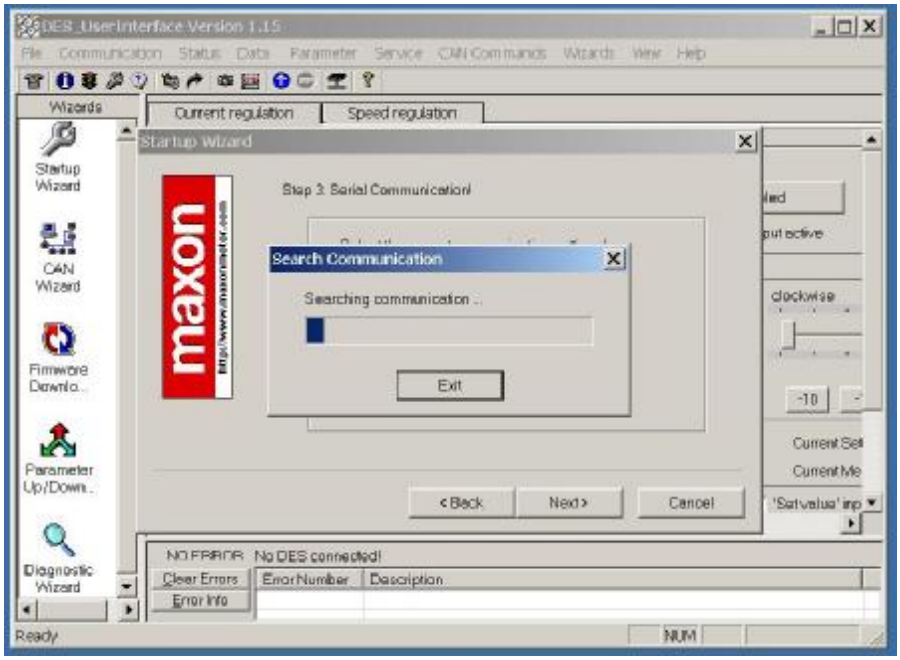


9. Click “Next”

10. Click OK

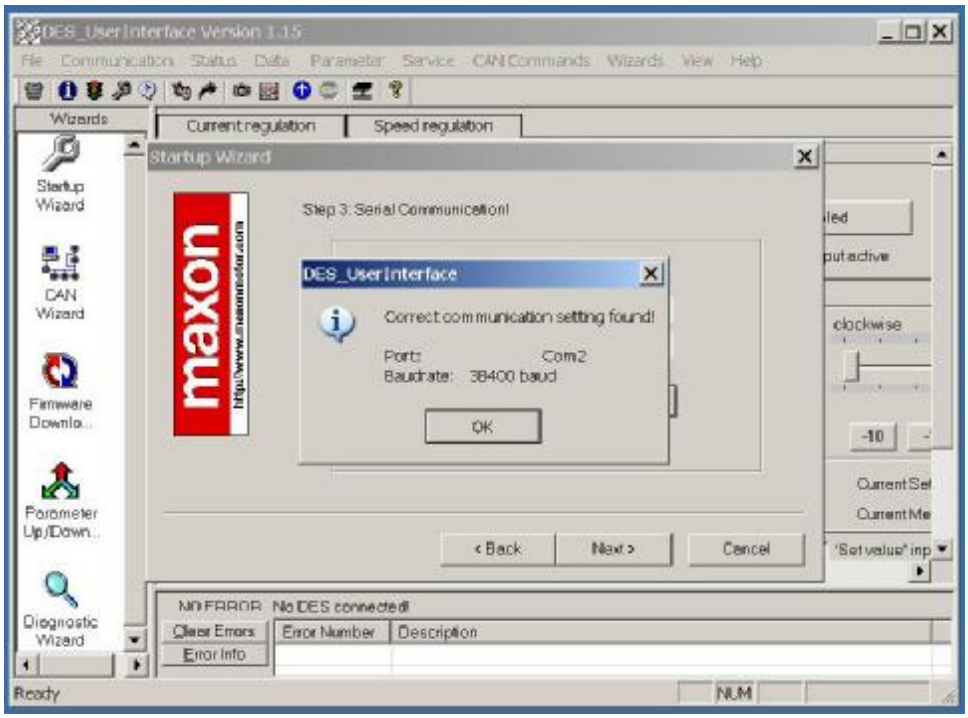

11. Check the encoder resolution is set to 500 pulse/turn

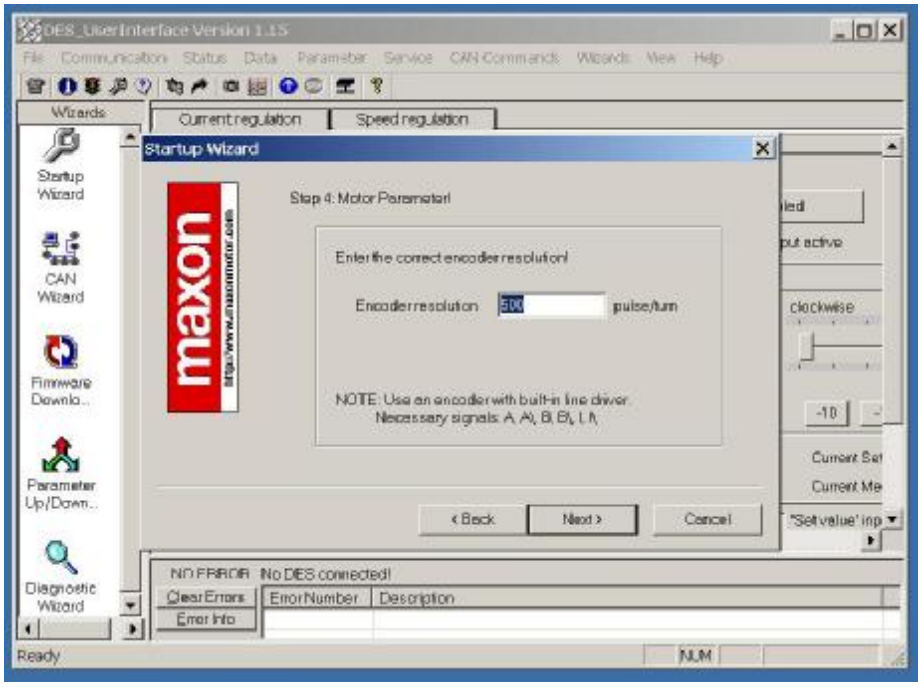


12. Click “Next”

13. Check the *Monitor signal is selected by software* and *Speed monitor signal* buttons

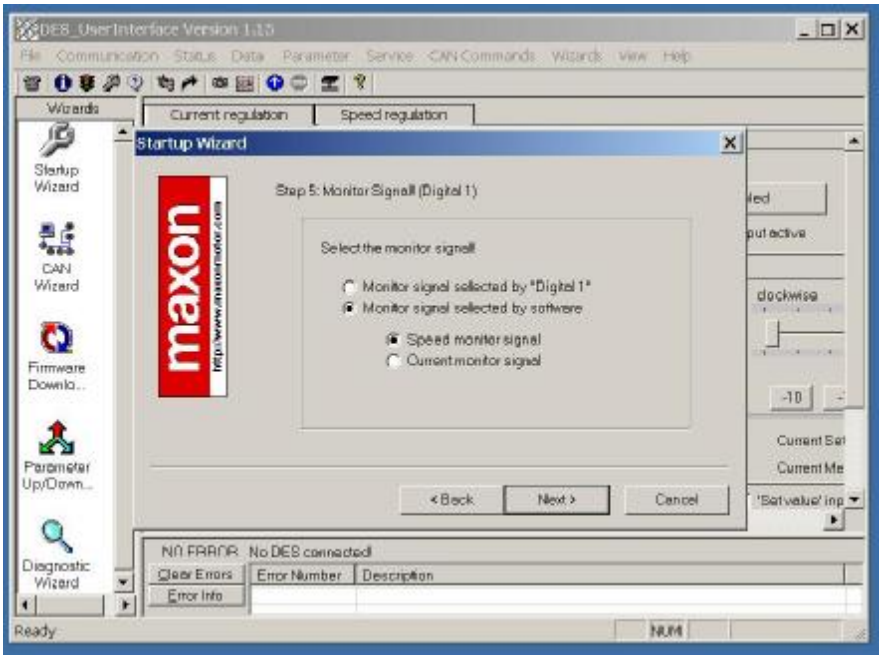


14. Click “Next”

15. Check that *Regulation mode set by software* and *Speed regulation* are selected

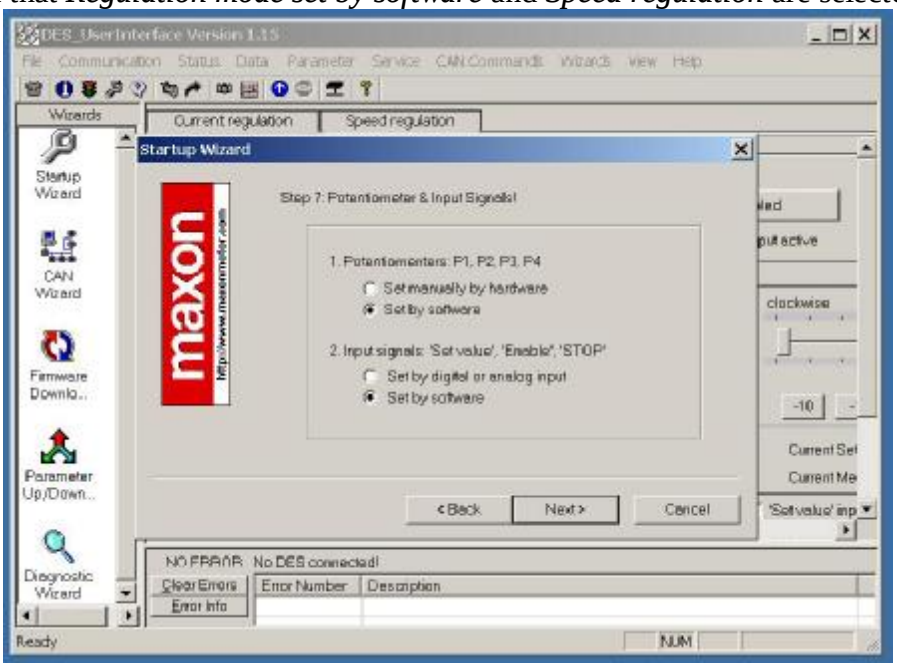


16. Click “Next”

17. Check that *Regulation mode set by software* and *speed regulation* are selected

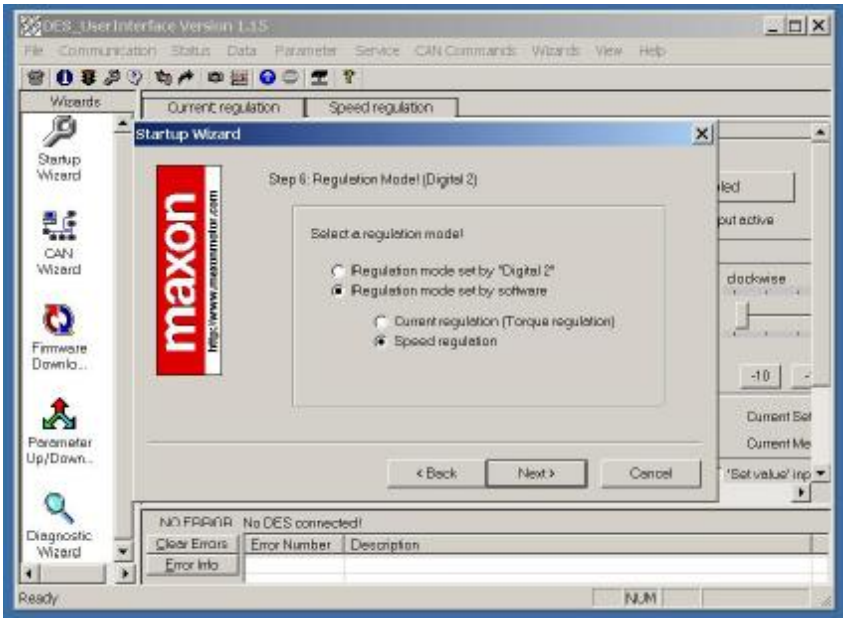


18. Click “Next”

19. Check that the values in the boxes are the same as those in the table below.

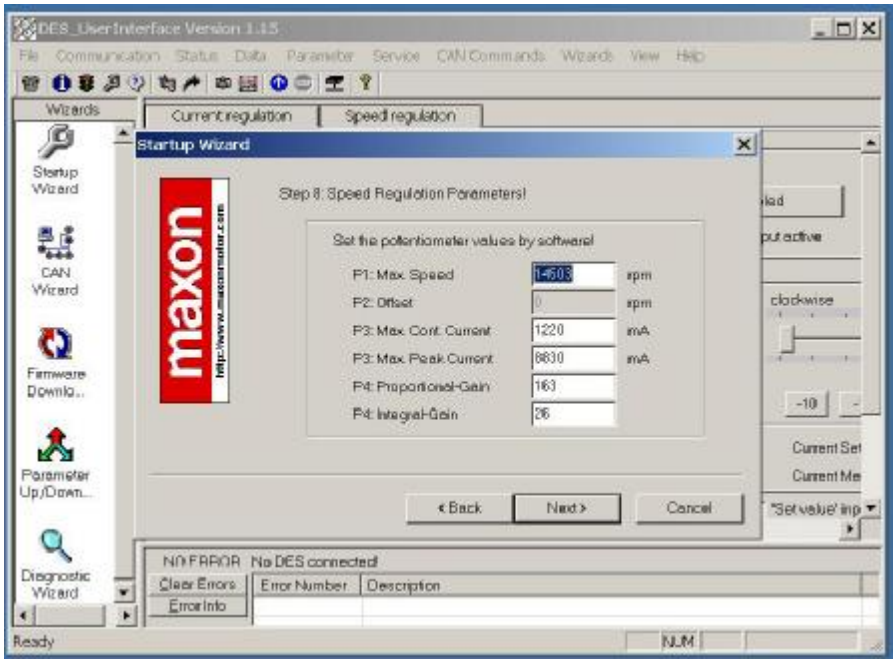


20. Click “Next”

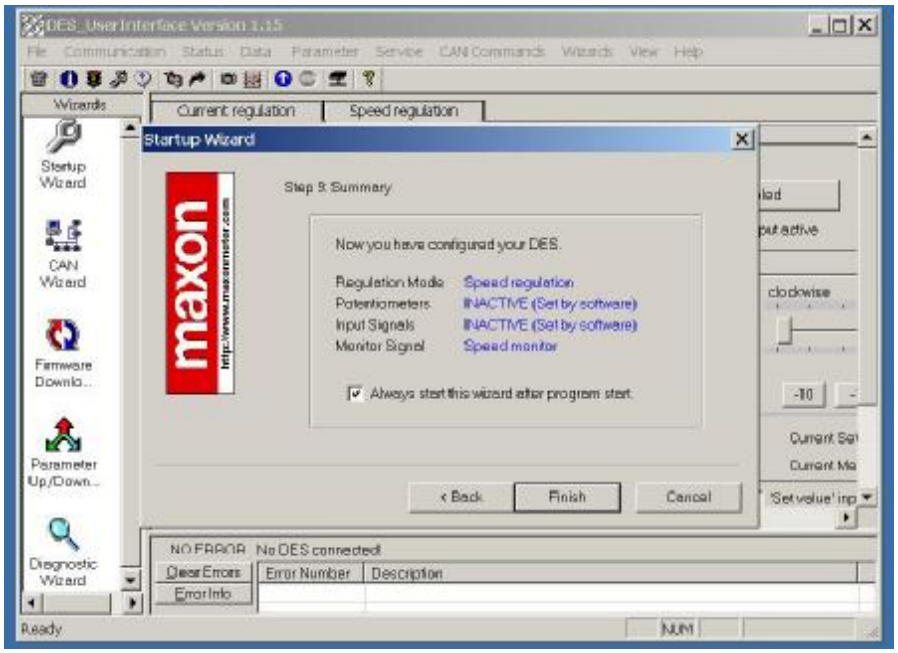


21. Click “Finish”

22. You will now be looking at the motor control screen. Click “Disabled”

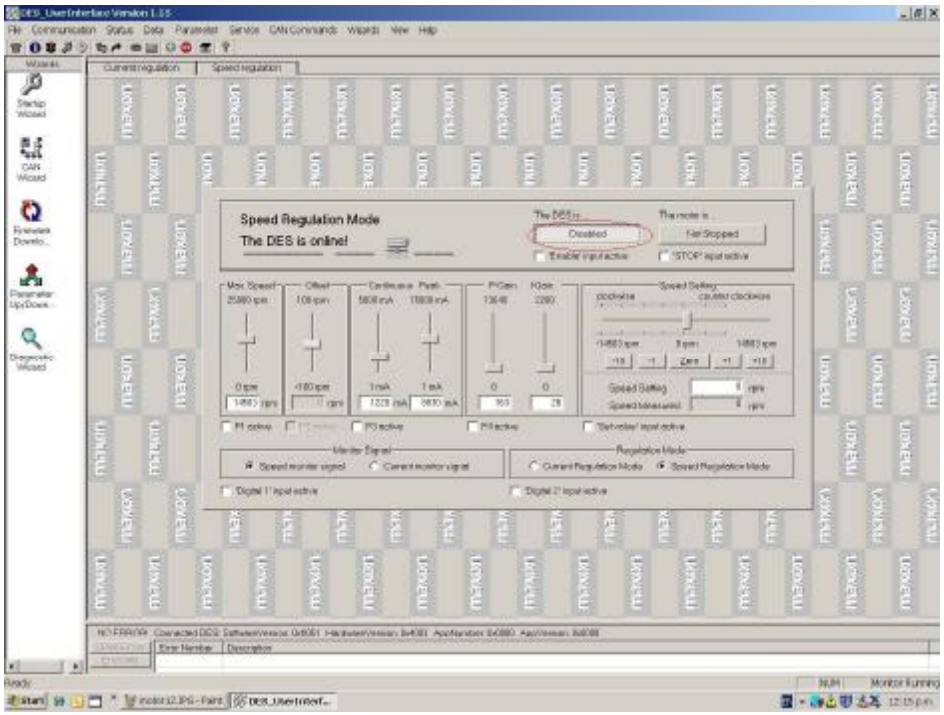


23. The motor is now enabled. Increase the motor velocity up to 300 RPM by pressing the -10 RPM button.

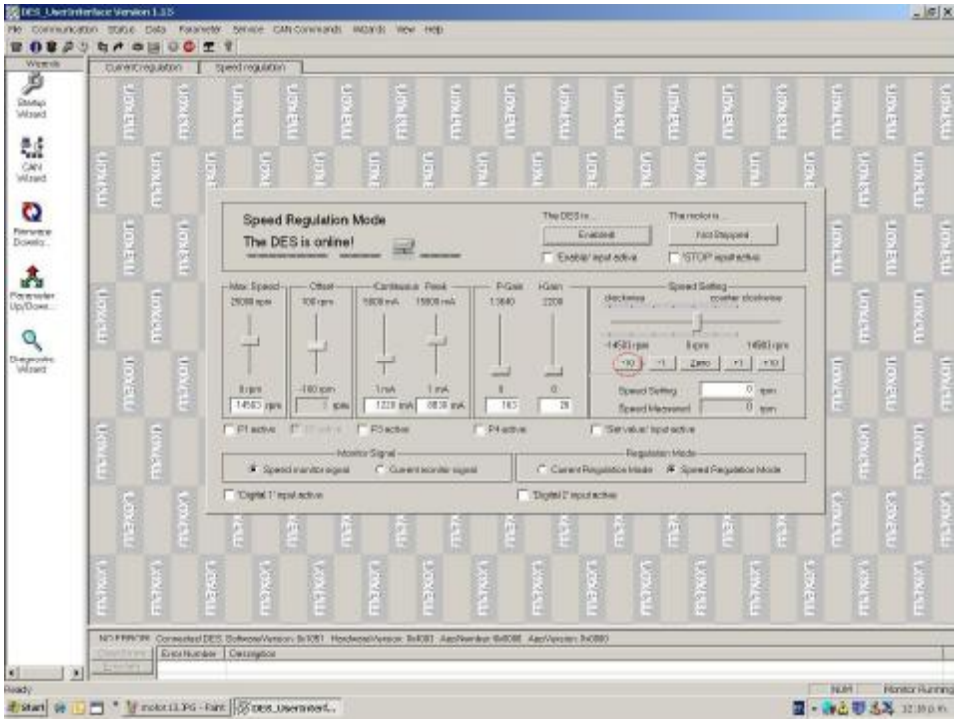

24. Once the motor is up to 300 RPM, increase the speed GRADUALLY by moving the slider to the left.

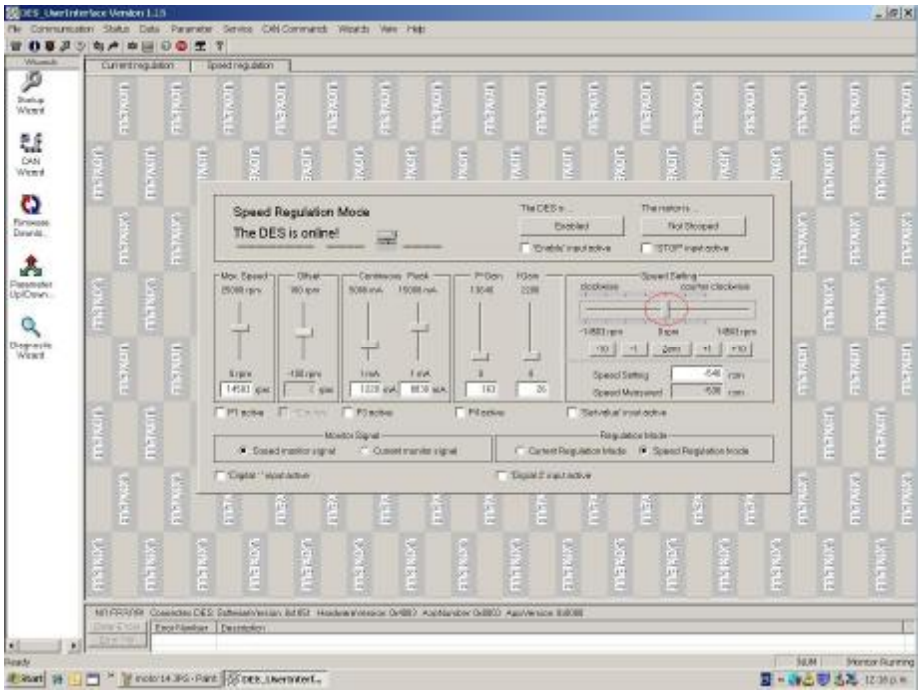


25. Use the slider during testing to decrease and increase the motor speed by 1000 RPM between readings.

26. The motor can be slowed down by GRADUALLY moving the slider to the left. If deceleration is too sudden, the motor will cut out and the rig will come to a sudden stop. This is not good and must be avoided.

27. The motor controller software is not very robust and has a tendency to stop responding after the motor has been running for some time. When this happens, the only way to stop the motor running is to:

- Open the wind tunnel door
- With your left hand pull the driver arm away from the wheel, being careful not to touch the wheel
- With your right hand, unplug the motor power supply and let go of the plugs
- With your right hand press the shaft of a crescent or screwdriver against the front of the tyre to brake the wheel

**IMPORTANT – ALWAYS UNPLUG THE MOTOR CONTROLLER FROM THE POWER SUPPLY IF YOU ARE NOT USING IT.**
If the motor controller is still plugged in after the software has frozen, power is still being supplied to the motor and it can get very hot. Too avoid this; it is a good habit to unplug the motor controller whenever it is not required.